Università degli Studi Roma Tre
Dipartimento di Matematica e Fisica
Corso di Laurea in Fisica

Tesi di Laurea Magistrale in Fisica

Performance studies for the electromagnetic calorimeter of the Mu2e experiment at Fermilab

Relatore esterno
Dott. Stefano Miscetti
Relatore interno
Prof. Domizia Orestano

Candidata
Raffaella Donghia
Matricola
454141

Anno Accademico 2014/2015

Abstract

The Mu2e experiment at Fermilab will search for the charged lepton flavor violating (CLFV) process of muon conversion in an aluminum nucleus field, $\mu + N(Z, A) \rightarrow e + N(Z, A)$. No CLFV interactions have been observed experimentally yet. In the Standard Model, even considering diagrams with neutrinos oscillation, the expected rate is negligible (BR $\sim$ 10^{-54}), so that, observation of these processes should be crucial evidence of New Physics beyond the Standard Model.

The current best experimental limit on $\mu - e$ conversion has been set by SINDRUM II experiment. Mu2e intends to probe four orders of magnitude beyond the SINDRUM II sensitivity, measuring the ratio, $R_{\mu e}$, between the conversion rate to number of muon captures by Al nucleus at 90% CL, with a single event sensitivity of 2.7×10^{-17}:

$$R_{\mu e} = \frac{\mu^- N(Z, A) \rightarrow e^- N(Z, A)}{\mu^- N(Z, A) \rightarrow \nu_\mu N(Z - 1, A)} < 6 \times 10^{-17}$$

The signature of this neutrinoless conversion process is a monoenergetic electron, with an energy slightly lower than the muon rest mass, $\sim$ 104.96 MeV. In order to achieve our goal, a very intense muon beam ($\sim 10^{10}$ Hz) has to stop on an aluminum target and a precise momentum analysis has to be performed. The beam must also have a pulsed structure to discriminate the prompt beam-induced background. Fermilab provides the right beam.

The Mu2e experiment recently achieved US Department of Energy's Critical-Decision 2 (CD-2) approval in March. At the same time, the Mu2e collaboration was awarded authorization to begin the construction of the experimental hall, which saw ground-breaking on 18th April.

In this thesis I present the electromagnetic calorimeter system, the experimental tests and results carried out for the study of a backup option. This option consists of a calorimeter composed by CsI crystals readout by silicon photomultiplier (SiPM, MPPC). The work is organized in 5 chapters.

In the first Chapter, an explanati on of the physics motivation for searches of CLFV process in the muon sector is reported.

In the second Chapter, the experimental technique for this search is studied, comparing Mu2e to other recent or similar CLFV search experiments. Then the Superconducting Solenoid Magnetic System, divided in Production, Transport and Detector solenoids, is briefly described and finally a summary of the overall detector organization is given.

In the third Chapter, the requirements and the technical choices for the electromagnetic calorimeter are discussed, focusing on its particle identification and background rejection capabilities. Furthermore, the baseline (BaF_2 crystals readout by superlattice solar blind avalanche photodiodes) and backup option for the calorimeter design are described in detail, explaining the advantages and problematics of the different crystal and photosensor choice.

The original point of this thesis is reported in the last two chapters, where I have personally contributed and participated to the most of the described measurements

In the fourth Chapter, the measurement concerning crystals light yield, longitudinal response uniformity and irradiation tests both with ionizing dose (at Calliope γ irradiation facility, ENEA) and neutrons (at Frascati Neutron Generator facility, ENEA) are discussed. The pure BaF_2 (CsI) crystals readout by a photomultiplier show a light yield of about 100 (130) photoelectrons per MeV, which increases by a factor of $\sim 60\%$ using optical grease to couple the crystal to the phototube. All the crystals have also a good longitudinal response uniformity, with an average variation of 0.5%/cm. A CsI crystal, irradiated with a dose up to 20 krad, kept its light yield ($\sim$ 35 $N_{p.e.}$/MeV at crystal center) and LRU (20%). After a total dose of 90 krad (three times the experimental

lifetime), a 20% reduction in light yield is observed, while the longitudinal response uniformity looks unaffected. Some fluorescence effects are visible after an intense irradiation dose, which become negligible after few hours. CsI and BaF_2 crystals have also been irradiated with a neutron fluency up to 9×10^{11} n/cm^2, corresponding to about 1.5 times the total flux expected for the calorimeter in three years of running. At the end of the irradiation test, an acceptable deterioration for the light yield has been observed in the tested crystals.

In the fifth Chapter, the performances of a small CsI+MPPCs calorimeter prototype are reported. Once completed the single channel measurements, a 3×3 calorimeter prototype of CsI crystals readout by UV-extended SPL MPPCs (SiPM) has been assembled and tested with an electron beam in the energy range from 80 to 120 MeV at the Beam Test Facility (Laboratori Nazionali di Frascati, INFN). A light yield of ~ 30 $N_{p.e.}$/MeV has been measured. An energy resolution of $\sim 7\%$ and a time resolution of 110 ps have been achieved for 100 MeV electrons impinging perpendicularly to the calorimeter surface.

Contents

Chapter 1

Charged Lepton Flavor Violation

1.1 The Standard Model

The Standard Model (SM) is currently the best theoretical model describing our understanding of modern elementary particle physics and their interaction via three of the four fundamental forces: the strong and electroweak interactions.

Mathematically, it is a quantum field theory involving two different types of fields: twelve fermionic fields, which represent the matter particles (some of their important properties are shown in Table 1.1); and thirteen bosonic fields, of which four represent the carriers of the weak and electromagnetic forces, eight the strong interactions and one represents the Higgs boson [1].

Electric Charge	1st generation	2nd generation	3rd generation
$+\frac{2}{3}$	u	c	t
$-\frac{1}{3}$	d	s	b
0	ν_e	ν_μ	ν_τ
-1	e	μ	τ

Table 1.1: *Quarks and leptons in the Standard Model. As far as we know, they are the smallest basic units of matter.*

The gauge symmetry of the SM is a $SU(3)_C \times SU(2)_L \times U(1)_Y$ gauge group, where C indicates color charge, L indicates that only left-handed fields participate

in the weak interaction and Y is the hypercharge. The $SU(2)_L \times U(1)_Y$ electroweak part of the gauge group breaks down to the $U(1)_{EM}$ of electromagnetism via the Higgs mechanism.

The SM was developed in the early 1970s and since then it has explained almost all experimental results [2], including the existence of the Higgs boson (discovered in the LHC at CERN in 2012 [3][4]). However, even though it is currently the best description of the subatomic world, it incorporates only three of the fundamental forces, excluding gravity. Indeed, the Standard Model is not a complete theory of the universe, for example it does not explain neutrino mass.

1.1.1 Massless neutrinos

Neutrinos are neutral fermions classified as leptons, so they are affected only by the weak subatomic force and by gravity. One of the problems with the SM is the fact that it describes neutrinos as massless. This is in stark contrast to the observation of neutrino oscillations which demonstrates that neutrinos do have mass (Super Kamiokande - 1998 [5], SNO - 2001[6]).

Since right-handed fermions exist in a weak singlet (i.e. they do not participate in the weak interaction) and, in the lepton sector, this singlet comprises of only charged lepton, no Higgs coupling can be written for neutrinos since this requires both a left-handed and a right-handed field, so neutrinos are massless in the SM. However, it is possible to minimally extend the SM by adding an extra right-handed fermion singlet that contains right-handed neutrinos in order to obtain the Higgs couplings.

Many extensions to the SM implement neutrino masses in a different way with respect to the Higgs mechanism, for example, by assuming that neutrinos are Majorana particles in nature (they are their own antiparticles), this allows for Majorana mass terms to be added via the seesaw mechanism [7] with a mass that be at the GUT scale ($\sim 10^{16}$ GeV). If these heavy right-handed neutrinos existed at the beginning of the universe, then they could undergo CP-violating decays to produce a lepton asymmetry, which could then produce a baryon asymmetry [8]. Since right-handed neutrinos cannot be directly produced at colliders, searching for their effects

in neutrino oscillations, neutrinoless double beta decay ($0\nu\beta\beta$) [9] and charged lepton flavor violation are now a priority.

1.1.2 Lepton flavor Violation in the Standard Model

Symmetries and conservation laws play a fundamental role in physics: for each symmetry of the Langrangian, there is a corresponding conserved quantity (Noether's theorem).

In the SM, the lepton number and the baryon number are accidental symmetries. As stated by Noether's theorem, all conservation laws should have a corresponding underlying local symmetry (for example, conservation of momentum arises from the requirement that the laws of physics are translationally invariant). This is not the case for lepton number conservation which arises from an ad-hoc global symmetry of the form $U(1)_e \times U(1)_\mu \times U(1)_\tau$. The lepton U(1) global symmetry is accidental.

Renormalizable operator in the SM Lagrangian that breaks conservation of lepton number simply cannot be written. Once you go beyond the SM by including higher-dimensions operators, there is no reason for lepton number (and baryon number) to be conserved.

In the SM, the quantity known as lepton flavor (L_e, L_μ, L_τ) is also conserved. For leptons of a given flavor it has a value of +1 and -1 for antileptons. The other lepton flavor numbers are 0 for both leptons and antileptons (i.e. the muon, μ, has $L_\mu = +1$ and $L_e = L_\tau = 0$).

In the minimal SM, neutrinos are massless and lepton flavor L_e, L_μ and L_τ is conserved separately for each generation. But neutrino oscillations allow mixing among the lepton families, giving rise to lepton flavor violating (LFV) processes. This will also be generically true for any model that includes a mechanism for generating neutrino masses.

The rate at which LFV processes occur in the neutrino sector is constrained by the measured neutrino mixing parameters, given by the PMNS matrix (Pontecorvo-Maki-Nakagawa-Sakata matrix), which contains information about neutrino mixing, but the rate at which charged lepton flavor violating (CLFV) occurs is model depen-

dent and can vary over many orders of magnitude. However, even with the addition of neutrino masses, the SM prediction for the rate of CLFV processes is incredibly small, $\mathcal{O}(10^{-54})$ [10]. If the Standard Model is the only source of CLFV, then the violation cannot be observed experimentally.

The reason for this very small rate can be seen in Figure 1.1, which shows the Standard Model Feynman diagram of the $\mu \to e\gamma$ process.

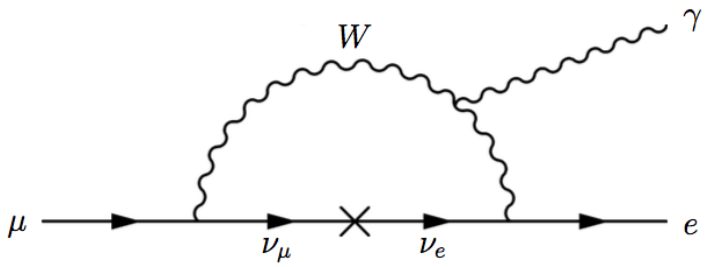

Figure 1.1: *Feynmann diagram for the charged lepton flavor violating process $\mu \to e\gamma$ in the Standard Model.*

In this process, the incoming muon decays emitting a muon neutrino and a W boson, which gets reabsorbed after the neutrino oscillates into an electron neutrino, creating an electron. Since the neutrino is oscillating in a virtual loop (much shorter length scale than the distance that neutrinos have actually been observed oscillating over), this process is massively suppressed by a factor of $m^2_{\nu_i}/M^2_W$ as shown in eq. 1.1, where the branching ratio (BR) of this process is given:

$$BR(\mu \to e\gamma) = \left| \frac{3\alpha}{32\pi} \sum_i U^*_{\mu i} U_{ei} \frac{m^2_{\nu i}}{M^2_W} \right| < 10^{-54}\,, \tag{1.1}$$

where α is the electromagnetic coupling constant, U is the PMNS neutrino mixing matrix and m_{ν_i} and M_W are the masses of the neutrinos and W boson respectively.

On the other hand, many New Physics (NP) models predict significant enhancements to CLFV rates. Indeed, the minute BR of eq. 1.1 makes searches for CLFV processes very appealing, since it means that there is no SM background to take account of and so any observation of CLFV would be a clear evidence of physics beyond the Standard Model.

1.2 Beyond the Standard Model

The origin of the flavors of elementary particles is still unknown. Their properties and structure should reflect the nature of the physics beyond the SM (BSM). Flavor physics is thereby believed to provide a path to new physics.

Up to now, new particles expected in BSM physics have not been found at the Large Hadron Collider (LHC). Therefore, the search for CLFV is crucial to find any clues of BSM physics.

In many BSM scenarios, rates for CLFV processes are within the reach of the next generation of experiments.

1.2.1 Independent model Lagrangian extension in the muon sector

Important CLFV processes involving muons are $\mu \to e\gamma$, negative muon to electron conversion in a nucleus field $\mu^- + N(A,Z) \to e^- + N(A,Z)$ and $\mu^+ \to e^+e^+e^-$. Even if the SM does not predict these processes, within measurable BRs, and because there are so many different BSM theories, it is possible to explicitly insert a model-independent CLFV lagrangian in order to study process sensitivities. There are two possible types of interactions between leptons and quarks which contribute to the effective Lagrangian for muon's CLFV processes of $|\Delta L_i| = 1$ (such as the previous cited processes): photonic or loop interaction and four-fermion or contact interaction (Fig. 1.2).

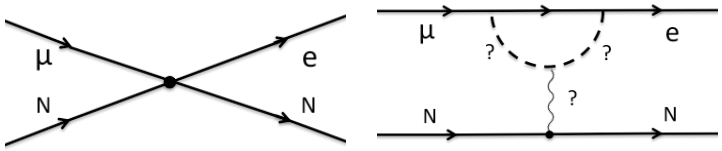

Figure 1.2: *Feynmann diagrams for the muon to electron conversion process in a nucleus field. Left: photonic interaction. Right: contact four-fermion interaction.*

For the photonic contribution, there is a definite relation between the muon conversion process and $\mu \to e\gamma$ decay. Supposing the photonic contribution is

dominant, the BR of the muon conversion process is expected to be smaller than the other process by a factor of a few hundred due to electromagnetic interaction of a virtual photon. This implies that the search for muon conversion at the level of 10^{-16} is comparable to that for $\mu \to e\gamma$ at the level of 10^{-14}.

If the contact term dominates, the $\mu \to e\gamma$ decay would be small whereas the muon to electron conversion could be sufficiently large to be observed. If a $\mu \to e\gamma$ signal is found, also a conversion signal should be found. The ratio of the branching ratios between $\mu \to e\gamma$ decay and muon to electron conversion carries vital information on the intrinsic physics process. If no $\mu \to e\gamma$ signal is found, there will still be an opportunity to find a $\mu - e$ conversion signal because of the potential existence of non-photonic contributions.

The effective Lagrangian that includes both the photonic and non-photonic contributions is given by 1.2 [10]:

$$L_{CLFV} = \frac{m_\mu}{(k+1)\Lambda^2}\bar{\mu}_R\sigma_{\mu\nu}e_L F^{\mu\nu} + \frac{k}{(k+1)\Lambda^2}\bar{\mu}_L\gamma_\mu e_L(\bar{u}_L\gamma^\mu u_L + \bar{d}_L\gamma^\mu d_L) \qquad (1.2)$$

The parameters of this Lagrangian are Λ and k, where the first is the energy scale of new physics and k is the ratio between the contact four-fermion (non-photonic) and loop-type (photonic) interactions. For $k \ll 1$, the photonic interaction dominates and for $k \gg 1$, the contact interaction dominates.

Figure 1.3 shows the relation between the BRs of $\mu \to e\gamma$ and $\mu - e$ conversion process as a function of the parameter k. The parameter space for muon CLFV that has been excluded by previous experiments and the region that future experiments will be able to probe are also reported.

It is also important to note that CLFV searches can probe energy scales of $\mathcal{O}(10^4)$ TeV, which are much higher than what can currently be directly probed at colliders. The upper limits expected at 90% CL for the future experiments MEG upgrade, Mu2e and Mu2e at PIP II (Proton Improvement Plan-II [13]) are also shown.

A second thing to note from Figure 1.3 is that an observation in a single channel would not give any indication as to the form of the new interaction. For example, if a signal was seen in muon conversion alone with a branching ratio of 10^{-16} then the value of k would not be known until a signal had been seen or excluded in $\mu \to e\gamma$

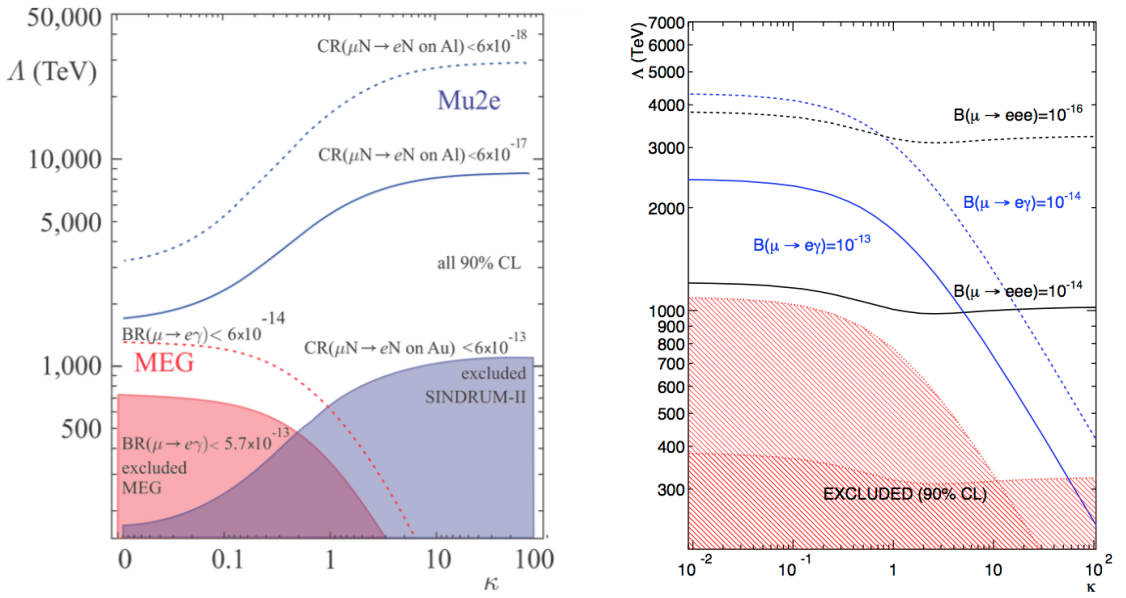

Figure 1.3: *The current and future limits expected of $\mu \to e\gamma$ and $\mu - e$ conversion (left) and $\mu \to 3e$ (rigth) in terms of the two parameters Λ and k, where the first one is the energy scale of the new interaction and the second is the ratio between the four-fermion and loop interactions.*

and $\mu - e$ conversion at a sensitivity greater than 10^{-14}.

Obviously, an observation of CLFV would lend some weight to these theories. However, a non-observation of CLFV would also restrict the large parameter spaces of these theories and possibly exclude most of them.

1.2.2 New physics models

The discovery of CLFV events, or just a better constraint on the BR, could give strong indications on which NP model is preferred.

SUSY model have recently received much attention. Other examples include extra-dimension models, little Higgs models, models with new gauge Z' bosons, models with new heavy leptons, leptoquark models, etc[11]. Some NP examples and their CLFV effects are reported in the following.

SO(10) SUSY Grand Unified Model In the Supersymmetric version of the SM (SUSY), the origin of CLFV could be interactions at a very high energy scale, such as the GUT scale or the mass scale of a heavy right-handed Majorana

neutrino that appears in the seesaw mechanism.

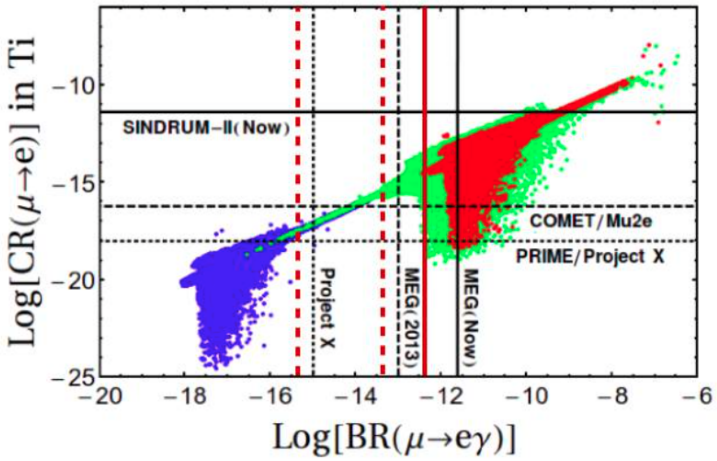

Figure 1.4: *Muon Conversion Rate $CR(\mu \to e)$ in titanium versus $BR(\mu \to e\gamma)$ for the PMNS-like neutrino Yukawa coupling in mSUGRA (red), Non Universal Higgs Mass (green) and for CKM-like neutrino Yukawa coupling (blue) for tanβ = 10. Red vertical lines represent the present limit given by MEG [14], the expected result for the MEG upgrade (dashed) [15] and the expected result for a conceptual $\mu \to e\gamma$ experiment [15]. Horizontal black lines, instead, represent limit on muon-to-electon conversion rate from SINDRUM II [19] result and Mu2e/COMET planned results. Project X, now PIP-II, is related to an improvement of 10 times the beam intensity, currently under study at Fermilab. Adapted from [18].*

SUSY can lead to sensibly large rates of CLFV process. It is possible to relate the $\mu^- N \to e^- N$ rate in titanium to of SO(10) SUSY GUT breaking parameters [18], taking into account the measured value of the neutrino mixing angle θ_{13} value and Higgs mass with different hypothesis of the neutrino Yukawa couplings (Fig. 1.4).

In fact, SUSY predicts $\mu^- N \to e^- N$ conversion through a penguin diagram with two sleptons or charginos in the loop (Fig. 1.5).

Higgs-induced lepton flavor violation Some NP models includes LFV processes induced by Higgs exchange. Compared to $\mu \to e\gamma$ and $\mu \to 3e$, muon conversion is more sensitive because of the smallness of the Yukawa couplings in the first two cases [20]. The conversion can be induced with a tree-contribution involving light quark or with a loop-induced effect of heavy quarks to the gluons (Fig. 1.6, right). The muon conversion in nucleus is also the most sensitive channel for the study of Yukawa couplings $|Y_{\mu e}|$ and $|Y_{e\mu}|$ (Fig. 1.6, left).

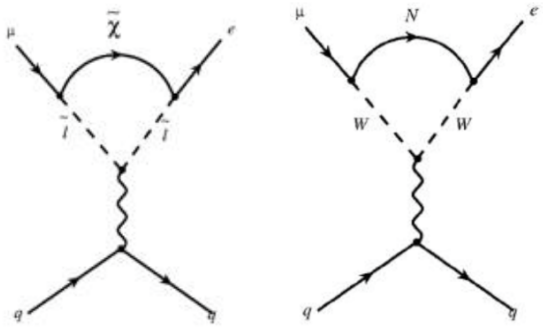

Figure 1.5: *On the left (right) the Feynman diagram for μ+N $\rightarrow$ e+N process in the SUSY (heavy neutrino) model, with sleptons (heavy neutrinos) in the loop and chargino (W boson) exchanging a photon with the nucleus*

Littlest Higgs model with T-parity In the Littlest Higgs model with T-parity (LHT), the Higgs boson is considered an exact Goldstone boson under several symmetries. Only if the symmetries are all broken (collective symmetry breaking, CSB), the Higgs boson picks up a contribution to its mass.

In order to avoid fine tuning from electroweak precision data, a discrete symmetry, analogous to SUSY R-parity and called T-parity, is introduced. The scanning

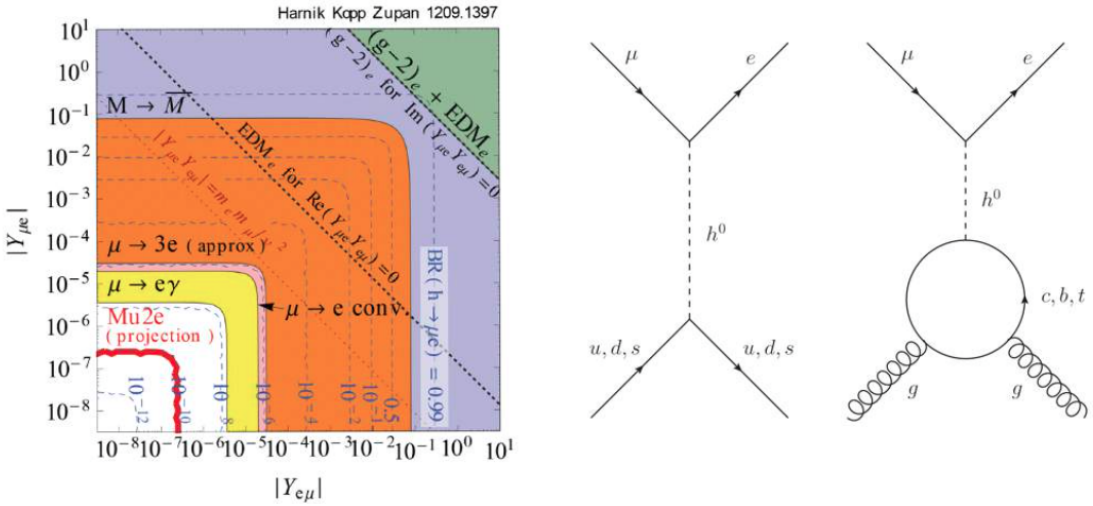

Figure 1.6: *Left: constraints on the flavor-violating Yukawa couplings $|Y_{\mu e}|$ and $|Y_{e\mu}|$ for a 125 GeV Higgs boson [20]. Thin blue dashed lines are contours of constant BR for $h \rightarrow \mu e$, while the thick red line is the projected Mu2e limit. Constraints from $\mu \rightarrow e\gamma$ process are not updated to the latest MEG result [14]. Right: Higgs-induced LFV for a muon conversion can involve light quarks with a tree diagram (on the left) or gluons with a loop of heavy quarks (on the right).*

of the parameters of this model provides measurable BRs both for $\mu \to e\gamma$ and for $\mu N \to eN$ (Fig. 1.7) [21].

The $\mu - e$ conversion sensitivity for this process is extremely good. Indeed, for most of the parameter space, is observed by MEG upgrade, the $\mu - e$ conversion will observe it with much larger statistics. In case of no observation the theory will be excluded.

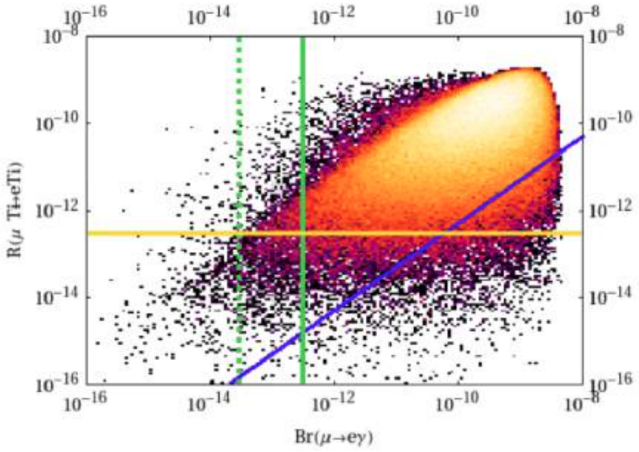

Figure 1.7: *Correlation between $\mu \to e\gamma$ and $\mu - e$ conversion rates in Ti obtained from a general scan over the LHT parameters. The blue line represents the MSSM dipole contribution, the green lines are the present (solid) and expected (dashed) upper limits by MEG and the yellow solid line is the SINDRUM II upper limit. The Mu2e experiment would cover all the parameters of this scan. Adapted from [21]*

Heavy neutrinos As previously stated, neutrino oscillation gives the first proof of LFV interactions. However, rates for CLFV processes are not immediatly related to neutrino masses, because they strongly depend on the undergoing mechanism. The presence of new heavy neutrino mass states, different from mass eigenstates ν_1, ν_2, ν_3, is related to a muon conversion process through the neutrino oscillation in Feynman loop (Fig. 1.5).

Scalar Leptoquark model The presence of scalar leptoquars at TeV scale could modify CLFV conversion rate processes through a new coupling λ [22], without violating all the other constraints from quark flavor physics (Fig. 1.8). In this case the mass and λ coverage of $\mu - e$ conversion is much higher than MEG upgrade. With Mu2e the sensitivity will be even larger.

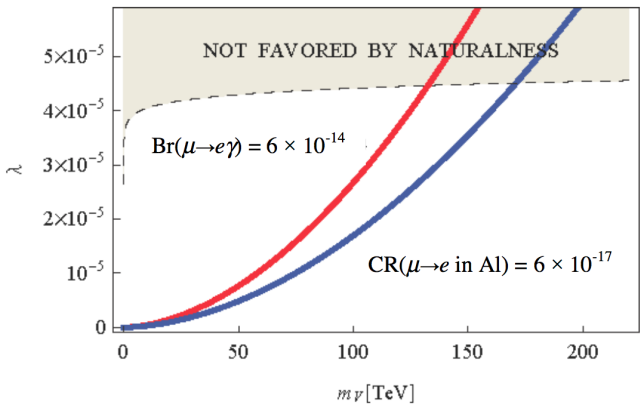

Figure 1.8: *Value of the coupling constant λ from [22] as a function of the scalar leptoquark mass. The thick solid lines represents the limits for two different values of muon conversion rate in Al (red and blue) and the thin solid red line the limit for $\mu \to e\gamma$ process. The shaded area corresponds to values which do not satisfy the naturalness criterion as defined in [22]*

Left-Right Symmetric Models Left-Right symmetric models are extensions of the SM useful to restore parity at short distances. A recent study [23] predicts the CLFV rates assuming a new mass breaking scale at around 5 TeV. From the correlation between the BR for the MEG upgrade and BR of muon conversion from Mu2e, it is possible to cover the full phase space of this theory: the observation of $\mu \to e\gamma$ with a branching ratio of 10^{-13} would imply a $\mu - e$ conversion rate around of 10^{-14} and then several hundreds of events in the Mu2e experiment (Fig. 1.9).

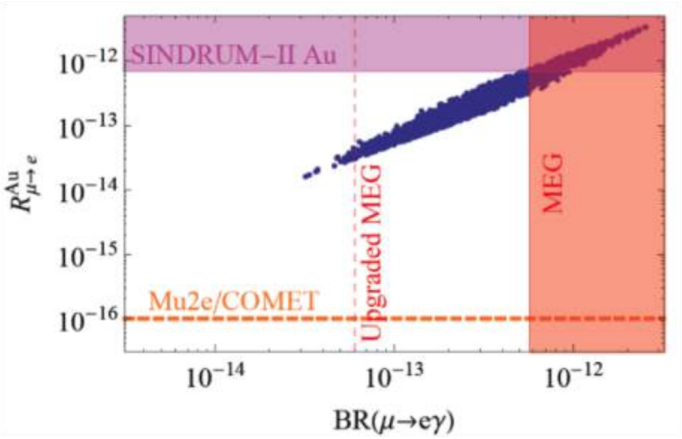

Figure 1.9: *Expected BR and $BR_{\mu e}$ for Left-Right symmetric models for the MEG upgrade and the muon conversion experiments [23].*

1.3 Negative muon conversion

From an experimental point of view, the $\mu-e$ conversion is very attractive. Its signal corresponds to a monoenergetic electron to be separated by a fast falling spectrum background. Since it does not suffer from accidental background, as in the case of $\mu \to e\gamma$ and $\mu \to 3e$, its systematic is completely different from the other two decays.

Indeed, the search for this process has the potential to improve the sensitivity by using a very intensive muon beam.

1.3.1 CLFV experimental searches

The muon was discovered in 1937 by Anderson and Neddermeyer in cosmic rays, with a mass found to be about 200 times the electron mass.

It was believed that the muon decayed into an electron and a neutral particle. It was assumed that if the muon were simply a heavy electron it would also decay into an electron and a γ ray. The first search for $\mu \to e\gamma$ was made by Hincks and Pontecorvo in 1947 exploiting muons from cosmic rays. Its negative result set an upper limit on the branching ratio of less than 10%, but this was the beginning of the search for CLFV.

In 1948, the continuous spectrum of electrons from muon decay was established, suggesting a three-body decay giving rise to a final state of an electron accompanied by two neutral particles. Soon afterwards, the search for the process of neutrinoless muon nuclear capture $\mu\, N(A,Z) \to e\, N(A,Z)$ (where $N(A,Z)$ is a nucleus capturing the muon) was also carried out, but with a negative result. Such searches were significantly improved when muons became artificially produced at accelerators.

A full history and future of the searches in muon CLFV decays is shown in Figure 1.10, where the experimental limits reached during the last 70 years are reported: it is clear that the increase in experimental sensitivity has been getting smaller and smaller and it is only by means of the new generation of experiments that a large leap in sensitivity (by a few orders of magnitude) is achievable.

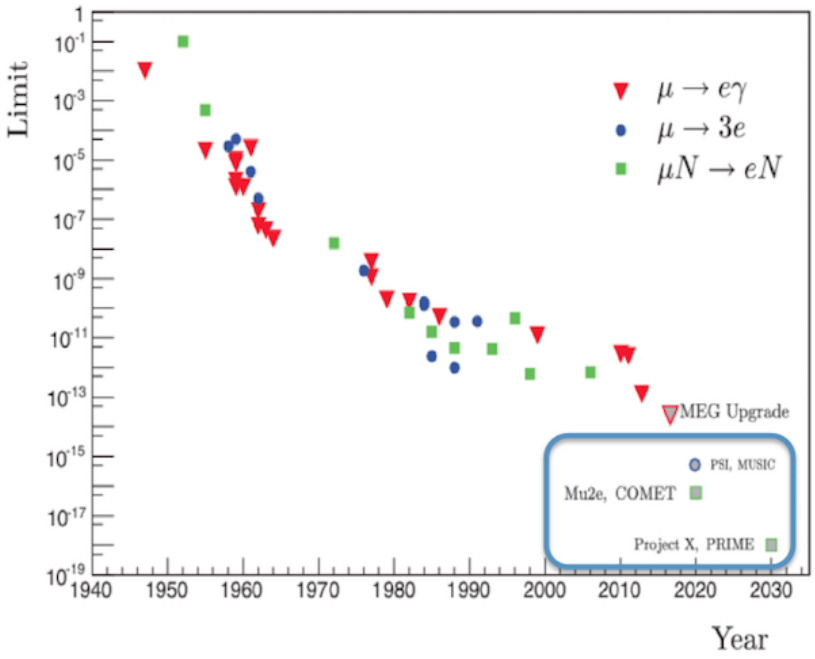

Figure 1.10: *Limits on the branching ratio of the CLFV processes involving muon evaluated experimentally during last years and in future experiments [28].*

The current best experimental limit in muon conversion process is settled by SINDRUM II (PSI, 2006) [26]:

$$BR(\mu^- \text{Au} \ \to e^- \text{Au}) < 7 \times 10^{-13} \text{, @ 90\% CL} \tag{1.3}$$

Each of these rare muon decay searches uses the same experimental method: large numbers of muons are brought to rest hitting a thin target and allowed to decay; stopping the muon is in a well known initial kinematic state (all the energy is in its mass) and so the kinematics of the decay products is well defined.

1.3.2 Signature

The event signature of the coherent $\mu - e$ conversion in a muonic atom is a monoenergetic single electron emitted from the conversion with an energy of:

$$E_e = m_\mu - B_\mu - E^0_{rec} \approx m_\mu - B_\mu \ , \tag{1.4}$$

where m_μ is the muon mass (105.6 MeV), $B_\mu \simeq Z^2\alpha^2 m_\mu/2$ is the binding energy of the 1s muonic atom, which depends by the atomic number Z, and E^0_{rec} is the nuclear-recoil energy. The nuclear-recoil energy is approximately $E^0_{rec} \approx (m_\mu - B_\mu)^2/(2M_N)$,

where M_N is the mass of the recoiling nucleus. Since B is different for various nuclei, the peak energy of the conversion electron signal changes. For instance, it varies from $E_e = 104.3$ MeV for titanium to $E_e = 94.9$ MeV for lead.

In the Mu2e experiment, muons are fired at a thin Al target, where they are stopped and can form a muonic atoms. Then, the muons immediately fall into the 1s ground state, emitting photons. Finally, muons can interact coherently with the whole nucleus and, in the case of $\mu - e$ conversion, will transform into a single electron with a muon life-time of 864 ns and a well-defined energy, 104.96 MeV (since for Al nucleus, $Z = 13$, $A = 27$). The choice of Al results from a tradeoff between conflicting requirements.

Muon conversion process scales as Z^5 (the interaction itself scales by Z^2 and then the probability of the wavefunctions overlapping scales as Z^3) and the BR is normalized to the rate of muon capture (proportional to Z^4). So that, the rate of the muon conversion process scales linearly in Z and so a high-Z material would be preferred. On the other hand, a long muonic atom lifetime is needed. In this way, experiments can collect data in a delayed time window, which means that low-Z materials would be preferred.

Considering both previous statements, the search for the conversion process will be initially conducted using an aluminum target. Other materials will be investigated later, since the rate of a given CLFV operator has a Z-dependence and this study would allow to distinguish among all the NP models beyond the SM.

The Mu2e experiment has also the possibility to measure a similar process with $\Delta L = 2$ [27], where L is the lepton number:

$$\mu^- + N(Z, A) \rightarrow e^+ + N(Z - 2, A) \tag{1.5}$$

which violates both total lepton number and lepton flavor numbers L_e and L_μ and it is related to the the neutrinoless double β-decay. Some theoretical models indicate a rate of this reaction between 10^{-12} and 10^{-14}. Present best limit (@ 90% C.L.) for the BR compared to ordinary muon capture is $< 4.9 \cdot 10^{-10}$, set by TRIUMF experiment [30].

1.3.3 Conversion Rate and Sensitivity

The aim of the Mu2e experiment is to measure the conversion rate of the $\mu - e$ coherent conversion process in a nucleus field, $R_{\mu e}$, defined as the ratio of muon conversion events normalized to the number of muon captures rather than the total number of decays (eq. 1.6).

$$R_{\mu e} = \frac{N(\mu^- + N(Z,A) \rightarrow e^- + N(Z,A))}{\mu^- + N(Z,A) \rightarrow \nu_\mu + N(Z-1,A)} \tag{1.6}$$

If conversion signals will not be observed, the Mu2e experiment will set an upper limit on $R_{\mu e} < 6 \times 10^{-17}$.

The Single Event Sensitivity (SES) is defined as that conversion rate for which the expected number of events will be one. It depends on the total number of stopped muons, the fraction of stopped muons that are captured (this depends on the nucleus), and by the efficiency of the experiment. The Mu2e experiment will rich a SES of $\sim\ 2.7 \times 10^{-17}$.

1.4 Physics background

The Mu2e experimental concept is simple: to create a negative muon beam, protons interact with a primary tungsten target to create charged pions, which are focused and collected by the magnetic lenses. Then pions mainly decay into muons. Low momentum and negative muons are transported to a thin stopping aluminum target, where they stop at high rate ($\sim$ 10 GHz). Active detector components (tracker + calorimeter) will measure the energy and momentum of the particles originating from the stopping target. The detector system starts taking data after 670 ns from the arrival of the proton pulse. The delayed acquisition time-window is fundamental to discriminate CEs from background processes (see Cap. 2).

Indeed, to reach experimental sensitivity, it is mandatory to keep under control all background events. There are many different processes that might obscure or mimic a conversion signal:

- intrinsic physics backgrounds arising from muons stopping in the target, where

they are captured in an atomic excited state and promptly fall to the ground state. For aluminum, about 39% of the muons will decay in orbit (DIO), while the remaining 61% will be captured on the nucleus, producing electrons, photons and neutrons from the atomic cascade (Fig. 1.11). DIO events are the most important intrinsic physics background processes. A high resolution detector reduces the effect of these backgrounds since, neglecting resolution effects, there are no intrinsic physics backgrounds that have the same energy as the electron from conversion signal energy;

- beam-related delayed backgrounds are events from the main proton pulse, but which arrive late at the stopping target section (for example, antiprotons or neutrons). These backgrounds can be reduced by having a sufficiently long muon beam line and using a time delayed acquisition window. Antiprotons are reduced to a negligible contribution by means of a specific absorber in the middle section of the Transport Solenoid;

- beam-related prompt backgrounds arising from contamination of the muon beam, causing electrons with an energy close to the region of conversion electrons. The impact of these events are greatly reduced by using a bunched proton beam and recording only data in a delayed time window, an example is the radiative pion capture process (RPC). However, these prompt backgrounds could still cause problems if there are protons leaking out of the main proton pulses and into the gaps between them. Therefore, a high level of "extinction", defined as the ratio of beam between pulses to the beam contained in a pulse, of secondary proton pulses is required to achieve the design SES. This contamination is due to three main sources. Pions that have not decayed by the time the beam reaches the stopping target can be captured immediately by the nucleus. Secondly, a small fraction of pions can decay directly in high energy electrons (despite having a small BR of 1.23×10^{-4}) and are important for the high intensity beams that will be used. Finally, muons can decay in flight and, if they have a momentum greater than 77 MeV, could produce an electron with an energy in the conversion signal region;

- other backgrounds are caused by electrons or muons initiated by cosmic rays, which can induce a background event in the detector but can easily be ac-

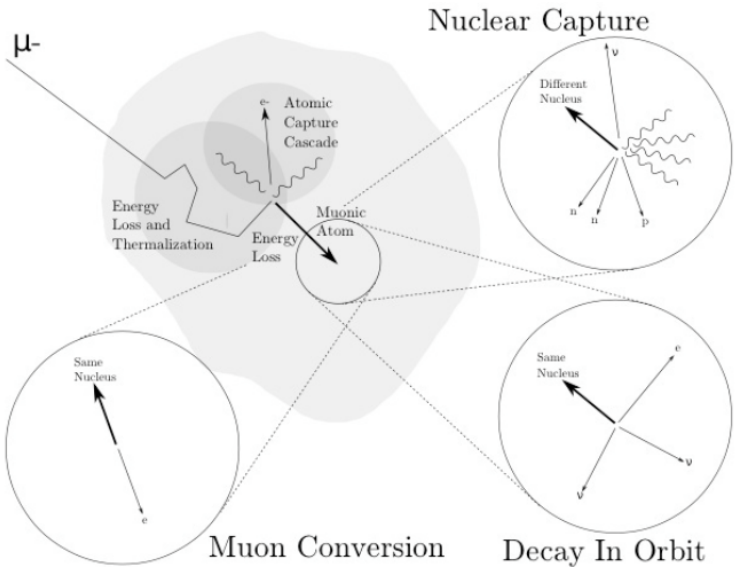

Figure 1.11: *A muon stopped in the aluminum target can be captured in an atomic excited state and promptly fall to the ground state. For aluminum, in addition to the electron conversion process, ∼ 39% of the muons will decay in orbit, while the remaining ∼ 61% will be captured on the nucleus, producing electrons, photons and neutrons from the atomic cascade.*

counted for by using a cosmic ray veto (CRV).

The Mu2e rate of background activity scales linearly with beam intensity and the main sources are described in more detail in the following sections.

1.4.1 Decay in Orbit

In the SM, a muon bound in the atom can undergo a decay-in-orbit (DIO). In this case, since the muon is captured in the atomic orbit, the decaying electron can exchange momentum with the nucleus. This result in a small, but not null, probability to reach the same energy of a conversion electron.

In a free muon decay, the electron energy would not exceed 52.8 MeV, which occurs when the electron and two neutrinos are emitted in opposite directions and is equal to half of the mass of the muon. However, in the DIO case the nucleus can take away some of the electron momentum which, being non-relativistic, means it can take momentum out of the system without taking any significant energy. Therefore, electrons can essentially recoil off the nucleus and thus have more energy

than the free muon decay limit. However, the electrons cannot take all of the energy (the two neutrinos will take some) and so the end point of the DIO spectrum is slightly lower than the energy of conversion signal.

The DIO electron energy spectrum has been calculated by Czarnecki et al. [12] and is shown in Figure 1.12 .The nucleus recoil results then in a small tail after 52.8 MeV (going as $1/m_{\mu}^{5}$) and appears to vanish at 60 MeV. However, looking at the DIO spectrum on a log scale, it can be seen that the occurrence of DIO electrons above 100 MeV is still at an appreciable level relative to a signal with a branching ratio of $\mathcal{O}(10^{-17})$.

To date, there are no measurements of DIO spectrum near the conversion electron energy, because of the high muon rate needed. However, a recent theoretical calculation [12], which takes into account nuclear effects, gives an uncertainty near the endpoint smaller than 20%.

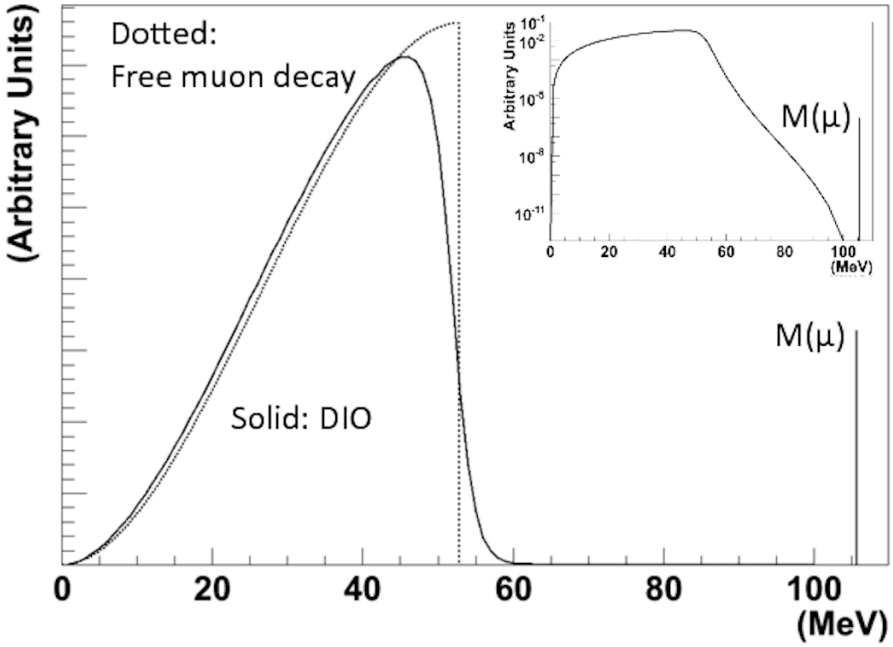

Figure 1.12: *The signature of $\mu - e$ conversion is a monoenergetic electron near the muon rest mass. Moreover, muons captured by the nucleus target can decay-in-orbit. DIOs spectrum shape is a distorted Michel spectrum with a long tail to high energies. The inset shows this DIO spectrum on a log scale: the spectrum extends all of the way out to the endpoint energy, about 0.5 MeV less than the muon mass, for this reason these events represent an important background for the Mu2e experiment.*

1.4.2 Radiative muon captures

The muon can be absorbed by the nucleus of the target, emitting a high energy photon, $\mu + N(Z, A) \rightarrow \gamma + \nu_\mu + N(Z-1, A)$, which can convert to e^+e^- pairs. It is possible, however, to choose the target material in order to reduce the energy of the resulting photon. For example, the resulting photon energy endpoint for an aluminum target is 101.9 MeV, about 3.1 MeV below the conversion electron signal energy, because the minimum mass of the Mg (Z=12) is a couple of MeV above the rest mass of Al (Z=13).

1.4.3 Antiprotons induced backgrounds

Antiprotons, which can be generated along with the muons by the parent proton beam or by cosmic rays, can be coincident in time with a conversion electron, having also the same energy. The products of their interaction with the matter can be also a source of background because they do not decay and carry a negative electric charge.

Antiprotons with momenta less than 100 MeV can propagate and reach the stopping target. Those with momenta less than 100 MeV spiral slowly, consequently the expected flux of antiprotons at the muon stopping aluminum target is nearly constant in time so that the delayed live gate and the extinction systems do not effectively mitigate the resulting backgrounds. Moreover, antiprotons will annihilate on nuclei, releasing significant energy and producing a significant number of secondary particles. These secondaries can include electrons themselves, or they can produce electrons in tertiary interactions such as capture or decay.

To prevent antiprotons reach the stopping target region, a thin absorbers will be placed before this region (upstream in the Transport Solenoid, see Ch. 2).

1.4.4 Radiative pion capture

Pions can induce background events when they are captured in the stopping target or surrounding material and produce a high energy photon through RPC:

$$\pi^- + N \rightarrow \gamma + N^* \tag{1.7}$$

The kinetic endpoint of the emitted photons peaks at ~ 110 MeV which can also e^+e^- pairs. If the photon then converts in the stopping material, one sees an electron-positron pair and in the case of an asymmetric conversion, the outgoing electron can be near the conversion energy, thus appearing to be a conversion electron. In addition, the photon can internally convert:

$$\pi^- + N \rightarrow e^+ \; e^- \; + N^* \tag{1.8}$$

Thus electrons resulting from photon conversions, both internal and external, can produce background.

RPC occurs in 2.1% of pion captures for an aluminum target. This kind of background can be reduced using a pulsed beam and an appropriate delayed acquisition time-window.

1.4.5 Other environmental backgrounds

Other activity in the detector might affect track reconstruction, thus causing tails in the energy resolution response function that can move low-energy DIO electrons into the signal momentum window. Additional activity in the detector primarily originates from the muon beam, from multiple DIO electrons, and from muon capture on target nucleus that results in the emission of photons, neutrons and protons.

The protons ejected from the nucleus following muon capture have a very small kinetic energy and are highly ionizing, so the large pulses they leave behind in tracking chambers can shadow hits from low energy electrons, potentially adding to the likelihood of reconstruction errors. Ejected neutrons can be captured on hydrogen or other atoms and produce low-energy photons.

Low-momentum electrons can be created in the tracker by photons that undergo Compton scattering, photo-production, or pair production, and by delta-ray

emission from electrons and protons. Because of the low mass of the tracker, these electrons can spiral a considerable distance through the detector before they range out, generating a substantial number of in-time hits.

Electron-generated hits caused by neutron-generated photons are the most common and difficult to remove form of background activity.

Chapter 2

The Mu2e experiment

The Mu2e experiment will search for the charged lepton flavor violating (CLFV) process of neutrinoless coherent muon conversion in the field of an Aluminum nucleus. The goal of the experiment is to measure the ratio of the conversion rate, normalized to the rate of nuclear muon capture, with an improvement of four orders of magnitude on the current limit set by SINDRUM II (PSI, 2006) [26]:

$$R_{\mu e} = \frac{\mu^- + N(Z,A) \rightarrow e^- + N(Z,A)}{\mu^- + N(Z,A) \rightarrow \nu_\mu + N(Z-1,A)*} < 6 \cdot 10^{-17} \,(@\, 90\% CL), \tag{2.1}$$

that corresponds to a SES of 2.7×10^{-17}.

Mu2e is being built at the Fermi National Accelerator Laboratory (Fermilab - Batavia, IL) near Chicago. The experiment received the US Department of Energy's critical-decision 2 (CD-2) approval in March 2015. This officially sets the baselines in the scope, cost and schedule of the experiment. At the same time, the Mu2e collaboration was given authorization to begin fabricating the solenoids and to begin the construction of the experimental hall, which saw ground-breaking on April, 18. By nowadays schedule, the Mu2e experiment will start to take first data at the end of 2020.

2.1 Comparison with other experiments

CLFV processes research started at the half of last century, when Hincks and Pontecorvo set the first upper limit on the $\mu \to e\gamma$ decay (Fig. 1.10). Then follow a rich history of searches for charged lepton flavor violating processes in the muon sector. The experiments exploiting muons are the most promising in this field. Such experiments have been constructed to reveal three main processes: the $\mu \to e\gamma$ decay, the muon decaying in three electrons $\mu^+ \to e^+e^-e^+$ and the coherent muon conversion in a nucleus field.

The most recent results for charged lepton flavor violating $\mu \to e\gamma$ decay are given by MEG experiment (PSI), which has set an upper limit of $BR(\mu \to e\gamma) < 5.7 \times 10^{-13}$ (at 90% CL) [14]. The MEG collaboration is also planning to start a new run with an upgraded apparatus in 2016, which will improve this limit of 1 order of magnitude.

The actual upper limit on the $\mu^+ \to e^+e^-e^+$ is $BR(\mu^+ \to e^+e^-e^+) < 1 \times 10^{-12}$ (at 90% CL), set by SINDRUM experiment [26]. The Mu3e experiment at PSI will improve this limit, reaching a new experiment sensitive to BR of $\sim 10^{-15}$ (2017).

In 2000, SINDRUM II has also set the upper limit for muon to electron conversion in the field of a nucleus at $R_{\mu e} < 7 \times 10^{-13}$ [26], using a 53 Mev muon beam and a gold target. Currently, not only Mu2e, but also an analogous experiment searching the coherent muon conversion, COMET at J-PARC (Japan), is in development phase, aiming to reach a similar sensitivity.

2.1.1 MEG

The MEG experiment is searching for the $\mu \to e\gamma$ decay. The experimental setup is shown in Figure 2.1. Exploiting the most intense continuous muon beam in the world and very innovative detectors, the MEG experiment has set an upper branching ratio limit of about 5×10^{-13} (2013), which is about two orders of magnitude improved from the previous limit ($BR < 1.2 \times 10^{-11}$), set by MEGA (2001) [14].

The signature of $\mu \to e\gamma$ decay has a back-to-back topology: the positron and gamma are emitted concurrently at 180° and with the same energy ($\sim$ 53 MeV, half

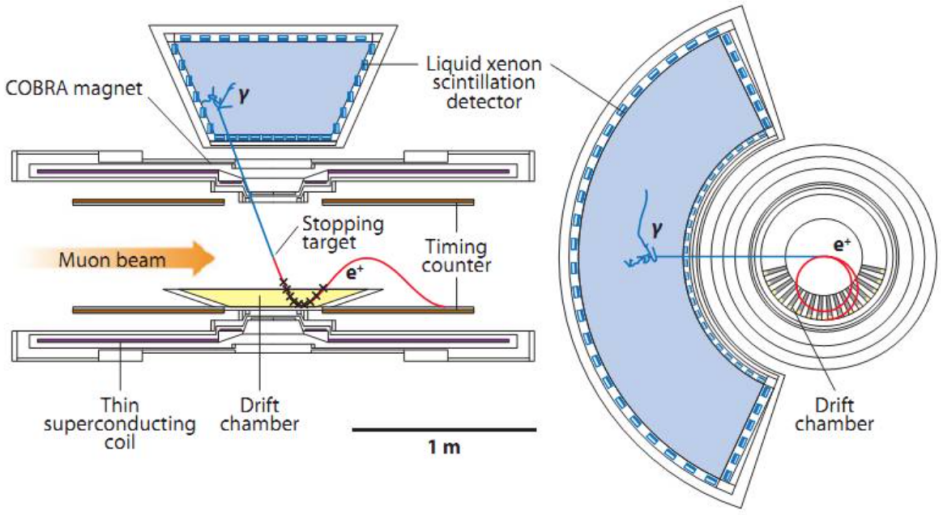

Figure 2.1: *Schematic layout of the MEG detector, showing one simulated event coming from the stopping muon target.*

muon mass). The MEG detector has been designed to distinguish the coincident back-to-back $\mu \to e\gamma$ events from the main high rate background of normal and radiative muon decays. On the detection side, two main components made possible the required energy, momentum, spatial and timing resolutions: a 800 l of liquid xenon (LXe) fast calorimeter (to detect prompt γ) using scintillation light together with a gradient-field and a thin-coil superconducting positron spectrometer. The LXe photon calorimeter is viewed from all sides by $\sim$ 800 photomultiplier tubes immersed in the cryogenic fluid and it allowed a homogeneous measurement of the energy, spatial and timing coordinates of the photon. The gradient magnetic field of the COBRA (Constant Bending-Radius) spectrometer allows the decay positrons to execute spiral paths of constant projected bending radius and increasing axial pitch, which depend entirely on the particle's total momentum while being independent of its emission angle. This allows a background of lower energy Michel positrons to be swept away more effectively from the fiducial tracking volume of the azimuthally spaced, staggered-cell drift chambers. Timing information and hence trigger information for events is provided by a set of fast, double-layered, orthogonally placed timing-counter arrays, positioned at either end of the magnet.

The analysis results of a combined data set, totaling 3.6×10^{14} stopped muons on target, of the MEG experiment is reported in Figure 2.2. The photon energy as a

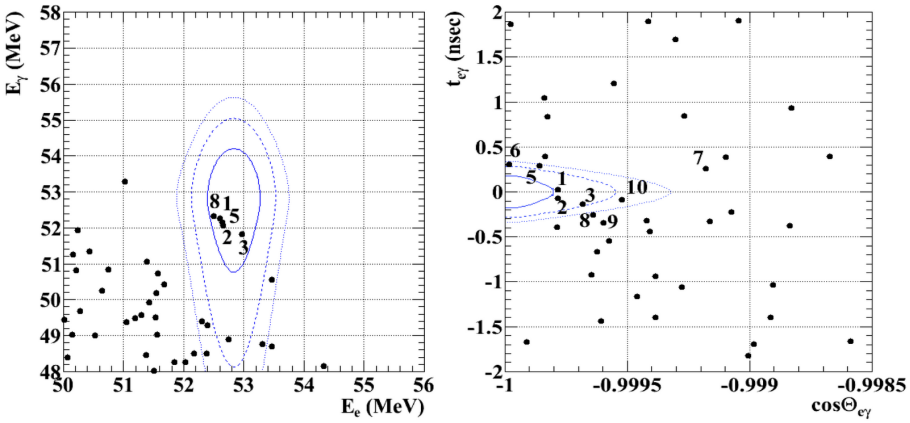

Figure 2.2: *Event distributions for the combined 2009-2011 data set in the (E_e, E_γ) and ($cos\theta_{e\gamma}$, $t_{e\gamma}$) planes. In the left (right) panel, a selection of $|T_{E\gamma}| < 0.244$ ns and $cos\theta_e < 0.9996$ with 90% efficiency for each variable ($52.4 < E_e < 55$ MeV and $51 < E_\gamma < 55.5$ MeV with 90% and 74% efficiencies for E_e and E_γ, respectively) is applied. The signal PDF contours (1, 1.64 and 2 σ) are also shown [16].*

function of the electron energy (left) and their relative emission time as a function of the opening angle between electron and γ are shown. The data collected show no excess of events compared to background expectations and allow to set a new upper limit on the BR of this decay of 5.7×10^{-13} (at 90% CL), which represents the world best limit[16].

2.1.2 Mu3e

The Mu3e experiment (PSI) will search for the CLFV decay of a muon to three electrons, $\mu^+ \to e^+e^-e^+$ [25].

More than $> 10^{16}$ muon decays will be observed (2017). This enormous number of muons will be reached by utilizing the world most intense muon beam, which produces $> 10^8$ muons/s decaying in the Mu3e detector. In order to filter out the few decays $\mu^+ \to e^+e^-e^+$ they must be excellently discriminated from possible background.

The dominant background contribution comes from accidental tracks coincidences from $\mu^+ \to e^+\overline{\nu}_\mu\nu_e$ decays as well as from the radiative decay with internal

conversion $\mu^+ \to e^+e^-e^+\overline{\nu}_\mu\nu_e$. The suppression of accidental background is reached through excellent timing and vertex (decay point) resolution. The background from $\mu^+ \to e^+e^-e^+\overline{\nu}_\mu\nu_e$ is suppressed by measuring the missing energy carried away by the two neutrinos. This is best achieved by a precise determination of electrons momenta in a magnetic spectrometer. The Mu3e detector has been designed to detect the signal process, namely two positrons and an electron from a common point in space and time, operating at such high rates. Moreover, to reduce the background to below 10^{-16} level, a good vertex (< 200 μm), time (< 100 ps) and momentum (< 0.5 MeV) resolutions are needed.

The Mu3e experimental setup is shown in Figure. 2.3. The requirements stated are met by using 50 μm thin high-voltage monolithic active pixel sensors in conjunction with an innovative tracking concept. The timing resolution is provided by a combination of scintillating fibers and tiles.

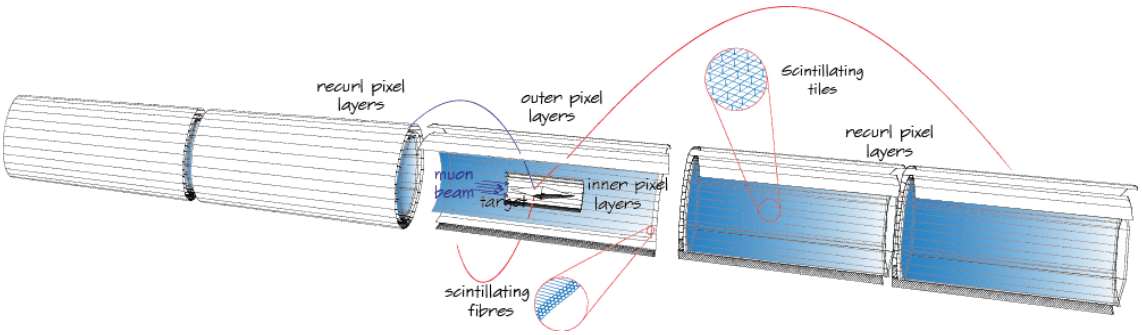

Figure 2.3: *Schematic layout of the Mu3e experiment at PSI.*

From 2017, the high intensity muon beam line should become available, allowing for a push towards a sensitivity of 10^{-16} at the end of this decade.

2.1.3 SINDRUM

The SINDRUM experimental setup is shown in Figure 2.4. A muon beam was produced by a 590 MeV proton beam hitting a carbon production target. The backward produced particles (π, μ and e) were transported by a secondary beam line to a degrader connected to the Transport Solenoid with a 1.2 T magnetic field. A gold target was used to stop muons. The conversion electron (CE) energy for gold is

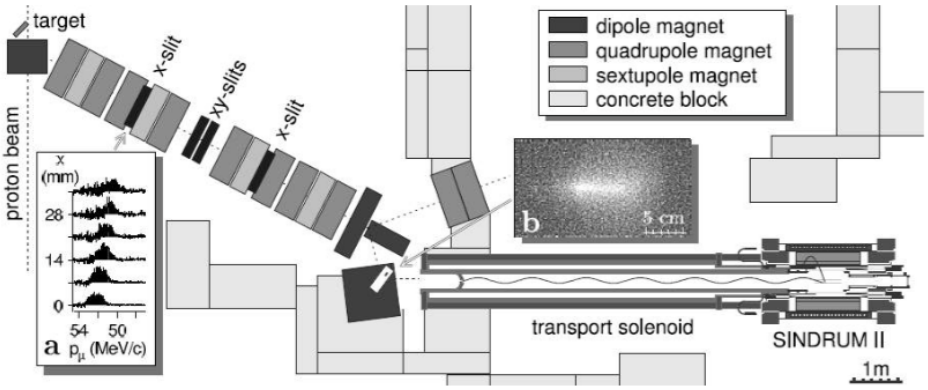

Figure 2.4: *Schematic layout of the SINDRUM II experiment at PSI.*

95.6 MeV. The helical trajectories of the emitted electrons were reconstructed by two drift chambers, while scintillation and Čerenkov hodoscopes were used for the trigger and for the timing of the track elements and electron identification. A scintillation beam counter in front of the target helped to recognize prompt background electrons produced by radiative capture of beam pions or beam electrons scattering off the target (Fig. 2.4).

After 25 days of run, a total of 4.9×10^{12} muons were stopped. A spectrometer measured the electrons energy, operating inside a superconducting solenoid with a 1 T magnetic field. The pion contamination was reduced by a factor of 10^6 by passing the beam through a thin moderator that reduced the muon flux by 30%. The few surviving pions had very low momentum and a simulation showed that ∼99.9% of them decayed before reaching the target. Electrons from radiative pion capture in the moderator could reach the target and scatter into the detector solid angle. This background was easily recognized since it was strongly peaked in the forward direction and had a characteristic time correlation with the cyclotron (RF $\sim$ 20 ns). The electron spectrum agreed well with the predictions for DIOs [12], but no events were observed with energies consistent with the muon-to-electron conversion hypothesis resulting in a limit of 4.3×10^{-12} (@ 90% CL).

In 2000, SINDRUM II performed a new search for muon to electron conversion using a 53 MeV muon beam. During a 75-day live time 4.4×10^{13} muons were stopped. After removing forward prompt events, the electron spectrum was well described by DIOs spectrum (Fig. 1.12) and no events were observed in the signal region. One

electron event, thought to be pion induced, was identified at higher energy. A final limit on muon to electron conversion in gold was set at 7×10^{-13}(@ 90% CL) [26].

2.1.4 COMET

The COMET experiment aims to study the $\mu - e$ coherent neutrinoless conversion in the field of an aluminum nucleus, such as the Mu2e experiment, improving by a factor of 10^4 the upper limit on the $R_{\mu e}$, with a $\sim 3 \times 10^{-17}$ sensitivity.

This project is being build at J-PARC (Japan) with a different approach, with respect to Mu2e, to achieve an early start of a series of searches for the muon conversion: the Phase-I presents the first part of the staged construction of the experiment and it would include the COMET proton beam line and the COMET muon beam line up to the end of the first 90∘ bending magnet, as shown in Figure 2.5 (left).

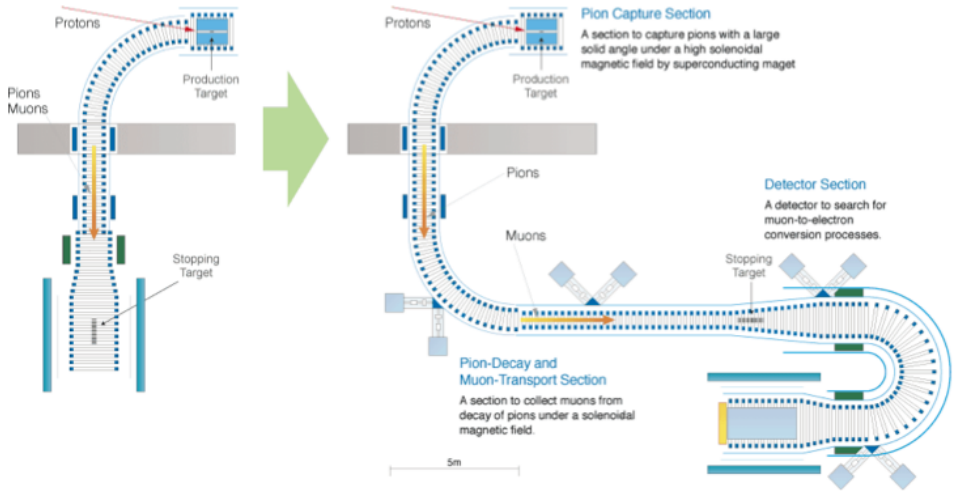

Figure 2.5: *Schematic structure of the Phase I (left) and II (right) of the COMET experiment at J-PARC, searching for the $\mu - e$ coherent conversion in an aluminum nucleus field.*

The experiment will use a dedicated 8 GeV proton beam for both phases. Muons will be produced from the pions emerging after collisions of the 8 GeV proton beam with a graphite target. In the first stage of the experiment, muons are selected using a transport solenoid before being stopped in an aluminum target at the center of a cylindrical drift chamber in a 1 T magnetic field.

In absence of a signal, the first phase of COMET will set an upper limit on the conversion rate of: $R_{\mu e} < 7.2 \cdot 10^{-15}$. The first stage, as well as improving the best limit for this type of muon conversion, will also provide an estimatation of backgrounds (inter-bunch extinction factor, presence of secondary particles, background processes), helpful for the second stage.

The COMET Phase-II, which has still to be approved, will provide a second "C-shaped" section, the electron spectrometer, which allows to transport the produced electrons from the target to the detector while introducing a cut on muon momentum and eliminating protons from nuclear captures. It also helps to suppress low energy uncharged events (neutrons, photons) coming from the target, allowing to reach a final SES of 2.6×10^{-17}.

2.2 The Mu2e experimental setup

The layout of the Mu2e apparatus shows a "S-shape" (Fig. 2.6): the entire system is surrounded by the Superconducting Solenoid Magnet System. The entire experimental setup is extensively described in the Technical Design Report of the experiment [28].

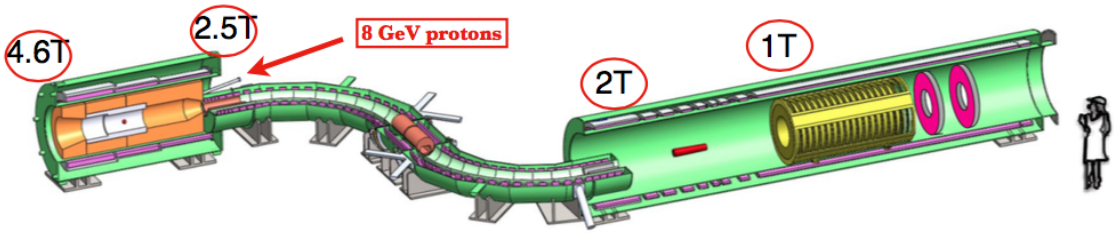

Figure 2.6: *Layout of the Mu2e experiment. It consists of three superconducting solenoid magnet: from left to right, the production solenoid, the transport solenoid and the detector solenoid.*

It consists of three superconducting solenoid magnets. The inner bore of the solenoids is evacuated to 10^{-4} Torr in order to limit backgrounds from muons that might stop on gas atoms and to reduce the contribution of multiple scattering for low momentum particles. The Mu2e project is structured as follows:

- a bunched proton beam produces an intense secondary pulsed muon beam

with a structure that allows enough time for most of the stopped muons to decay before the next pulse arrives;

- the Production Solenoid (PS) where the 8 GeV proton beam coming from the Fermilab accelerator system enters, hitting the production target;
- the Transport Solenoid (TS), which efficiently captures charged pions and transports negatively charged secondary muons to a stopping target. The S-shaped Transport Solenoid is long enough to allow the decay of almost all hadrons and to suppress line-of-sight particles. The momentum spectrum of the transported muon beam must be low enough to ensure that a significant fraction of the muons can be brought to rest in a thin target;
- the Detector Solenoid (DS) which is capable of efficiently and accurately identify and analyze CEs with energy around 105 MeV produced by the muon beam hitting the thin aluminum target. Moreover its design allows backgrounds rejection from conventional processes and cosmic rays;
- a detector hall facility to house the experimental apparatus.

So that, the Mu2e experimental concept is simple: in the PS, to create a negative muon beam, protons interact with a primary tungsten target to create charged pions, which are focused and collected by the lens provided by the graded magnetic field in the TS, where they mainly decay into muons. Low momentum and negative muons are transported to a thin stopping aluminum target, in the DS, where they stop at high rate ($\sim$ 10 GHz). Active detector components (tracker + calorimeter) will measure the energy and momentum of the particles originating from the stopping target and discriminate CEs from background processes. A Cosmic Ray Veto (CRV) system surrounds the DS to make negligible the contribution due to cosmic rays.

2.2.1 The accelerator system

The Mu2e experiment needs a high intensity and bunched proton beam to produce a secondary intense beam of low energy muons with the time structure required by the experiment (Fig. 2.7).

The existing Fermilab accelerator complex will take 8 GeV protons from the Booster, rebunch them in the Recycler, and slow-extract them to the experimental apparatus from the Muon Campus Delivery Ring, which was formerly the anti-proton Accumulator/Debuncher ring for the Tevatron (Fig. 2.7). Mu2e will collect about 4×10^{20} protons on target, resulting in about 10^{18} stopped muons, which will yield a single-event sensitivity for coherent muon conversion of 2.7×10^{-17} relative to normal muon nuclear capture.

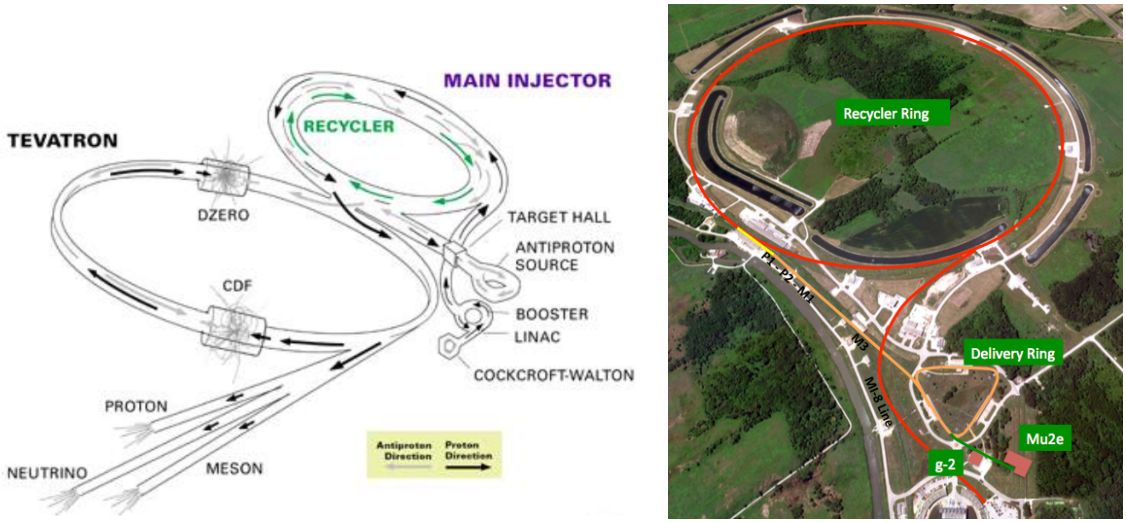

Figure 2.7: *Layout (left) and picture (right) of the Mu2e facility relative to the accelerator complex that provides proton beam to the detector. Protons are transported from the Booster through the MI-8 beamline to the Recycler Ring where they will circulate while they are re-bunched by a 2.5 MHz RF system. The reformatted bunches are kicked into the P1 line and transported to the Delivery Ring where they are slow extracted to the Mu2e detector through a new external beamline.*

The upgrades to the Fermilab accelerator complex necessary to run the Mu2e experiment are distributed over several projects. These projects will transform the Fermilab Antiproton Source into what is now called the Muon Campus, which will support the operation of the Muon g-2 and the Mu2e experiments.

Booster protons are extracted and injected into the Recycler Ring. As each batch circulates in the Recycler Ring it is re-bunched with a 2.5 MHz RF system to form four bunches with the bunch characteristics required by the Mu2e experiment. After the 2.5 MHz bunch formation, the beam is extracted from the Recycler, one bunch at a time, and transported to the Delivery Ring. The beam is then resonantly

extracted and transported to the Mu2e production target. After the resonant extraction sequence is complete, a cleanup abort kicker is fired to remove any remaining beam.

Protons designated for Mu2e are acquired from the Booster synchrotron by utilizing the unused portions of the Main Injector timeline during slip-stacking operations for NOνA. The flux of protons striking the primary target between beam pulses must be suppressed by a large factor, in order to reduce backgrounds. While these protons collide against the production target, a pair of high-frequency dipoles will sweep all but the desired beam out of the beam path (extinction method). It is important that for every proton in the beam pulse, there are fewer than 10^{-10} out-of-time protons.

In order to achieve the designed single event sensitivity, the produced muon beam must follow strict requirements:

- High rate: a larger number of muons stopped is essential to improve previous experiments results. The present proposed rate is of $4.21 \cdot 10^{10}$ μ^-/s.
- Pulsed structure: in order to suppress the prompt background, the muons hitting the stopping target should be distributed in a narrow time burst (< 200 ns), each one separated by the other by intervals of ~ 1500 ns (larger than the muonic aluminum lifetime).
- No veto: the result of SINDRUM II experiment was ultimately limited by the presence of the veto counters, necessary for the suppression of the prompt background. Mu2e, instead, will take data after 670 ns the injection bursts, to let the prompt background (especially pion capture) to subside. The data-taking time window will then close 925 ns after, just before the arrival of the next bunch. Veto counters are then no longer needed. Given the time scheme provided by the Fermilab accelerator complex, the muon capture time in Al maximizes the total number of muons on target (Figure 2.8).
- Extinction: between-bursts extinction is fundamental to suppress background generated by unwanted beam between pulses.

The timing structure which satisfies these requirements is summarized in Figure

2.8. The proton beam hits the production target with bursts 200 ns large and separated from the next one by ∼1700 ns. The detector system starts taking data after 670 ns the arrive of the proton pulse, when almost all pions are decayed. Muon capture in Al has a life time $\tau \sim 864$ ns, so it best matches this timing scheme.

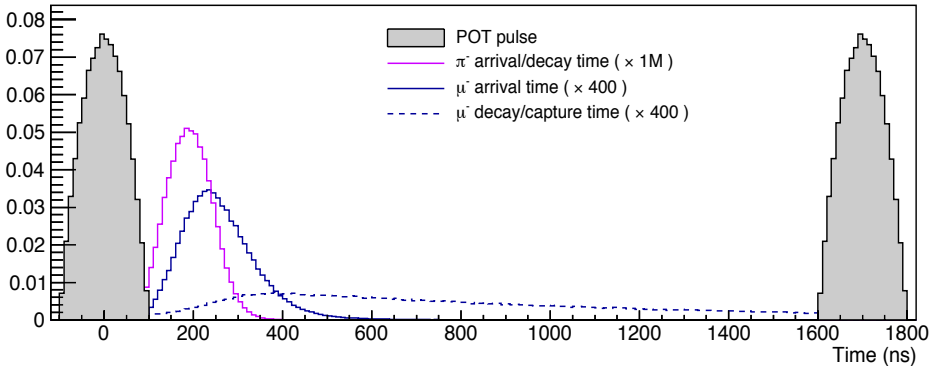

Figure 2.8: *The proton beam hits the production target with bursts 200 ns large and separated from the next one by ∼1700 ns. The detector system starts taking data after 670 ns from the arrival of the proton pulse, when almost all pions are decayed. Muon capture time in Al (dashed blue line) best matches this timing scheme.*

2.2.2 The Production Solenoid

The first stage of Superconducting Solenoid Magnet System is the Production Solenoid (PS), which must collect and focus pions and muons generated by the interaction between the 8 GeV bunched proton beam coming from the accumulator ring and the production target, placed in the center of the solenoid (Fig. 2.9).

The flux of particles coming from the proton pulse striking the production target during the early burst is referred as "beam flash". In order to reduce the flux of secondary particles, the primary proton beam enters the PS from the opposite direction of the Transport Solenoid (TS) (Fig. 2.6): the required high number of stopped muons is then achieved applying a graded solenoidal magnetic field, B, from 4.6 T to 2.5 T. In this way, the protons move in the direction of increasing field strength: the graded field, then, increases the pitch angle, defined as $\sin\theta = p_t/p$ (where p_t is the transverse momentum), of the interaction products of selected charge, directing

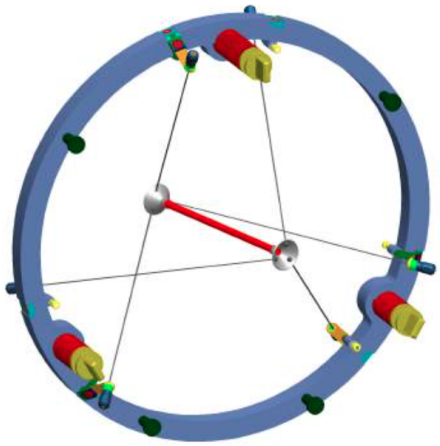

Figure 2.9: *Tungsten stopping target for proton beam.*

them into the part of the PS with lower field. The graded field helps also to recover some interaction products emitted backwards: the p_t/p ratio, in fact, decreases as B decreases, enhancing the particle movement in the direction of decreasing gradient. This approach has been already validated by the MuSIC experiment R&D (at J-Park) [29]. The production target consists of a tungsten rod, 160 mm long and with a 6.3 mm diameter, placed within a titanium support ring (Fig. 2.9). The tungsten has been chosen as target material because of its thermal properties: the high melting point and the low thermal expansion coefficient. The PS coils, made of Al-stabilized NbTi cables, are then protected from radiation damage by a bronze shield.

2.2.3 The Transport Solenoid

The Transport Solenoid consists of a set of superconducting solenoids which must transmits low energy negatively charged muons ($p < 80$ MeV/c) from the PS to the Detector Solenoid (DS). The S-shape suppresses the line-of-sight neutral particles, while highly energetic negatively and positively charged particles are suppressed by several absorbers and collimators. A charged particle beam traversing a curved solenoid will drift perpendicular to the its axis, with opposite direction for opposite charged particle. In the collimator region there is also an absorber to reduce the contribution due to antiprotons.

In order to suppress late arriving particles to the DS, the magnetic field is slightly graded (from 2.5 T to 2 T): possible traps, where the particle bounces for a while between two local field maxima, are then eliminated.

A cosmic ray veto device covers also the part of the TS close to the DS entrance.

2.2.4 The Detector Solenoid

The upstream section of the Detector Solenoid (DS) houses the muon stopping target, the tracker, which measures the particles momenta, and the calorimeter in the downstream part, which measures particle energy and their arrival time (Fig. 2.10). Moreover, in the downstream part of the DS, there is the muon beam stop, which is made by an high-Z material, to absorb the energy of the muons which did not interact with the stopping target.

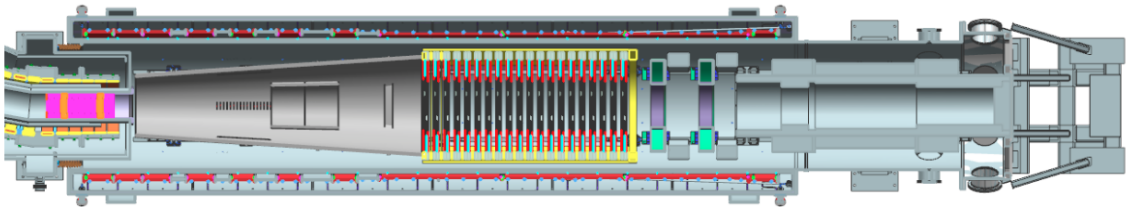

Figure 2.10: *The Detector Solenoid is a large, low field magnet that houses the muon stopping target and the components required to identify and analyze CEs from the stopping aluminum target.*

All these devices have to operate in a graded magnetic field, which is around 2.5 T, at the beginning of the solenoid, and is about 1 T in the region occupied by the tracker, becoming almost uniform till the end of the DS. The graded field allows to accelerate particles from the TS to the detector area, increases the acceptance for conversion electrons (the conversion electrons emitted in the direction opposite the detector components are gradually reflected backwards) and also helps in rejecting beam-related backgrounds.

Furthermore, the graded field of the first part of the DS captures part of the CEs that are emitted in the opposite direction with respect to the detector components, causing them to reflect back towards the detector. Not all of these reflected electrons will be used in the final data sample, because many of them will pass through nearby material, losing energy or scattering and failing the analysis cuts.

The muon stopping target has to be at high-Z enough to stop a significant fraction of muons coming from the TS, but not so massive to corrupt the momentum measurement of conversion electrons emerging. It is composed by 17 thin aluminum foils (Fig. 2.11, left) arranged along the first part of the DS axis. The design of the stopping target is the result of a trade off between the stopping efficiency and the amount of material traversed by the eventual conversion electron. Figure 2.11 (right) shows the conversion rate as a function of the atomic number (Z) of the stopping target material: the eventual dependence of the conversion electron rate from the target material could help to identify the physics mechanism responsible for the process.

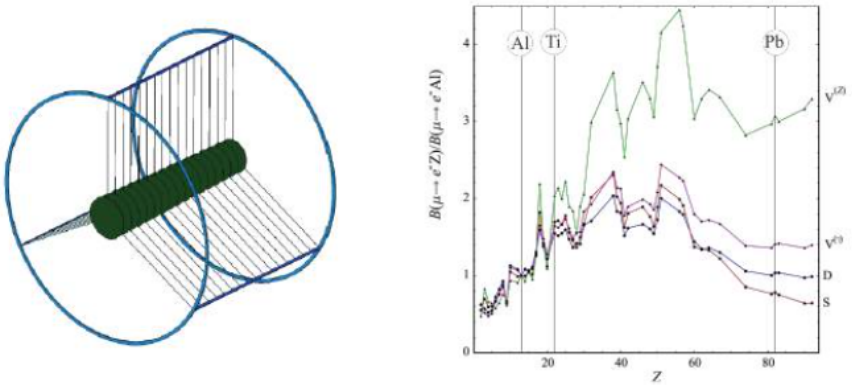

Figure 2.11: *Left: schematic layout of the Mu2e stopping target and its mechanical support. It is made by 17 aluminum disks, 0.22 mm thick, spaced 5 cm along the DS axis. The disks radius decreases from 8.3 cm upstream to 6.3 cm downstream. Right: $R_{\mu e}$ material target dependence, for single operator dominance model, normalized to the aluminum value.*

2.2.4.1 The Tracker

The tracker has to accurately measure the trajectory of 105 MeV CEs, operating in an almost uniform 1 T magnetic field, in order to calculate their momentum. Moreover, it must reject backgrounds and operates in vacuum (the bore is evacuated to 10^{-4} Torr).

The material of the tracker must be as low as possible to minimize multiple scattering in the tracker, which is the main source of reconstruction errors. Moreover, the high rates of the Mu2e environment can generate background from spurious hits

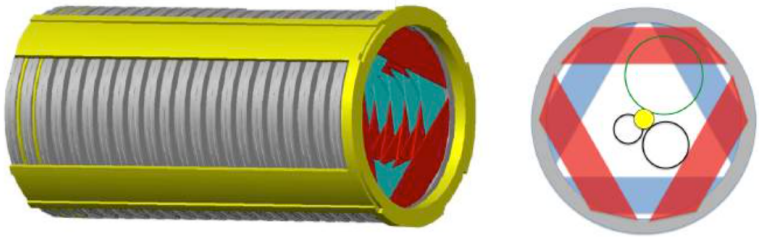

Figure 2.12: *Left: The Mu2e straw tube tracker. The straws are oriented transverse to the solenoid axis. Right: cross sectional view of the Mu2e tracker station with the trajectories of a 105 MeV CE (top) and a 53 MeV Michel electron (lower right) superimposed. The disk in the center is the stopping target. Electrons with energies smaller than 53 MeV (lower left) miss the tracker entirely.*

of lower energy particles, which can combine mimicking a CE trajectory. Indeed, a low mass and highly segmented detector is required to minimize multiple scattering and handle the high rates.

The actual design plan provides 18 measurement stations, assembled to resemble an annular disk (Fig. 2.12): all the electrons with $p < 53$ MeV will pass through the central hole, increasing the tracker purity.

Each station is made of about 200 Mylar straw tubes, 5 mm wide, 15 μm thick with a 25 μm sense wire inside. Each station is arranged in two planes (Fig. 2.12, right). Each straw readout will be readout on both sides by means of pre-amplifiers and TDCs for timing and will include one ADC for dE/dx capability. The position along the straws is obtained by charge deposition and time. The required tracker resolution on position measurements is about 100 μm.

Tracker momentum resolution is important to determine the level of several critical backgrounds. The required momentum resolution is $\sigma < 180$ keV: current simulations indicate that the net resolution of the tracker is smaller than the estimated deterioration due to the energy loss in the upstream material (Fig. 2.13).

2.2.4.2 The Calorimeter

High rates of hits in the tracker may cause pattern recognition errors that add tails to the resolution function. Accidental hits combined with lower energy particles might

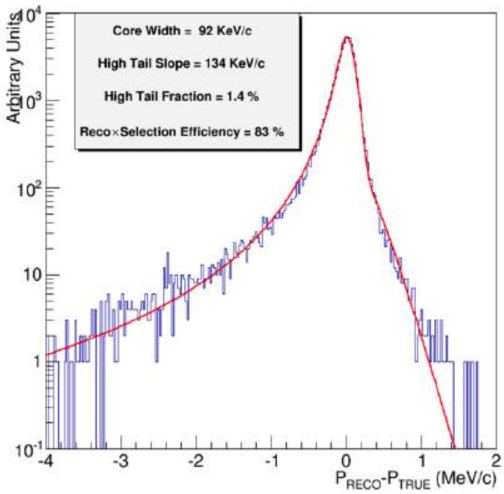

Figure 2.13: *Tracker momentum resolution with simulated CEs. Full background overlay and pattern recognition included. Fit to a split double Gaussian with standard track fit quality cuts. The core width satisfyes the 180 keV momentum resolution requirements [28].*

reconstruct to a trajectory consistent with a higher energy conversion electron. A calorimeter downstream to the tracker allows particle identification and rejection of such kind of background, combining the fitted helix trajectory extrapolated with the measured energy deposit, timing and position. In particular, energy and timing measurements from the Mu2e calorimeter provide information critical for efficient separation of electrons and muons in the detector (next chapter).

Besides the Particle Identification (PID), the calorimeter allows:

- track seeding;
- rejection of the background due to cosmic ray muons, not vetoed by the Cosmic Ray Veto (CRV) system, with energy and timing information;
- to perform a fast and stand alone high level trigger (HLT), based on energy measurements;
- reduction of the total volume and rate of the data storage.

The Mu2e electromagnetic calorimeter consists of 1820 BaF_2 crystals located downstream of the tracker and arranged in two disks (Fig. 2.14). The square crystals dimensions are (30.7×30.7) mm^2 across flats and are 200 mm long. Each crystal is

read out by two large-area solid-state photo-detectors, as required by the presence of 1 T axial magnetic field. Front-end electronics, HV, slow controls and digitizer electronics are mounted on the rear of each disk and must operate in high vacuum, high magnetic field and high radiation conditions.

As already experimented by the BaBar electromagnetic calorimeter, a circulating liquid radioactive source system provides absolute calibration, while a laser flasher system will be used for relative calibration and gain monitoring.

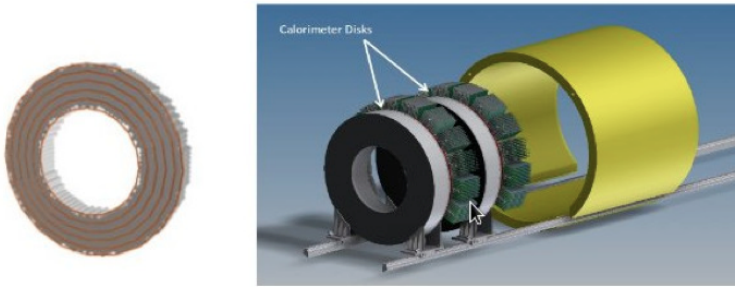

Figure 2.14: *The Mu2e electromagnetic calorimeter. 1820 BaF2 crystals are assembled in two annular rings of the same size. Lower energy electrons will pass through the hole, while the conversion electron candidates will hit the upstream disks faces.*

2.2.4.3 The Muon Beam Stop

The final component in the DS is the muon beam stop (MBS). This is where about 60% of the muons stop. The MBS is designed to absorb the energy of beam particles that reach the downstream end of the solenoid while minimizing the background to the detectors from the muon decays. Structurally, the MBS consists of several concentric cylindrical structures of stainless steel and high density polyethylene. The MBS is coaxial with the DS bore, and the green end plug is on the downstream end [TDR].

2.2.4.4 The Cosmic Ray Veto

Muons from cosmic rays are a known background source for the Mu2e experiment. They could produce 105 MeV particles mimicking a particle emanate from the stopping target or produce 105 MeV electrons and positrons through secondary and

b!

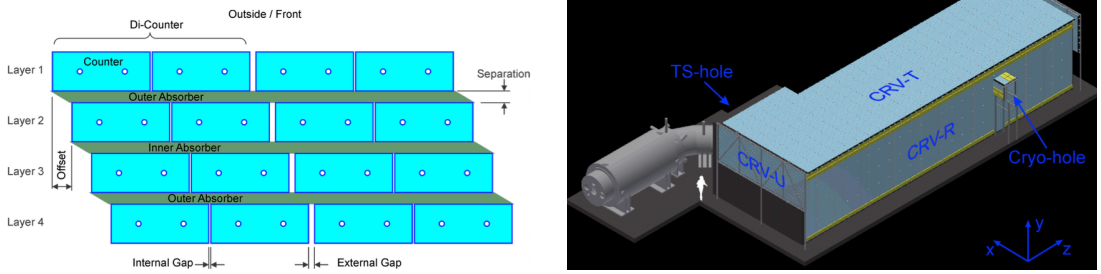

Figure 2.15: *Left:The CRV system is an active veto made by a system of four layers of long scintillator strips, with an aluminum layer between them. Right: the cosmic ray veto covering the Detector Solenoid and half of the Transport Solenoid.*

delta-ray production in the material within the solenoids, as well as from muon decay-in-flight. Moreover, muons themselves could be misidentified as electrons. Such kind of background events occur at a rate of about one per day and must be suppressed in order to achieve the required sensitivity.

The CRV system is an active veto made by a system of four layers of long scintillator strips (Fig. 2.15. left), with an aluminum layer between them, which covers all the DS and the last part of the TS too (Figure 2.15, right). The strips are 2 cm thick, providing ample light yield to allow a low enough light threshold to be set to suppress most of the backgrounds. Aluminum absorbers between the layers are designed to suppress punch through from electrons. The scintillation light is captured by embedded wavelength-shifting fibers, whose light is detected by silicon photomultipliers, SiPMs, at each strip end.

Chapter 3

The Calorimeter

The Mu2e calorimeter has to provide information about energy, timing and position to validate the charged particle reconstructed by the tracker, reject fakes induced by cosmic rays and antiprotons and perform a particle identification to distinguish muons from electrons. It should be also fast enough to be used in the software trigger. The design of the calorimeter is driven by the need to reject backgrounds to reach a S.E.S. for muon conversion process of the order of 2.5×10^{-17} and also to maximize the acceptance for ~ 105 MeV conversion electrons tracks.

3.1 Requirements

The previously stated tasks lead to the following requirements [28]:

- an energy resolution around 5% (5 MeV, at 100 MeV) is desirable to confirm the electron momentum measurement from the tracker, which is much more precise (100 keV/c @ 100 MeV/c);
- a timing resolution better than ~ 0.5 ns is required to ensure that energy depositions in the calorimeter are in time with events reconstructed by the tracker;
- a position resolution ($\sigma_{r,z}$) better than 1 cm is needed to allow comparison of

the position of the energy deposit to the extrapolated trajectory of a reconstructed track;

- the calorimeter should provide additional information that can be combined with information from the tracker to help the particle identification to distinguish muons from electrons;
- the calorimeter must provide a trigger, either in hardware, software, or firmware that can be used to identify events with significant energy deposits;
- the energy deposited in the calorimeter provides a "seed" for tracker pattern recognition, to improve track finding efficiency at high occupancy;
- the calorimeter must operate in the unique high-rate Mu2e environment and must maintain its functionality for radiation exposures up to $\sim$ 15 krad/year in the hottest region and for a neutron flux equivalent to 10^{11} MeV/cm^2;
- temperature and gain stability is necessary to ensure that the readout system does not introduce variation of more than $\pm$ 0.5%. Larger fluctuations could deteriorate the energy resolution.

Moreover, the Mu2e calorimeter must be fast enough to handle the experimental high rate and it must operate within the 1 T magnetic field. This implies the use of solid-state photodetectors and of electronics (HV and FEE) immune to the presence of the magnetic field. In order to reduce multiple scattering of CEs on air molecules and prevent discharge from detector high voltage, the calorimeter has to operate in high vacuum regime.

3.1.1 Energy and time resolution

Even if the tracker momentum resolution is sufficient to distinguish a signal from the background, a combination of hits from lower energy particles could result in an erroneously reconstructed CE signal: even a coarse confirmation of the particle's energy will then be fundamental to reject this kind of background from spurious combinations of hits from lower energy particles. The signals from the tracker and from the calorimeter are correlated in time. The time of the calorimeter signal

should be comparable to the time of impact of the extrapolated tracks from the tracker. The difference between these two times should be less than 0.5 ns and this value drives the timing resolution requirement of the calorimeter [28].

The calorimeter timing information can be used by the cluster reconstruction algorithm in several ways: for the cluster reconstruction itself, a good time resolution helps in the connection and rejection of cells to the cluster and in the cluster merging. This, however, depends strongly on the geometry and granularity choice.

Timing information can also be used to improve the pattern recognition in the tracker and add discriminating power to the particle identification of μ with respect to the electrons (PID). Figure 3.5 shows how the calorimeter allows a simplification of the pattern recognition: the speed and efficiency of tracker reconstruction is improved by selecting tracker hits compatible with the time ($|\Delta t| < 0.5$ ns) and azimuthal angle of calorimeter clusters.

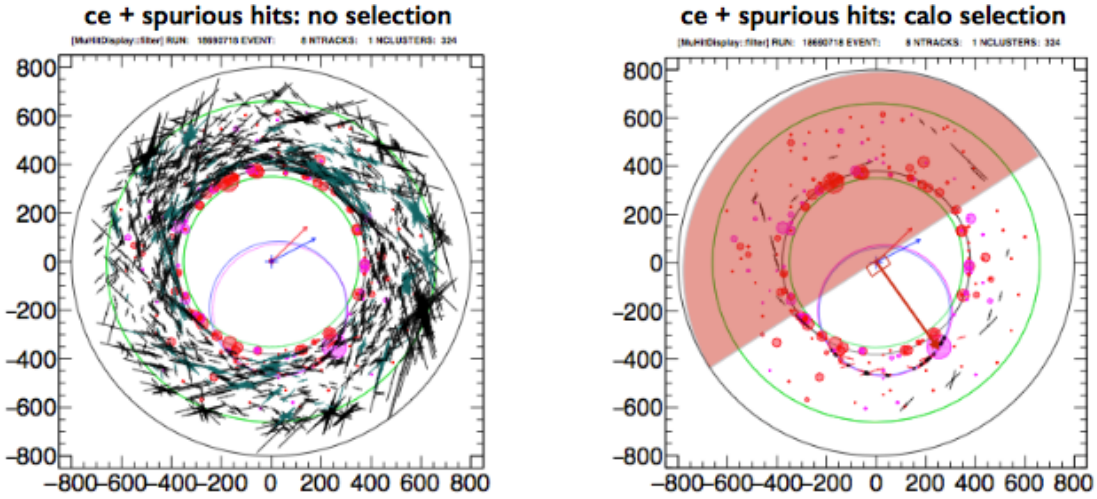

Figure 3.1: *Distribution of the hits in the tracker before (left) and after (right) the application of a timing window based on timing information in the calorimeter. The situation for the pattern recognition is dramatically improved: fitting a helix to the selected tracker hits and calorimeter cluster increases the tracking efficiency by 9%*

3.1.2 Particle identification and muon rejection

The main goal of the particle identification (PID) at Mu2e is to separate potential signal, CEs, from muons which could be associated with the beam or produced in

the atmospheric showers.

Cosmic rays generate two distinct categories of background events: muons trapped in the magnetic field of the DS and electrons produced in a cosmic muon interaction with detector material.

Studies on cosmic ray induced background, assuming a CRV inefficiency of about 10^{-4}, show that after 3 years of data taking one could expect about 3 events in which negative cosmic muons with $103.5 < p < 105$ MeV/c enter the detector, not detected by the CRV counters and surviving all analysis cuts [31]. The event display of a such kind of event is shown in Figure 3.2.

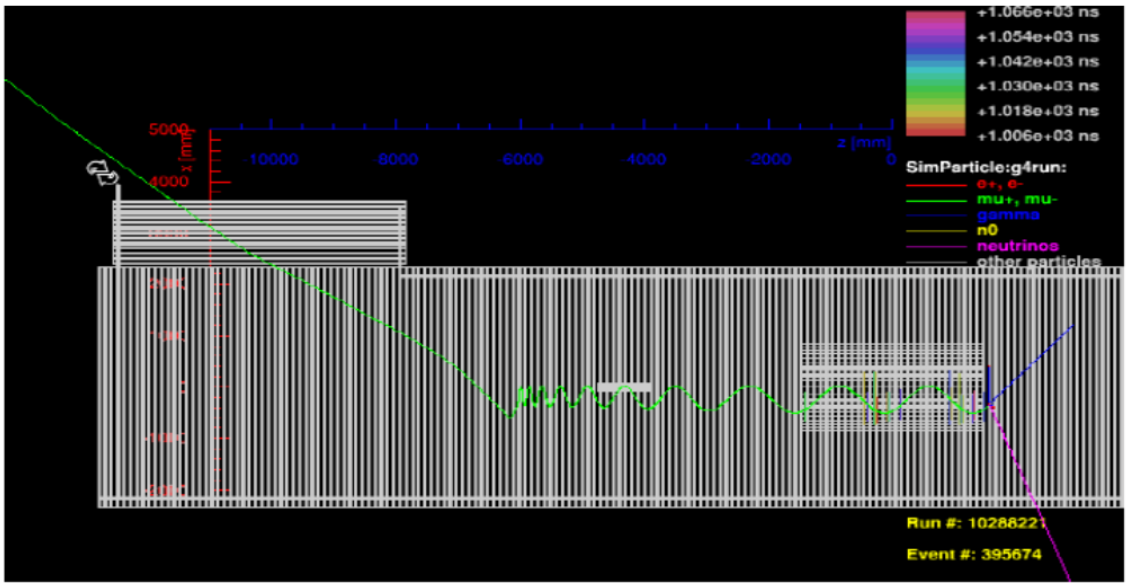

Figure 3.2: *Event display of a negative muon from cosmic rays mimicking a CE signal.*

Thus, to keep the total background from cosmic rays at a level below 0.01 events, a muon rejection factor of 200 is required. Timing and dE/dx information from the Mu2e tracker provide some PID capabilities [32]. However, to reach a muon rejection factor of 200, the efficiency of the electron identification based on the tracker-only information goes below 50%. The energy and timing measurements from the Mu2e calorimeter provide information for an efficient separation of electrons from muons. In Figure 3.5, the distributions of the time difference between the track and cluster times and the E/p are reported both for muons and electrons, showing a clear separation between the two particles. A PID likelihood is built combining these two

variables.

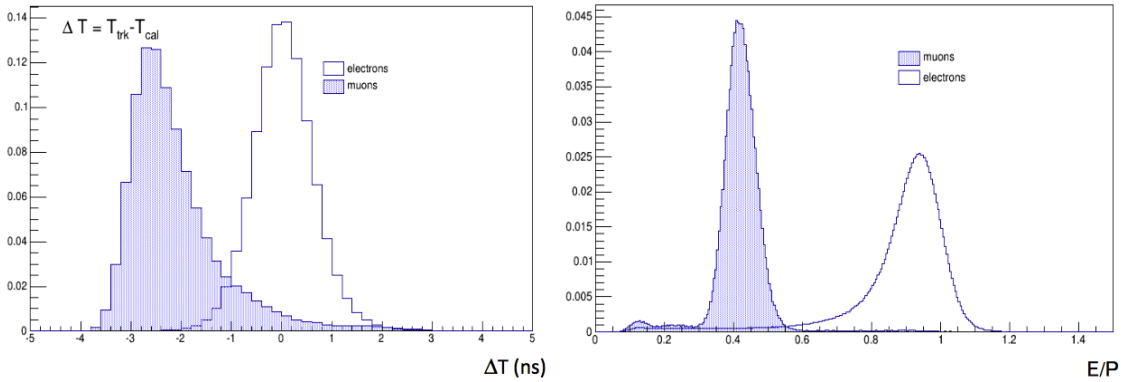

Figure 3.3: *Distributions of time difference, Δt, between the track and the cluster (left) and E/P (right) for 105 MeV/c electrons and muons [28].*

The calorimeter acceptance has been optimized to reveal 99.4±0.1 % of the CEs produced from the stopping target, with tracks passing "Set C" quality cuts [34] and producing a calorimeter cluster with $E > 10$ MeV from the conversion electron. Therefore a reconstructed CE candidate event is required to have a calorimeter cluster, pointed to by a track.

In Figure 3.4 (left) the dependence of the electron identification efficiency from the timing resolution for different values of the calorimeter energy resolution is reported, with a muon rejection factor set at 200. It is also possible to see that in the expected operational range, $\sigma_E/E < 0.1$ and $\sigma_T < 0.5$ ns, the PID is robust as a function of the time resolution, for different values of the energy resolution, with the electron identification efficiency variations below 2% in this region of parameter space.

3.1.3 The calorimeter trigger

The calorimeter system can also generate a fast, efficient trigger for the experiment. This trigger will take the form of a HLT filter that will be used after streaming the events to the online computing farm, but before storing data on disk.

The most important aspect of this filter is that it is fully independent from the tracker. The latter statement is particularly important for smooth start-up of the

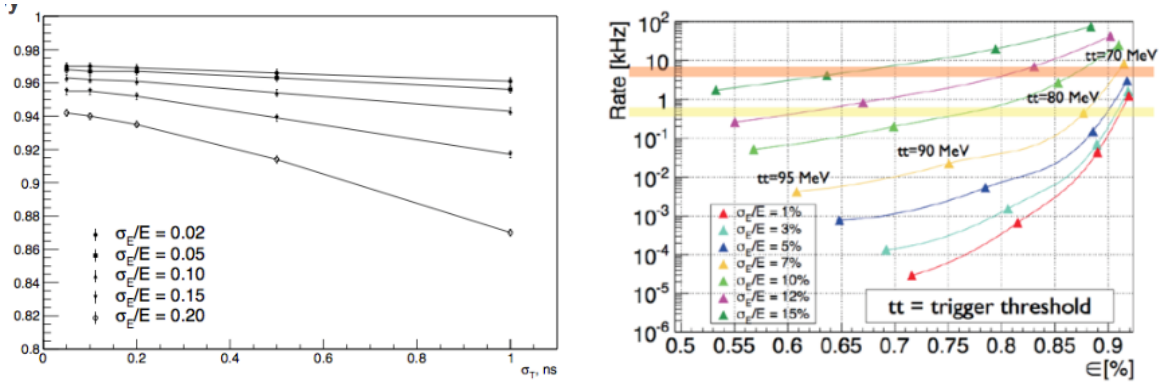

Figure 3.4: *Left: PID efficiency for CEs for muon rejection factor of 200 and different assumptions about the calorimeter energy and timing resolution. Right: DIO rejection versus calorimeter trigger efficiency for different calorimeter energy resolution. The two horizontal bands correspond to storage on disk at 600 Hz or 4 kHz.*

experiment when running conditions will not be perfectly known. Indeed, while the overlapping hits in the tracker make pattern recognition difficult, a calorimeter-based filter that depends only on the applied energy threshold will see any additional hits only as increased energy. This will translate to higher throughput for the background without substantially affecting the trigger efficiency. The offline application of the Δt cut can also be used to speed up the tracker reconstruction.

Studies about DIOs rejection and signal efficiency for a simple calorimeter cluster-based trigger demonstrate that the requirement to bring down the data storage rate to 2 kHz while keeping a filter efficiency of $> 90\%$ implies building a calorimeter with an energy resolution better than 7%, as shown in Figure 3.4 (right), where the DIO survival rate as a function of the trigger efficiency is shown for different values of energy resolution [33].

In summary, an energy resolution of $\sim 5\%$ is a reasonable goal for the calorimeter.

The purpose of the calorimeter's position measurement, instead, is to confirm that the reconstructed track from the upstream tracker points to the location directly measured by the calorimeter. The position resolution should ideally, therefore, be comparable to or better than the extrapolated position error from the upstream track, which is around 1x1 cm^2 [28].

3.1.4 Environment

The Mu2e calorimeter must operate and survive in the unique Mu2e environment: high radioactive dose, 1 T constant magnetic field and 10^{-4} Torr internal pressure.

3.1.4.1 Radiation hardness

Scintillating crystals, of the kind of the Mu2e calorimeter baseline design, suffer from radiation damage. Both ionizing dose and neutral particles can produce three possible damage effects [35]:

- damage to the scintillation mechanism, which would reduce scintillation light yield and may also change the light longitudinal response uniformity if the irradiation profile is not uniform along the crystal;
- radiation-induced absorption, which reduces light attenuation length and thus light output;
- radiation-induced phosphorescence, which causes an increased dark current in photo-detectors and thus an increased readout noise.

No scintillation-mechanism damage was observed in crystals listed in Table 3.1. The main damage in these crystals is radiation-induced absorption, or color-center formation. Radiation-induced color centers may recover at the application of high temperature through color-center annihilation. If so, a precision light monitoring system is mandatory to follow variations of crystal transparency in situ. However, the radiation-induced absorption, in all of the crystals listed in Table 3.1, does not recover at room temperature. Radiation-induced damage in these crystals was measured for some crystal samples (Ch.4). Both transmittance and light output were also measured. Radiation damage due to γ-ray dose causes a loss of transmittance and light output, while neutron irradiation appears less problematic.

Figure 3.5 shows the expected deposited dose per year in each crystal of both the two calorimeter disks, using a full Mu2e simulation, including contribution from the beam flash, DIOs, neutron, protons and photons. The average dose is around

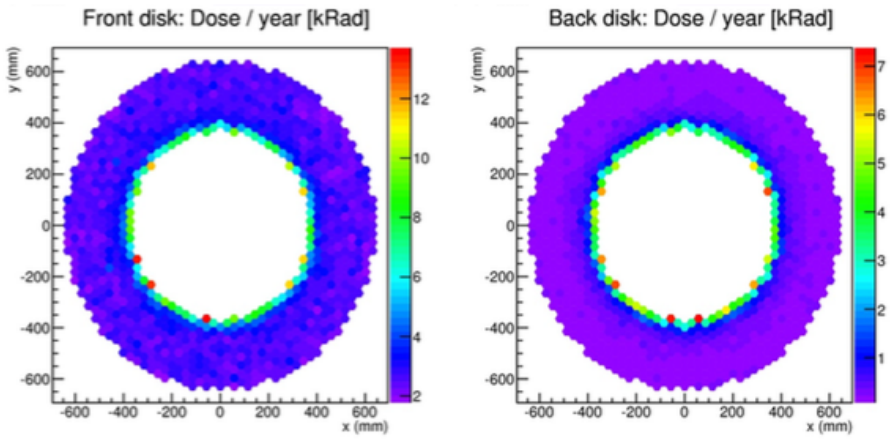

Figure 3.5: *Expected dose in each crystal of the front (left) and back (right) disks. The dose is given in krad/year.*

3 krad/year in the front disk and 0.5 krad/year in the back one, but it increase up to 15 krad/year for the innermost crystals of the front disk [28].

The neutron flux expected in three years running is of 10^{11} n/cm^2. Neutrons incident on both APDs and SiPMs could increase the dark current and deteriorate the calorimeter performance.

3.1.4.2 Magnetic field

The presence of a 1 T almost uniform magnetic field requires the use of solid-state photodetectors for crystals readout. Also the electronics (HV and FEE) must be immune to the presence of the magnetic field.

3.1.4.3 Vacuum

To reduce multiple scattering of CEs on air molecules and prevent discharge from detector high voltage, the entire muon beamline, DS included, must have an internal pressure of 10^{-4} Torr ($\sim 10^{-7}$ atm) at most.

The consequent extreme rarefaction of the gas inside the detector makes essential to dissipate the heat by conduction: a cooling system, shared with the Tracker, will remove heat from ADCs and FPGAs through R-410A refrigerant.

3.2 Design

In the 100 MeV energy regime, a total absorption calorimeter employing a homogeneous continuous medium is required to meet the resolution requirements. Different types of crystals have been considered for the Mu2e calorimeter: lutetium-yttrium oxyorthosilicate (LYSO), lead tungstate ($PbWO_4$), Barium Fluoride (BaF_2) and pure Cesium Iodide (CsI). $PbWO_4$ has been excluded for its low LY.

In Table 3.1 a comparison of the properties of all these crystals is reported.

Property	BaF_2	LYSO	CsI	$PbWO_4$
Density [g/cm^3]	4.89	7.28	4.51	8.28
Radiation length X_0 [cm]	2.03	1.14	1.86	0.9
Molière radius [cm]	3.10	2.07	3.57	2.0
Interaction length [cm]	30.7	20.9	39.3	20.7
dE/dx [MeV/cm]	6.5	10.0	5.56	13.0
Refractive Index at λ_{max}	1.50	1.82	1.95	2.20
Peak luminescence [nm]	220, 300	402	310	420
Decay time τ [ns]	0.9, 650	40	26	30,10
Light yield (compared to NaI(Tl)) [%]	4.1, 36	85	3.6	0.3,0.1
Hygroscopy	None	None	Slight	None

Table 3.1: *Comparison of crystal properties for LYSO, BaF_2, pure CsI and $PbWO_4$.*

In Figure 3.6 a comparison of the radiation hardness up to a 1 MRad dose for LYSO, BaF_2 and pure CsI scintillator crystals is shown. The radiation damage in all three crystals does not recover, but, while radiation damage in LYSO and BaF2 can be thermally annealed, this is ineffective for pure CsI. The losses in emission weighted longitudinal transmittance, EWLT, (top left), light output, LO, (bottom left) and radiation-induced absorption coefficient, RIAC, (right) at the peak of crystals radioluminescence are also reported. LYSO crystals are clearly the best in both light output and radiation hardness. The other two less expensive materials are, however, significantly more susceptible to radiation damage than LYSO. Because of low defect

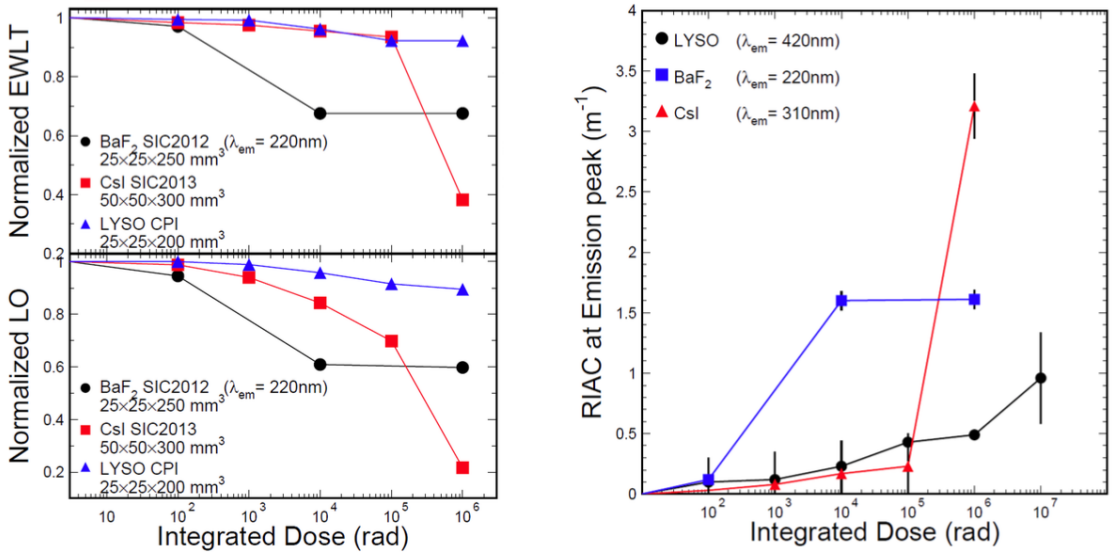

Figure 3.6: *Normalized EWLT and light output (left) and the RIAC at the emission peak (right) as a function of the integrated dose up to 1 Mrad for LYSO, BaF2 and undoped CsI crystals [28].*

density, radiation damage in BaF_2 saturates after about 10 krad. Radiation damage in CsI is small at low doses, but shows no saturation at high doses, indicating continuous degradation under irradiation. Measurements indicate that CsI is much more radiation hard than doped CsI. For doses up to 10 krad, no severe radiation damage has been observed.

As shown in Figure 3.6, in the hottest region of the calorimeter (dose up to $\sim 10^4$) BaF_2 will lose around 50% of its light after 10^4 rad and CsI around 20-25 %.

3.2.1 Baseline design

At the start of the Mu2e project, the crystal considered for the calorimeter was $PbWO_4$, at the time of the Mu2e CDR, it was replaced by LYSO crystals. The latter crystal option represents an excellent match to the problem of the experiment: it has a very high light output, a small Molière radius, a fast scintillation decay time, excellent radiation hardness and a scintillation spectrum that is well-matched to readout by large-area Avalanche Photodiodes (APD). Due to the increased price of LYSO crystals, this choice is unaffordable and for CD-2 we have therefore opted for BaF_2 crystals for the calorimeter baseline.

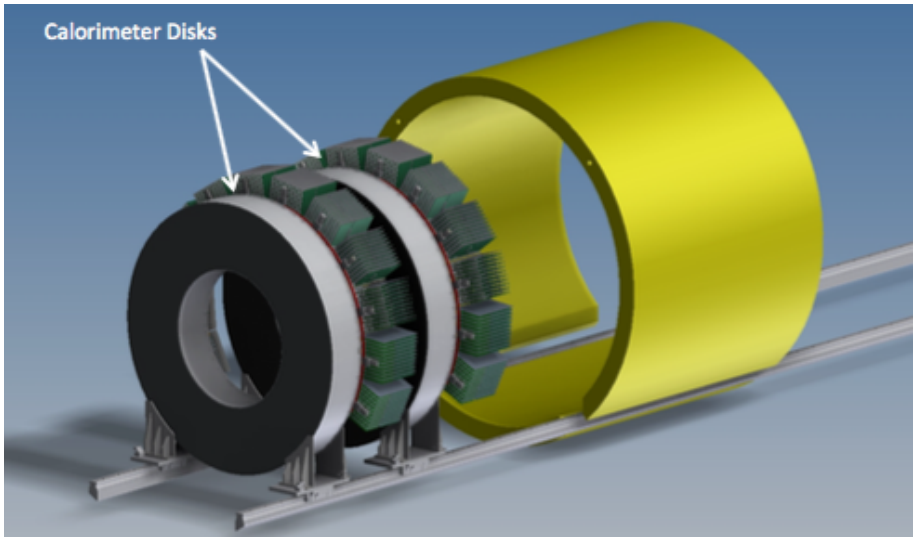

Figure 3.7: *The Mu2e calorimeter consists of an array of 1650 scintillating crystals arranged in two annular disks, with disks radii of 351 mm (internal) and 660 mm (external) and depth of 10 times X_0 ($\sim$ 200 mm).*

The baseline calorimeter consists of 1820 BaF_2 $3 \times 3 \times 20$ cm^3 square crystals, arranged in two disks (Fig. 3.7), separated by approximately a half-wavelength of the typical CE helical trajectory (70 cm). In this configuration, low-energy particles will pass through the hole and the distance maximizes the acceptance, while maintaining excellent signal efficiency (Fig. 3.8, right).

The dimensions of the crystals and of the disks were optimized to maximize calorimeter efficiency. The chosen crystals length is a trade-off between leakage effects, budget constraints, needed space between disks and also number of spurious hits due to helicoidal electron trajectory. Even if a longer crystal reduces the leakage, it also increases the probability of an electron passing through the hole and hitting the crystal on the side. The electromagnetic showers originating from these electrons will not be completely contained in the calorimeter, causing badly reconstructed clusters. These events must then be avoided as much as possible. The length of the crystals (200 mm) corresponds to 10 times the radiation length (X_0), however considering an average angle of incidence of 50°, conversion electrons pass trough $\sim$ 300 mm of the calorimeter, corresponding to 15 times X_0. The disk inner and outer radii will be 351 m and 660 mm respectively (Fig. 3.8, left).

Each crystal will also be wrapped with 4 layers of Teflon of 20 μm each, to avoid

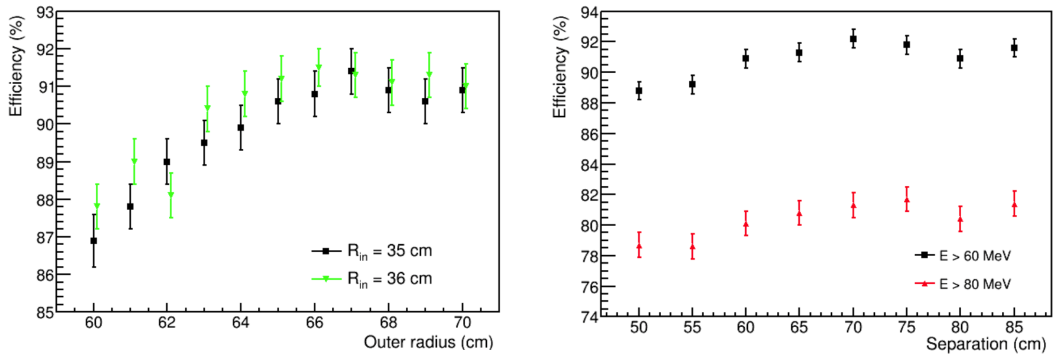

Figure 3.8: *Calorimeter efficiency for detection of good signal tracks initially found in the tracker as a function of the disk outer radius for different values of inner radius (left) and as a function of the distance between the two disks with two hypothesis on the energy threshold (right) [28].*

light leakage, and read out by two large-area APDs.

Front-end electronics is mounted on the rear of each disk, while voltage distribution, slow control and digitizer electronics are mounted behind each disk in stand alone crates, as shown in Figure 3.9.

A laser flasher system provides light to each crystal for relative calibration and monitoring purposes. A pipes system, with a radioactive liquid source circulating inside, provides absolute calibration and energy scale channel by channel.

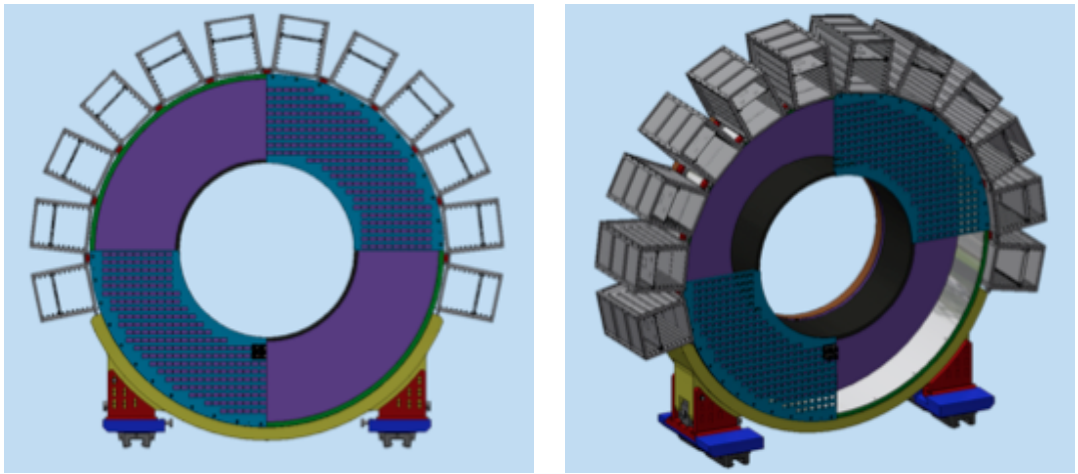

Figure 3.9: *Schematic model of the calorimeter support structure, included back plate for APD+FEE housing and the digitizer board crates.*

3.2.1.1 BaF_2 crystals

BaF_2 has a smaller light yield than LYSO, but much larger than $PbWO_4$. BaF_2 does not suffer from rate-dependent light output, but presents a larger value for the Molière radius and for the radiation length than LYSO. These characteristics are disadvantages, causing a larger shower extension and, consequently, a larger calorimeter dimension is required.

Figure 3.10 shows the emission spectrum of BaF_2. The main disadvantage of this crystal is the presence of two decay components: one very fast (BaF_2 is the only crystal with an emission decay-time, τ, smaller than 1 ns) with wavelength in the deep ultraviolet range (at $\sim$ 220 nm) and one much slower (650 ns) at 300 nm.

The short wavelength of these fast and slow scintillation components presents a difficult readout problem. Photomultiplier tubes (PMT) with quartz windows and solar-blind photocathodes can be well coupled to the BaF_2 spectrum, but the presence of a 1 T magnetic field precludes the use of such high-gain, low-noise photosensors. For the Mu2e experiment our main thrust is to use solid-state photosensors, either solar blind APDs or SiPMs, with UV extended response as readout. This will be explained in detail in next section.

A backup option is provided by pure CsI coupled with standard MPPC (Hamamatsu SiPM). However, its lower radiation hardness poses some project risks, espe-

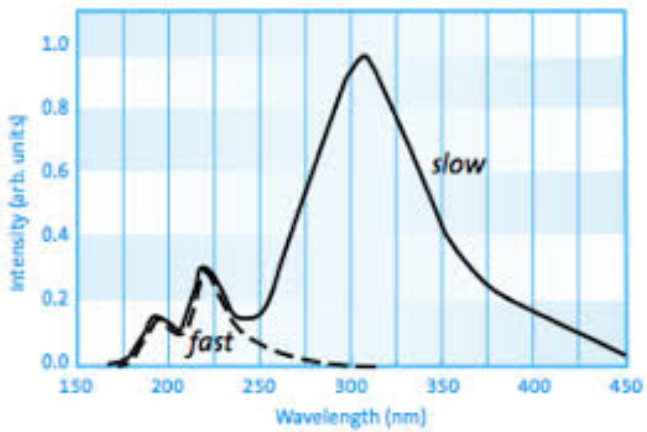

Figure 3.10: *Emission spectrum of BaF_2. The fast component ($\tau \sim$ 900 ps) peaks at 220 nm and the slow component ($\tau \sim$ 650 ns) peaks around 330 nm.*

cially for an eventual Run-II, at higher rates.

3.2.1.2 Avalanche Photodiode, APD

As alternative to the high-gain, low-noise PMTs, the photosensor candidate for BaF_2 readout is the APD. This is a semiconductor device made of a simple p-n junction, working in inverse polarization mode, at a voltage just below the breakdown level (Fig. 3.11). It consists of a thin layer of silicon in which the light is absorbed and free charge carriers (electrons and holes) are created and amplified. Electron and holes are collected at the anode and cathode of the diode, respectively. The primary electrons, produced by the incident radiation, are made to attain high velocities under the influence of an externally applied high electric field. If the energy attained by an electron is large enough, it can free one or more secondary electrons, thereby creating an avalanche of charge pairs.

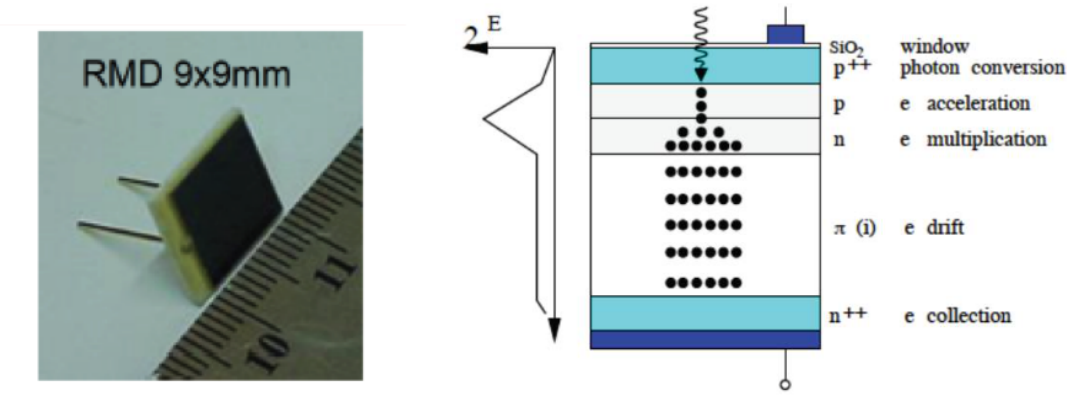

Figure 3.11: *Left: picture of a solar blind APD. Right: Schematic layout of the Avalanche Photodiode. An intrinsic (or lightly doped p-type) material π sandwiched between a heavy doped p-side and a heavy doped n-side. Another p-type region is also established between the intrinsic material and the heavily doped n side. A strong reverse bias between the two ends creates an electric field E.*

Theoretically, such a process is only possible if the incident electron gains energy at least equal to the band gap energy of the material. However, since an electron also loses energy through non-radiative scatterings, on average, the electron energy should be much higher than the band gap energy. For most semiconductors an

energy difference of a factor of 3 is normally required. The secondary electrons, being under the influence of the same electric field, produce tertiary charge pairs and so on. Once started, this process of charge multiplication grows and eventually causes avalanche multiplication of charge pairs (Fig. 3.11, right).

The ability to ionize of charge carriers is described by two ionization coefficients: α_e for the electrons and α_h for the holes, defined as the probability per unit length for a ionization impact. This probability is directly proportional to the electric field in the depletion region and inversely proportional to the temperature: the increase of internal vibrations in the crystal lattice can cause uncontrolled impacts before the electric field acceleration.

The gain, G, of the APD is quantified trough the formula:

$$G = \frac{1-\rho}{e^{-(1-\rho)\alpha_e w} - \rho} \ , \tag{3.1}$$

where $\rho = \alpha_h/\alpha_e$ and w is the width of the depletion region, it is possible to observe that with $\rho = 0$ the gain grows exponentially with the $\alpha_e w$ factor, while in the limit $\rho \to +\infty$, the gain is unitary. If electrons and holes have similar ionization coefficients ($\rho = 1$), they can both produce new electron-hole pairs along their tracks, thus increasing the gain. However, this process can slow down the avalanche envelope and increase the photodiode intrinsic noise: for this reason, APDs usually exploit only one type of charge carriers, generally electrons, because they maximize the device temporal response.

These photodetectors have low gain (< 1000) (Fig. 3.12, right), so that inorganic, high light response scintillators are mandatory.

Large area APD from Hamamatsu, APD S8664, showed to be well coupled to LYSO crystal: at the peak of the emission spectrum (402 nm), this photodetector has $\sim 65\%$ QE (Fig. 3.12, left). However, for the fast emission component of BaF_2 crystal (~ 220 nm) the QE of this device is much lower and, moreover, this APD is not capable to discriminate between the slow and the fast component.

A consortium formed by Caltech, JPL and RMD is then developing a modified version of a large-area APD with superlattice delta-doping (i.e. doping atoms confined to single atomic layers) and atomic layer deposition antireflection (AR) filter (solar blind). This device will be able to provide 60% QE at 220 nm and 0.1% QE

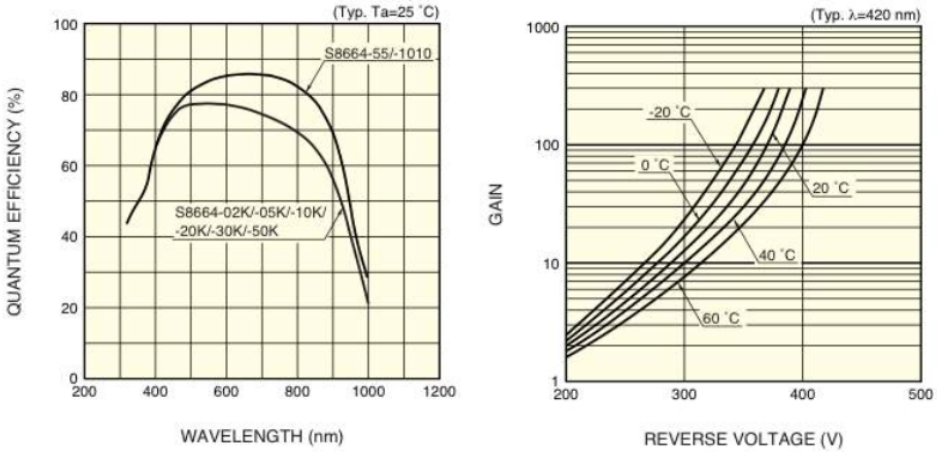

Figure 3.12: *Left: quantum efficiency vs wavelength for Hamamatsu APD S8664: at 402 nm (LYSO emission peak) its quantum efficiency is 65%. Right: gain vs reversed voltage for Hamamatsu APD S8664.*

at 300 nm.

This procedure has been already applied to a charged imaging device (CCD) [36]: the delta-doping and the anti reflective (AR) coating sensibly increases the QE at 300 nm (Fig. 3.13 left). For the RMDAPD, instead, the delta-doping should provide a high QE of $\sim$ 90% in the entire UV region. Thus, the deposition of 5 anti-reflection layers provides a transmission of nearly 70% at the fast component of BaF2 (220 nm), while the slow component (around 300 nm) is almost suppressed (Fig. 3.13, right). The overall QE near the spectrum should be around 60%.

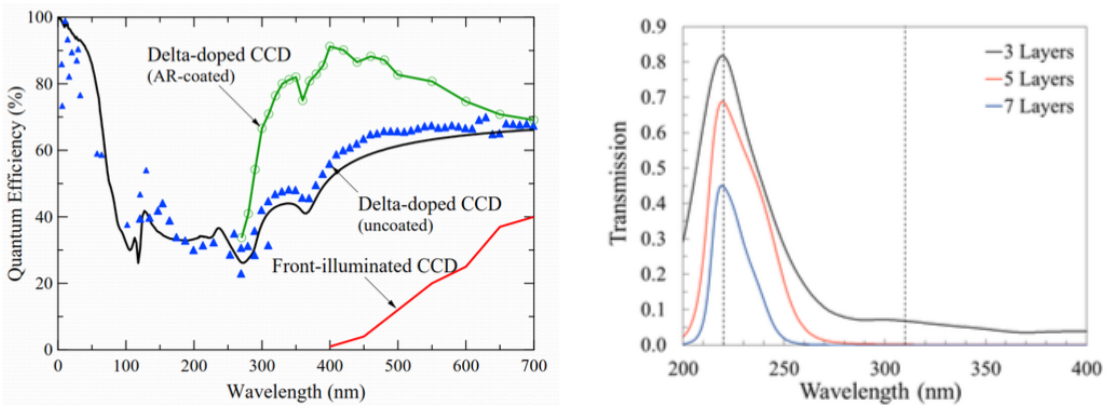

Figure 3.13: *Left: quantum efficiency vs wavelength for a delta-doped, AR-coated CCD (in green). Right: transmission vs wavelength with 3, 5 and 7 layers of AR coating.*

APD	HV (V)	Gain
Hamamatsu S8664	400	50
RMD	1650 - 1750	500

Table 3.2: *Specifications (typical value at around 23°) of the RMD and the Hamamatsu S8664 Avalanche Photodiode.*

To summarize, the advantages of APDs are a good quantum efficiency, absence of magnetic field sensitivity, moderate cost, compact size and a reasonable gain. However, electronic noise is a major problem due to the small signal amplitude. The main electrical characteristics of the two APD options are reported in Table 3.2. The Hamamatsu S8664 APDs require lower voltage with respect to RMD APD, but they have a much lower gain and they are not capable to suppress the BaF_2 slow component.

3.2.2 Backup solution

Since the solar blind APD are still on the development phase, we have pushed forward the study of a backup solution for the calorimeter. This consists of the combination of cheaper crystals, pure CsI, emitting at higher frequency (310 nm) coupled with large area UV extended Silicon Photomultipliers (SiPM).

3.2.2.1 Pure CsI crystals

Undoped Cesium Iodide (CsI, also called pure CsI) is a material with high γ-ray stopping power due to its relative high density and atomic number. It is used in physics experiments because of its combination of fast timing and relatively high density. Its scintillation is heavily quenched at room temperature, and cooling improves the light output.

This crystal is slightly hygroscopic, so contact with water and high humidity should be avoided and also during test a dry atmosphere is preferred. Undoped CsI has an emission maximum at 315 nm (Fig. 3.14, left), characterized by a relatively short decay time of $\sim$ 20 ns, it can therefore be used for fast timing applications

[37].

Next to this fast 315 nm component, a much slower component with a decay time of about 1 ms is present which represents less than 15% of the total light output. The intensity of this slow component depends very much on the purity of the crystal since contamination with certain trace elements tends to degrade the fast-to-total ratio. It will be considered negligible in our CsI samples.

Figure 3.14 (right) shows the CsI scintillation intensity as a function of the temperature. The light output, though, is heavily quenched at room temperature, and cooling to -77° would give ten times higher light output .

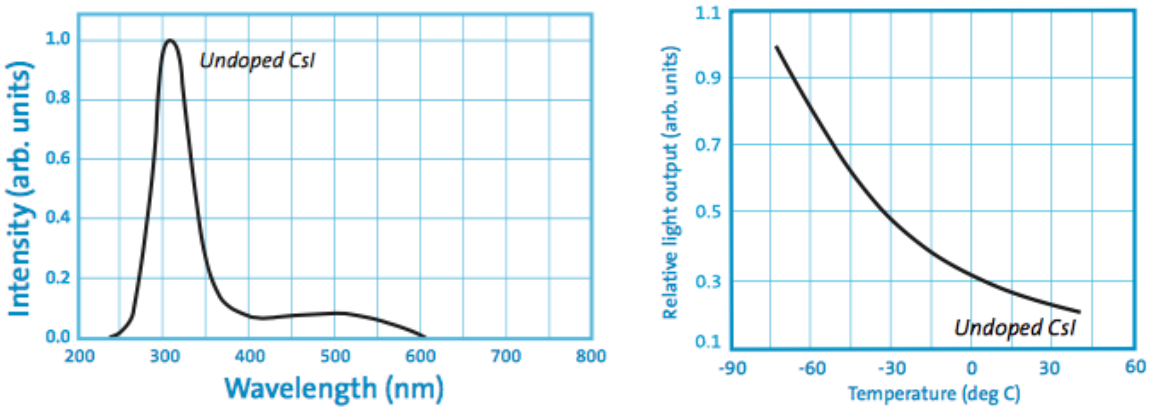

Figure 3.14: *Left: scintillation emission spectrum of pure CsI. Right: relative light output as a function of temperature .*

Because the emission wavelength is in the UV, the optical windows, surface conditions and optical coupling should be carefully selected in order to avoid light-loss. The scintillation emission properties are highly affected by the presence of trace impurities in quantities below ppm in the crystal and by growth process. Thus, a high quality process is mandatory to get a good, reliable performance.

To summarize, CsI is slightly hygroscopic but its emission is dominated by a single component with a τ of $\sim$ 20 ns @ 315 nm. Its light yield is expected to be around 100 photoelectrons per MeV (100 $N_{p.e.}$/MeV), without grease coupling and wrapping with reflector materials, with UV extended wavelength.

3.2.2.2 Silicon Photomultiplier, MPPC

The CsI crystals readout has to be made by high-gain solid-state photodetectors, such SiPMs.

SiPMs are photon-counting devices made by one planar matrix of several APD photodiodes pixel of the same shape, dimensions and constructions features operating in Geiger mode, with an inverse polarization above the breakdown and coupled to a quenching resistor. When a photon travels through silicon, it can transfer its energy to a bound state (valence) electron, thereby transporting it into the conduction band, creating an electron-hole pair. The Photon Detection Efficiency (PDE) in silicon depends on its energy (or wavelength), as shown in Figure 3.15. This illustrates that silicon is a good photo detector material in the spectral range between 350 nm and 800 nm.

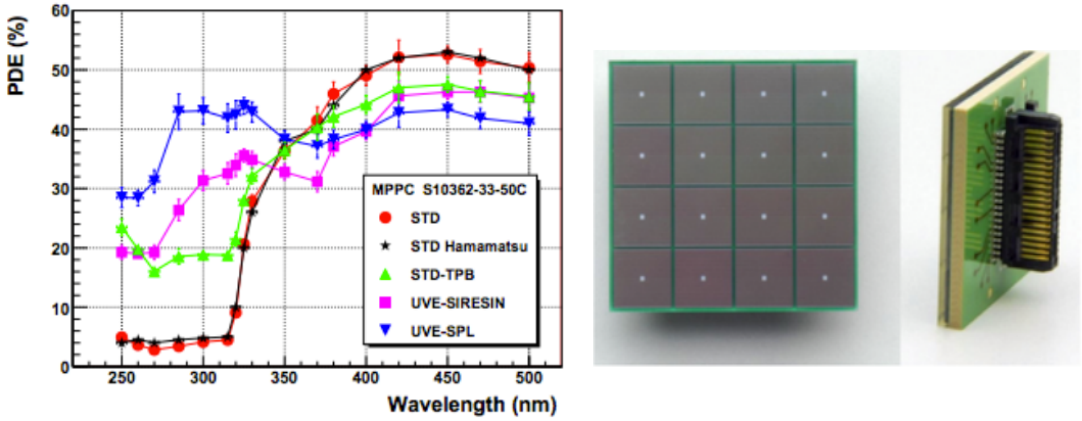

Figure 3.15: *Left: photodetection efficiency as a function of the wavelength for four SiPM prototypes. The typical PDE values of the standard MPPC S10362-33-50C from Hamamatsu are shown for comparison. These measurements were performed at 25° and include effects of cross-talk and after-pulses. Right: picture of an Hamamatsu SiPM.*

The PDE is the product of three factors:

- Quantum Efficiency, QE: this parameter is the ratio of the number of carriers collected by the photosensor to the number of photons of a given energy incident on the device. For silicon photodiodes, the QE peak is in the visible spectrum around 400 μm;

- Avalanche probability: the probability that an incident photon starts an avalanche;
- Fill factor: ratio between the pixel dimensions and the total SiPM dimension.

Each SiPM's APD pixel outputs a pulse signal when it detects one photon: the signal output from the device is the total sum of the outputs from all the pixels. It is then possible to cover a large area with several small photodetectors.

This devices operate on low voltage featuring high gain, high PDE, high-speed response, excellent time resolution and wide spectral response range.

The SiPM gain is directly related to its inverse polarization voltage:

$$G = \frac{Q}{e} = \frac{(V_{bias} - V_{bd}) \cdot C_{pixel}}{e}\,, \tag{3.2}$$

where V_{bias} is the voltage applied to the SiPM, V_{bd} the breakdown voltage and C_{Pixel} is the capacitance of a single pixel. The overall resistance of the photodetector and then its voltage breakdown V_{bd}, is a function of the temperature:

$$R = R_0(1 - \alpha T)\,, \quad \alpha = \beta / T_0^2\,, \tag{3.3}$$

where β is a parameter which depends on the device.

When a SiPM is hit by one photon, there is a dead time, also called recovery or quenching time, when the pixels have a lower value of deposited charge if hit again, due to the presence of the quenching circuit. Thus, if there is a large flux of incident photons on the SiPM area, the number of fired pixels will saturate with the relation:

$$N = N_{max}(1 - e^{-\frac{\mu}{N_{max}}})\,, \tag{3.4}$$

where N is the number of active pixels, N_{max} is the total number of SiPM pixels and $\mu = N_\gamma \cdot PDE$ is the number of incident photons rescaled with the PDE.

To summarize, the main aspects of MPPC development with reasonable QE at ~ 300 nm are:

- No need of solar blind filters;
- The gain is excellent;

- Double pulse separation is assured;
- The noise level is small.

So that, at the wavelength emission peak of pure CsI (315 nm) the standard Hamamatsu SiPM, called Multi-Pixel Photon Counters (MPPC) can be a good choice for the Mu2e calorimeter.

In particular, the performance of S13361 series MPPCs designed for the application in the photon-counting region are under study. The schematic structure of these devices is shown in Figure 3.16. These MPPCs allow precision measurements

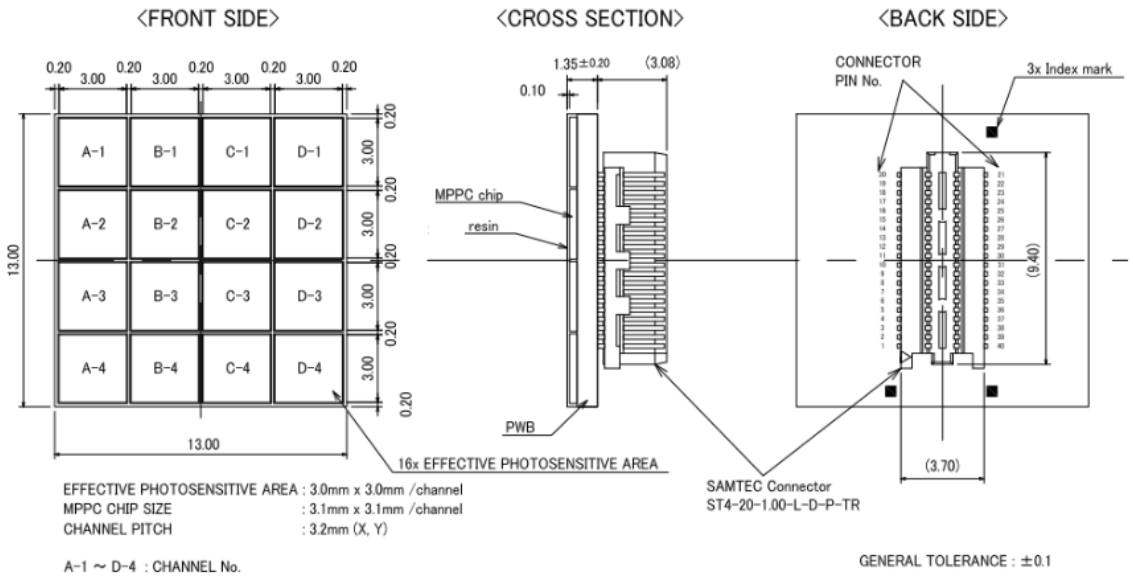

Figure 3.16: *Schematic structure (from left to right) of the front, cross and back side of the S13361-3050 Hamamatsu MPPC.*

and the strongest point is the drastical reduction of the cross talk (compared to previous products). The S13361 series use the TSV (Through Silicon Via) technology [40]. There is no wire bonding, so the package outline is very close to the MPPC array. The outer gap from active area edge to package edge is only 0.2 mm.

The main features of the TSV S13361 Hamamatsu MPPCs are:

- Low after pulse;
- Very compact package with small dead space;

- High sensitivity and reliability;
- Suitable from UV to near IR light, for precision photometry;
- Superior photon counting capability;
- Low voltage operation, $V_{op} \sim 53$ V;
- High gain, about 1.3×10^6.

3.2.2.3 MPPC's Front End Electronics

The Front-End Electronics (FEE) consists of two discrete and independent chips (Amp-HV) for each crystals that are directly connected to the back of the photosensor pins. These provide both the amplification stage and a local linear regulation for the photosensor bias voltage (Fig. 3.17, right).

The Amp-HV is a multi-layer double-sided discrete component board that carries out the two tasks of amplifying the signal and providing a locally regulated bias voltage. The two functions are each independently executed in a single chip layer, named the Amp and HV sides, respectively.

A dedicated ARM [41] controls groups of 16 Amp-HV chips, distributing LV and HV reference values, while setting and reading back the locally regulated voltages. Groups of 16 amplified signals are sent to a digitizer module where they are sampled and processed before being optically transferred to the DAQ system.

The required characteristics for the preamplifier are:

- high amplification with low noise;
- fast signal rise and fall times for good time resolution and pileup rejection;
- a low detection threshold at the MeV level;
- operation in a rate environment of 200 kHz/channel
- low power consumption.

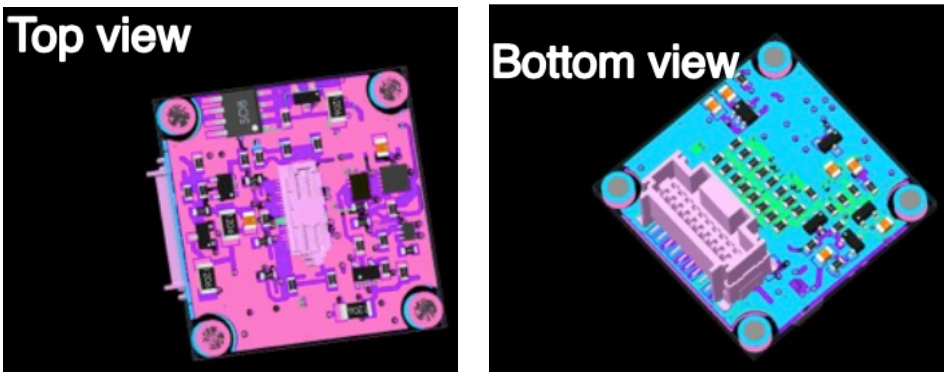

Figure 3.17: *Layout of the top (left) and bottom (right) side of the front end electronics used to readout MPPCs.*

Figure 3.17 shows the layout for the readout electronics developed by the Electrical Design Department of the Laboratori Nazionali di Frascati (LNF). The adder amplifier gain is ~ 5, the band width (BW) is 200 MHz and the rate capability up to 100 kHz. Instead, the HV regulator allows to have 10 mV steps, up to 90 V, with a stability better than 10 mV.

3.2.2.4 Digitizer

The Calorimeter Waveform Digitizer Prototype (Cal-WFD) is an electronic printed circuit board, which converts analog signals to digital, performs zero suppression, adds metadata, and combines individual channels into a single block of data. The Readout Controller serializes and translates data into the correct protocol, and sends the data to the DAQ, via a fiber optic transceiver. The schematic layout is shown in Figure 3.18.

The Cal-WFD has also to perform some digital signal processing operations, removing data below thresholds as well as providing the mean charge and time for each channel by means of running averages.

A prototype board has been designed and is currently being tested. The production version must operate in a difficult environment, due to the high radiation and high magnetic field, the knowledge gained from using this prototype will be essential to understand the needs of the production version.

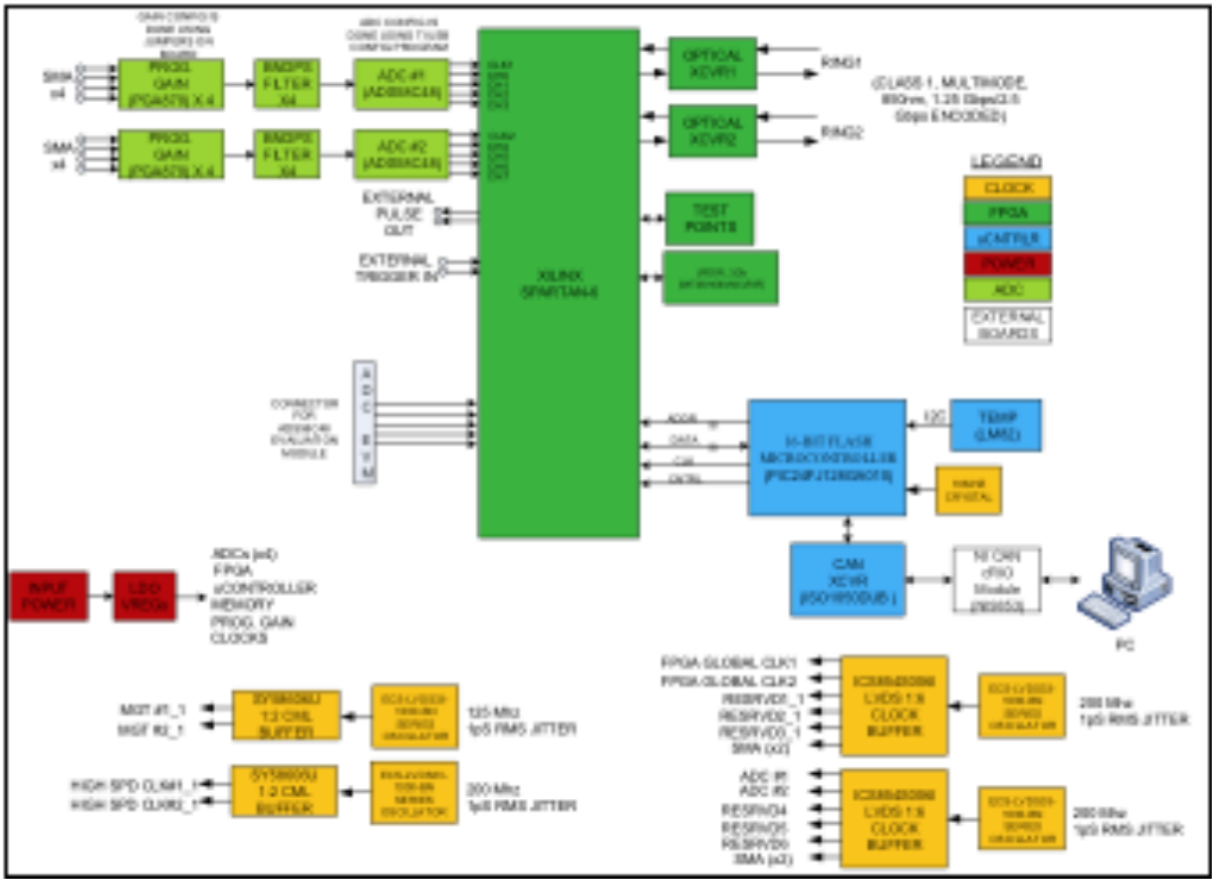

Figure 3.18: *Block Diagram of the Cal-WFD prototype board.*

Chapter 4

Experimental test on BaF_2 and CsI Crystals

As explained in the previous chapter, two crystals are being taken in consideration for the Mu2e calorimeter: the BaF_2 and the undoped CsI. In this chapter, we will summarize the sets of measurements carried out to check their properties and characterize their radiation hardness.

Most of the measurements have been performed at LNF using a dedicated station for crystals testing. The crystals have also been exposed to two different radiation sources: a large ionizing dose at ENEA-Casaccia γ irradiation facility (Calliope) and a large neutron flux at ENEA Frascati Neutron Generator (FNG). Test of their properties after irradiation have been carried out at the LNF station.

4.1 Light emission performance

The light yield and the longitudinal response uniformity of both BaF_2 and CsI have been measured by means of a ^{22}Na radioactive source.

To test the production quality, we have procured samples from different high quality producers in the world. In 2015 we have obtained a new sample of 13 pure CsI crystals: 2 from Opto Materials (Italy) and 7 from ISMA (Ukraine) companies, both with a crystal dimension of $(3 \times 3 \times 20)$ cm^3 and four additional longer crystals

$(2.9 \times 2.9 \times 23)$ cm^3 from ISMA. These CsI "2015" crystals are compared with two old samples produced by SICCAS (China) in 2014. Moreover, in order to compare with similar crystals from SICCAS already tested by our colleagues of Caltech, we have also procured 4 $(3 \times 3 \times 20)$ cm^3 BaF_2 crystals from INCROM (Russia).

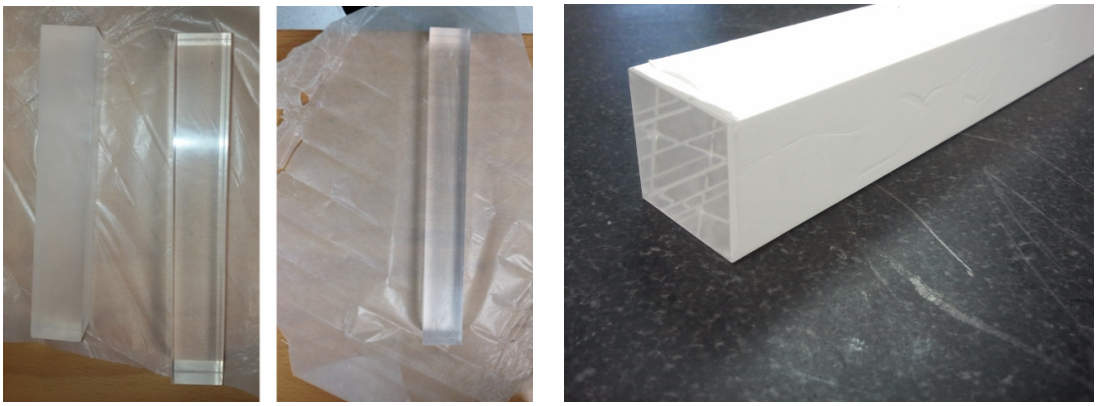

Figure 4.1: *From left to right: SICCAS (2014), Opto Materials and ISMA (2015) undoped CsI crystals and a BaF_2 from INCROM, wrapped with a Teflon foil.*

The picture of a crystal from each company is shown in Figure 4.1, together with the SICCAS undoped CsI crystal produced in 2014 (left). The new CsI productions show a much better optical transparency as already evinced by the optical inspection. This is confirmed by the results of the transmittance test, shown in Figure 4.2, where the longitudinal transmittance at a wavelength of 350 nm increases from $\sim 60\%$ to $\sim 80\%$ when comparing the 2014 SICCAS crystal to the new ones from ISMA and Opto Materials. The transmittance measurement has been performed with a large integration sphere in order to recover most of the light diffused due to the soft irregular surface of the crystal.

A new production of 10 SICCAS CsI crystals is also underway: the first 5 crystals received look much better than the 2014 production and with a performance more comparable to the crystals from the other companies.

One of the 2014 SICCAS crystal has been used for a dose test, while one crystal from each firm (both for CsI and BaF_2) has been used for a radiation hardness test with neutrons.

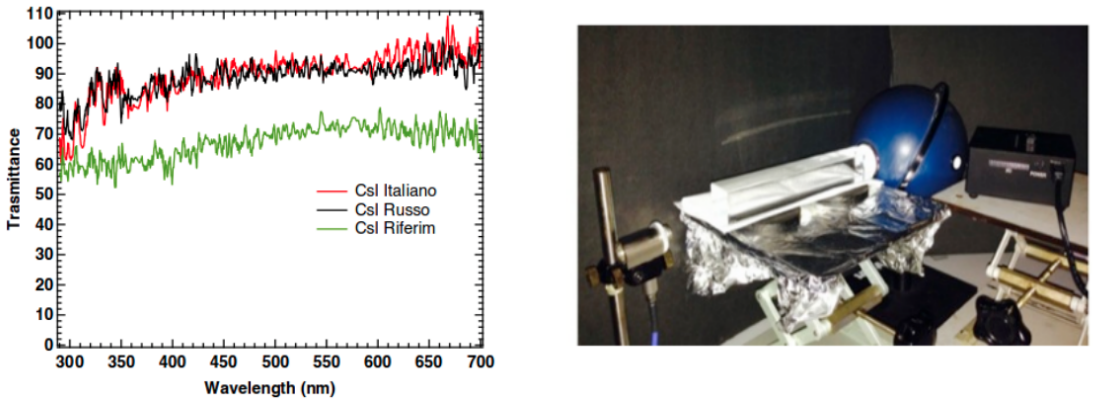

Figure 4.2: *Left: transmittance for SICCAS (green), Opto Materials (red) and ISMA (black) CsI crystals. Right: experimental setup used for the measurement.*

4.1.1 Experimental setup

To study the light yield (LY) and the longitudinal response uniformity (LRU) of each crystal, we have used a low intensity collimated ^{22}Na source which irradiates the crystal in a region of few mm^2. The ^{22}Na source produces 511 keV electron-positron annihilation photons and it is placed between the crystals and a small tagging system, constituted by a $(3 \times 3 \times 10)$ mm^3 LYSO crystal, readout by a (3×3) mm^2 MPPC.

One of the two back-to-back 511 keV photons produced by the source is tagged by this monitor, while the second photon is used to calibrate the crystal under test, which is readout by means of a 2" UV extended photomultiplier tube (PMT) from ET Enterprises. The efficiency curve of the PMT used is shown in Figure 4.3. It has a quantum efficiency of $\sim 30\%$ at 310 nm, which is the wavelength where the undoped CsI reaches the emission maximum. The whole system is inside a light tight black box.

The data acquisition system is composed by a trigger board, which starts the recording of the events applying a threshold of 20 mV on the tag discriminated signal, and a CAEN DT5751 digitizer at 10^9 samples per second (1 Gsps), which acquires both tag and test signals.

For each crystal, a longitudinal scan is done irradiating eight points, of 2 cm step, from the readout system. In the scan, the source and the tag are moved together

along the axis of the crystal under test with a manual movement. A detail of the setup is shown in Fig. 4.3. The crystal under test is placed inside a holder, while the hand-cart contains both the source and the tag crystal.

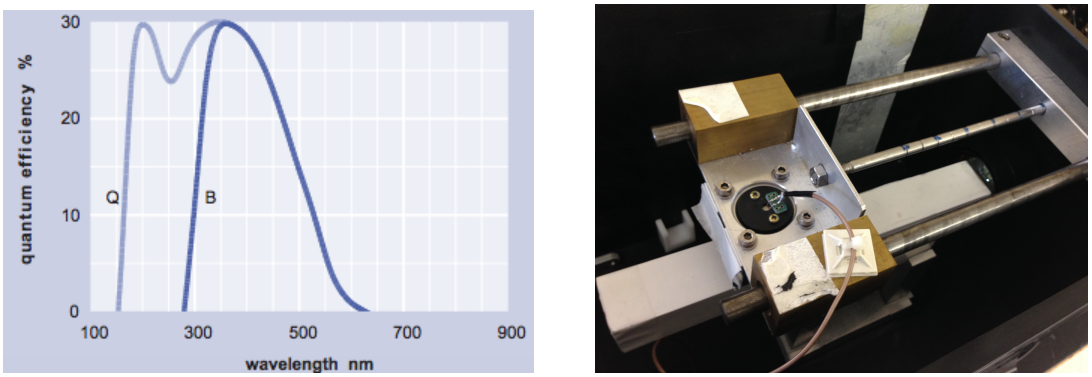

Figure 4.3: *Left: efficiency curve of the UV-extended photomultiplier tube used for the measurements. Right: detail of the setup used to test crystals. The coupling of a wrapped crystal with the PMT is visible. The cart bringing the source is also visible.*

A complete longitudinal scan takes about 10 minutes. We take $\sim$ 20000 events per point at an acquisition rate of $\sim$ 500 Hz. Each point is completed in about one minute with the adjustment of the next position taking few seconds. A program analyzes data for all points as soon as the scan is completed.

All crystals have been tested wrapped with a reflector material. The wrapping foils cover both the four longitudinal surfaces along the longitudinal axis and the side opposite to the readout system. The effect of applying optical grease to couple the PMT to the crystal has also been studied for some cases.

4.1.2 Measurement method

The digitizer has 1024 samples in the acquisition window, each sample corresponding to 1 ns. Examples of the pulse shapes, obtained for both tag and CsI crystals, are shown in Figure 4.4. The generic emission time distribution for a scintillator can be described as a fast component, generated by a two-step scintillation mechanism

(absorption, emission) and a slow component [38]:

$$E(t) = \frac{\frac{e^{-t/\tau_f} - e^{-t/\tau_r}}{\tau_f - \tau_r} + \frac{R}{\tau_s} e^{-t/\tau_s}}{1+R}, \tag{4.1}$$

where τ_f, τ_s, τ_r are the time constants of the fast and slow scintillation process and of the rising part, respectively. R is the ratio between the slow and the fast component. If we assume that the time resolution of our system can be described by a Gaussian, then the resulting distribution used to fit the waveforms is the convolution of $E(t)$ with a Gaussian, as follows:

$$V(t) = \frac{1}{1+R}\left[\frac{\tau_f f(t,\tau_f) - \tau_r f(t,\tau_r)}{\tau_f - \tau_r} + R f(t,\tau_s)\right], \tag{4.2}$$

where:

$$f(t,\tau) = \frac{1}{2\tau}\left[1 + \mathrm{erf}\left(\frac{1}{\sqrt{2}}\left(\frac{t}{\sigma} - \frac{\sigma}{\tau}\right)\right)\right] e^{-(t/\tau - \sigma^2/2\tau^2)} \tag{4.3}$$

erf is the error function, defined as:

$$erf(x) = \frac{2}{\sqrt{\pi}} \int_0^x e^{-t^2}\, dt \tag{4.4}$$

and σ is the Gaussian standard deviation.

The profiles of the waveforms have been fit with Eq. 4.2 to evaluate the decay time of each crystal. Fit results are reported in Figure 4.4; since CsI has a very small slow component, R parameter has been fixed to 0.1, while the resolution function of our system has been set to $\sigma = 1$ ns.

In our setup, signals produced in CsI crystals are typically within 300 ns from the trigger, with a 50 ns delay offset, so that the charge Q is obtained integrating in the range $(50 \div 300)$ ns. The baseline is evaluated using the interval region above 700 ns. Differently from CsI, the BaF_2 shows a very large slow component, so that the baseline is evaluated using the interval below 20 ns. The charge is then obtained integrating signals amplitude in the range $(20 \div 150)$ ns.

To reduce random coincidence, a cut on the time difference between the time of the tag system and the crystal signals, T_{mean}, is used. Signals are selected only if their peak time is around $\pm 3\,\sigma$ of the time distribution mean value (Fig. 4.5).

The peak of the 511 keV photons for the tag is extracted performing an asymmetric Gaussian fit around the maximum of the charge distribution, as shown in

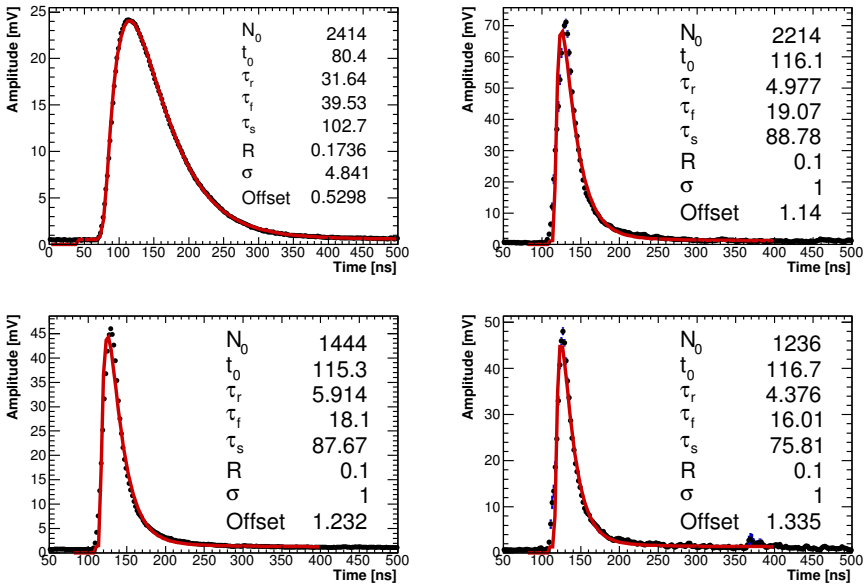

Figure 4.4: *Digitized waveform for few events of the tag (top left) and of one Tyvek wrapped crystal from each company acquired by the CAEN digitizer: Opto Materials 01 (top right), ISMA 05 short (bottom left) and ISMA 04 long (bottom right).*

Fig. 4.6. The peak position, extracted with a precision of few per mil, is then plotted as a function of the distance of the source from the PMT, obtaining a conversion factor of 96 pc/MeV, almost uniform along the crystal.

In Figure 4.7, the charge distributions for one of the crystals under test (Opto Materials 01), wrapped with Tyvek, are reported for the eight points of a single scan. The charge spectra are very clean and the peak due to the 511 keV photon is clearly visible. A Gaussian fit is applied to extract the mean values (μ_{Q1}): these values are then plotted as a function of the distance of the source from the PMT, obtaining a linear slope parametrized as $39\,\mathrm{pC} + 0.09\,\mathrm{pC/cm}$ (Fig. 4.7, bottom right).

4.1.3 CsI Crystals performance

All crystals have been tested with the ^{22}Na using just one orientation with respect to the readout system and with a 2 cm step longitudinal scan, starting at 2 cm from the PMT. For some of the crystals, the effect of the optical grease contact with the PMT has also been studied.

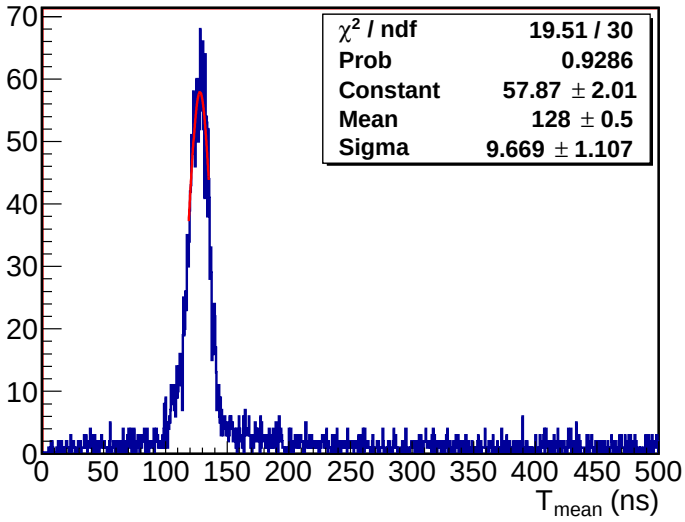

Figure 4.5: *Time distribution mean value, fitted with a gaussian function to evaluate the mean value and the σ of the distribution. Events are selected only if their peak time is around $\pm 3\,\sigma$ of the mean value.*

4.1.3.1 Wrapping materials

A reflector material wrapping is needed to improve the detection efficiency of scintillation photons. The Opto Materials pure CsI crystal number 02 has been tested with different wrapping materials: aluminum (Al), Tyvek, Teflon.

The first material, Al, is a good reflector in the UV wavelength range, showing a reflectance at 300 nm of about 90% with a tickness of about 10 μm.

The Tyvek is a brand of flashspun high-density polyethylene fibers, a synthetic material. It is very strong and difficult to tear but can easily be cut with scissors. Water vapor can pass through Tyvek, but liquid water cannot. Dedicated studies have shown that Tyvek is approximately 90% reflective on the range of interest. The tickness of Tyvek paper used is $\sim$ 100 μm.

The Polytetrafluoroethylene (PTFE), also called Teflon, is a synthetic fluoropolymer of tetrafluoroethylene. It diffuse light and shows a reflection up to $\sim$ 98% in the wavelength range $\sim$ (250 - 2500) nm. For crystals tests, 3 rounds of Teflon of

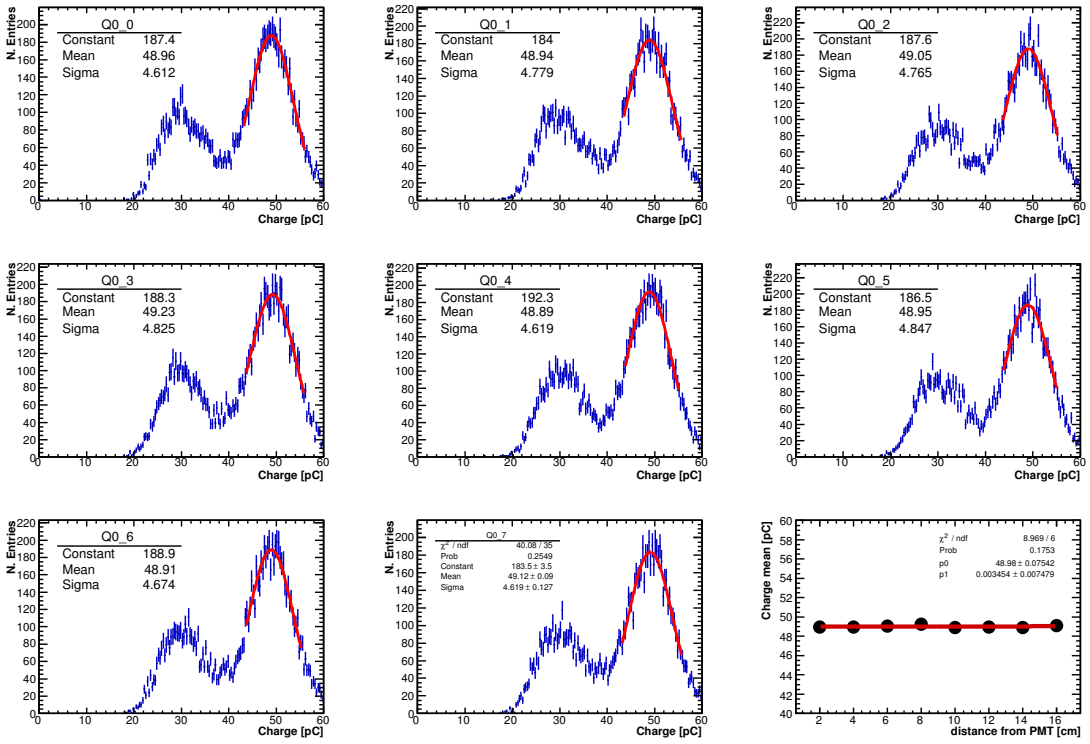

Figure 4.6: *Charge distributions of the tag crystal for different distances of the source from the PMT, fitted with an asymmetric Gaussian fit. The last plot shows the peak value as a function of the distance from the PMT.*

25 μm each has been used.

In Figure 4.8 (left) , the charge distributions obtained for each wrapping material, with the source placed in the central scan position, are shown. The distributions have been fit with a gaussian function to extract the peak position and evaluate the LY, defined as the number of photoelectrons produced per MeV, $N_{p.e.}/MeV$:

$$\frac{Np.e.}{MeV} = \frac{\mu_{Q1[pC]}}{G_{PMT} \cdot E_{\gamma}[MeV] \cdot q_{e^-}[pC]}, \tag{4.5}$$

where $q_{e^-} = 1.6 \times 10^{-19}$ pC is the charge of the electron, $E_{\gamma} = 511$ keV is the energy of the annihilation photon and $G_{PMT} = 3.8 \times 10^6$ is the PMT gain.

To evaluate the longitudinal uniformity, LRU, we have reported the light yield as function of the source distance from the PMT and fit the distribution with a linear function, as reported in Figure 4.8. The obtained angular coefficients are of

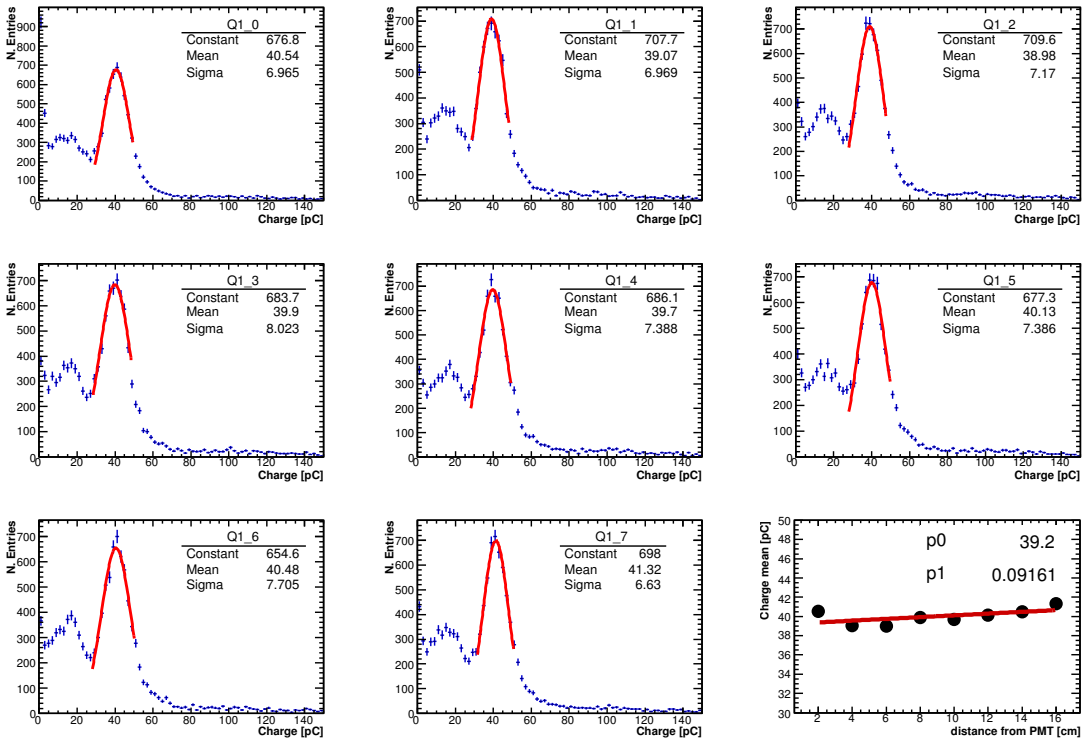

Figure 4.7: *Fits used to extract the peak position during the scan of the Opto Materials 01 crystal, wrapped with Tyvek and plot of these values as function of distance.*

$\sim$ 0.4 $N_{p.e.}$/(MeV $\cdot$ cm) for all three wrapping materials.

The Al wrapping provided the worst light yield ($\sim$79 $N_{p.e.}$/MeV with the source in the central position), while the best performance, for every scan point, has been obtained with Teflon wrapping ($\sim$91 $N_{p.e.}$/MeV), as shown in Figure 4.8 (right). The Tyvek wrapping provided a LY of about $\sim$ 89 $N_{p.e.}$/MeV, which is just few % below that of Teflon.

Summarizing, a full wrapping with Teflon or Tyvek provides a light yield increase of a factor about 20% with respect to the configuration with Al. However, although the Teflon provided the best performance, tests on all the other crystals have been carried out with 2 layers of Tyvek wrapping, due to the fragility and difficulty to repair Teflon, especially when presence of optical grease.

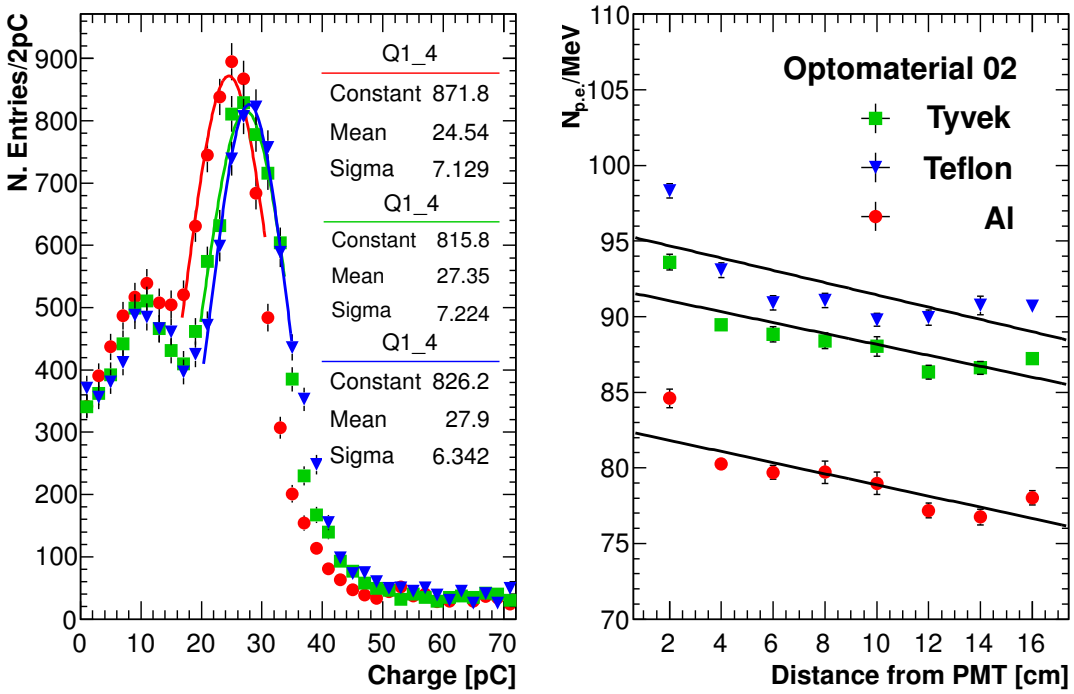

Figure 4.8: *Charge distributions in the central position of the scan of the Opto Materials 02 crystal, wrapped with Tyvek, Teflon and aluminum (left). The mean value has been extracted with a gaussian function in each scan point to evaluate the number of photoelectrons produced per MeV as a function of the distance (right).*

4.1.3.2 Light Yield and Longitudinal Response Uniformity

All the CsI crystals tested have been wrapped with two layers of Tyvek. The scan results with and without optical grease are reported in Figures 4.9 to 4.11.

The plots show:

- a light yield of about 90 - 100 $N_{p.e./MeV}$ and an improvement of a factor $\sim$ 1.6 when using the optical grease for coupling;
- relevant differences between crystals from the same company (i.e. we observe a 45% better light yield with Opto Materials sample 01 with respect to sample number 02, see Figure 4.11);
- similar performance for ISMA crystals and Opto Materials 02, while Opto

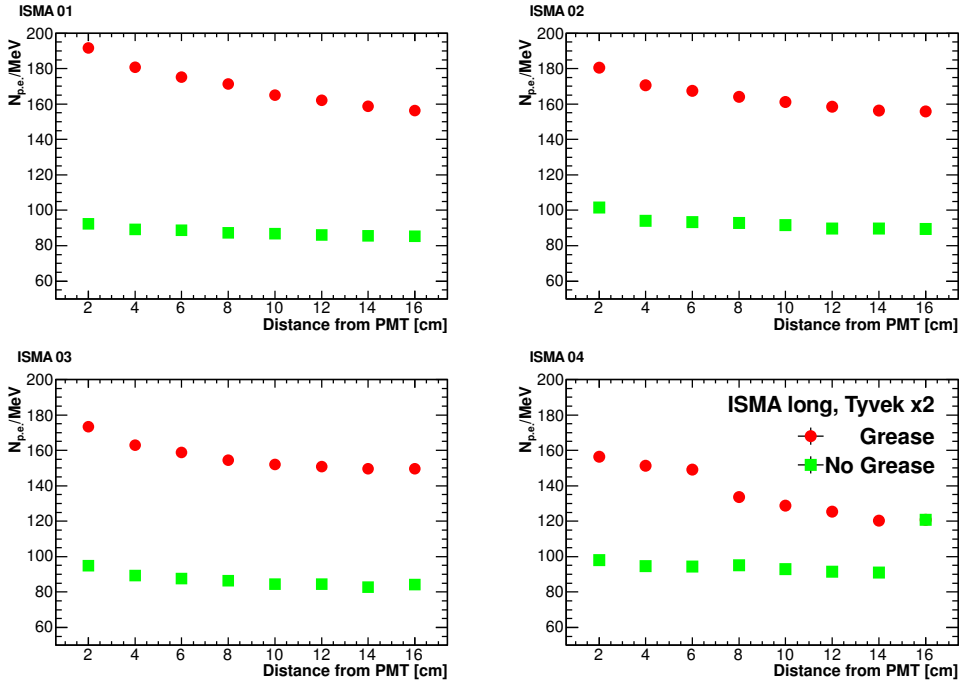

Figure 4.9: *Number of photoelectrons produced per MeV in the ISMA's long crystals (number 01-04), as function of the distance of the source from the PMT.*

Materials 01 has much better uniformity and LY (130 $N_{p.e.}$/MeV with respect to $\sim$ 100 $N_{p.e.}$/MeV);

- larger signals are observed closer to the PMT, because of the collection of direct light;
- the charge resolution is $\sim$18% ($\sim$25%) with (without) optical grease.

The LY, normalized to its value in the central position, has been plotted as a function of the scan position and fitted with a linear function, as shown in Fig. 4.11. Angular coefficients of the fitted slopes are reported in Figure 4.12, showing a LRU better than 0.5%/cm in most of the crystals.

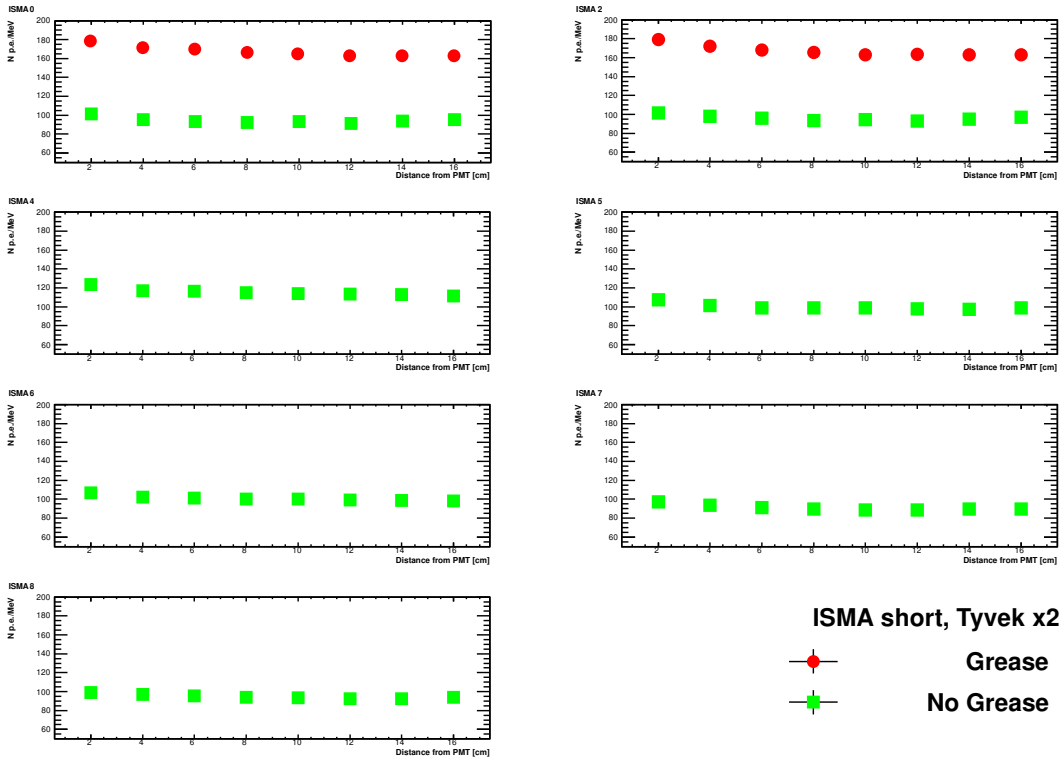

Figure 4.10: *Number of photoelectrons per MeV produced in the ISMA's short crystals (number 05-11), as function of the distance of the source from the PMT.*

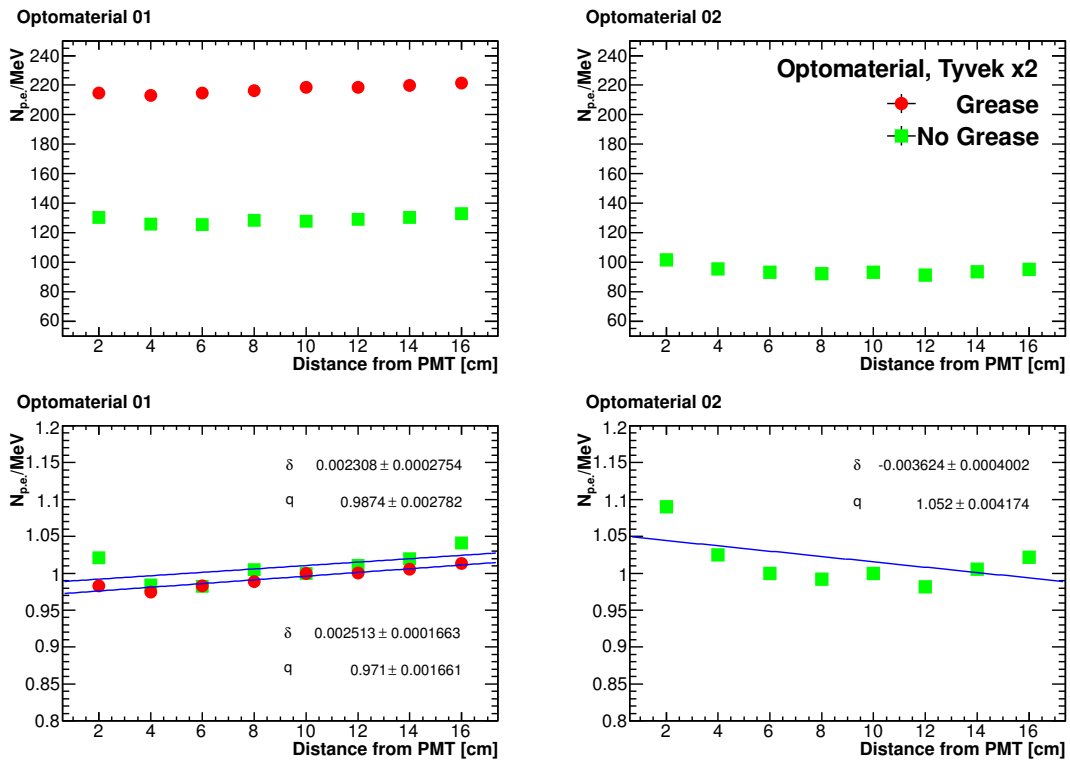

Figure 4.11: *Number of photoelectrons per MeV produced in the Opto Materials 01 (top left) and 02 (top right) crystal samples as function of the distance of the source from the PMT. LY normalized to the number of photoelectrons per MeV produced in the central scan position and fitted with a line function to evaluate the longitudinal response uniformity (δ) in %/cm.*

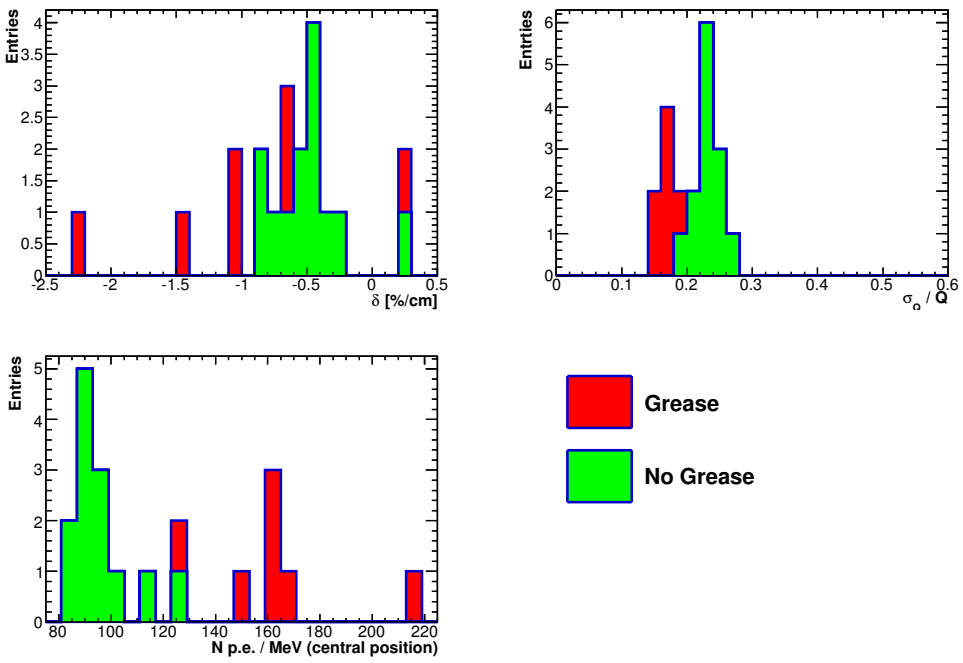

Figure 4.12: *Slopes distribution (in %/cm) provided by the linear fit on the LY normalized as function of the distance from the PMT (top left), resolution distribution (top right) and LY distribution obtained in the central scan position (source at 10 cm from the PMT) for all the pure CsI crystals testesd (bottom left).*

4.1.4 Results with BaF_2 crystals

The four BaF_2 crystals have been tested using the same experimental setup. In this case a Teflon wrapping was preferred, due to the smaller emission wavelength of the fast component of BaF_2. The effect of the optical grease coupling has been studied for every crystal.

4.1.4.1 Study on wrapping

The BaF_2 crystal number 01 has been tested by wrapping it both with three and eight Teflon layers of 25 μ m each. As shown in Figure 4.13, the measured LY with eight layers of wrapping is about 8% larger (in the central scan position) than that with three layers. Being this a negligible improvement, all other crystals have been tested with three Teflon layers only.

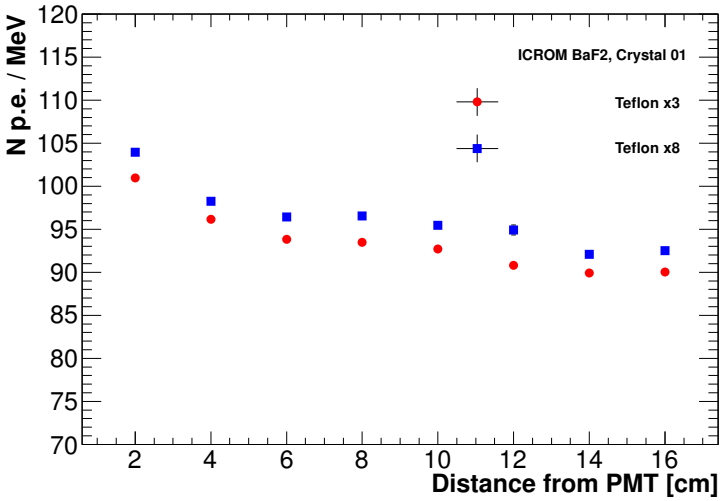

Figure 4.13: *Light yield of the BaF_2 crystal INCROM 01 obtained wrapping with 3 (red) and 8 (blue) layers of Teflon, of 25 μ m each, and coupling in air.*

4.1.4.2 Light Yield and Response Uniformity

The scan results for all the BaF_2 INCROM crystals wrapped with Teflon and coupled the to PMT both in air and with Dow Corning HC 2000 optical grease are reported

in Fig. 4.14. The plots show that:

- the light yield is around 80 - 100 $N_{p.e.}$/MeV (120-180 $N_{p.e.}$/MeV) for a coupling without (with) optical grease;
- larger signals are obtained for source positions close to the PMT, due to the increased collection of direct light;
- the longitudinal uniformity deteriorates when coupling the crystal with grease to the PMT;
- the LRU measurement of INCROM 02 sample with grease is probably affected by a detachment of the crystal from the PMT during the scan test.

As already shown in Fig. 4.14, the LRU deteriorates using optical grease, from (7-11)% to (25-30)% (Fig. 4.15).

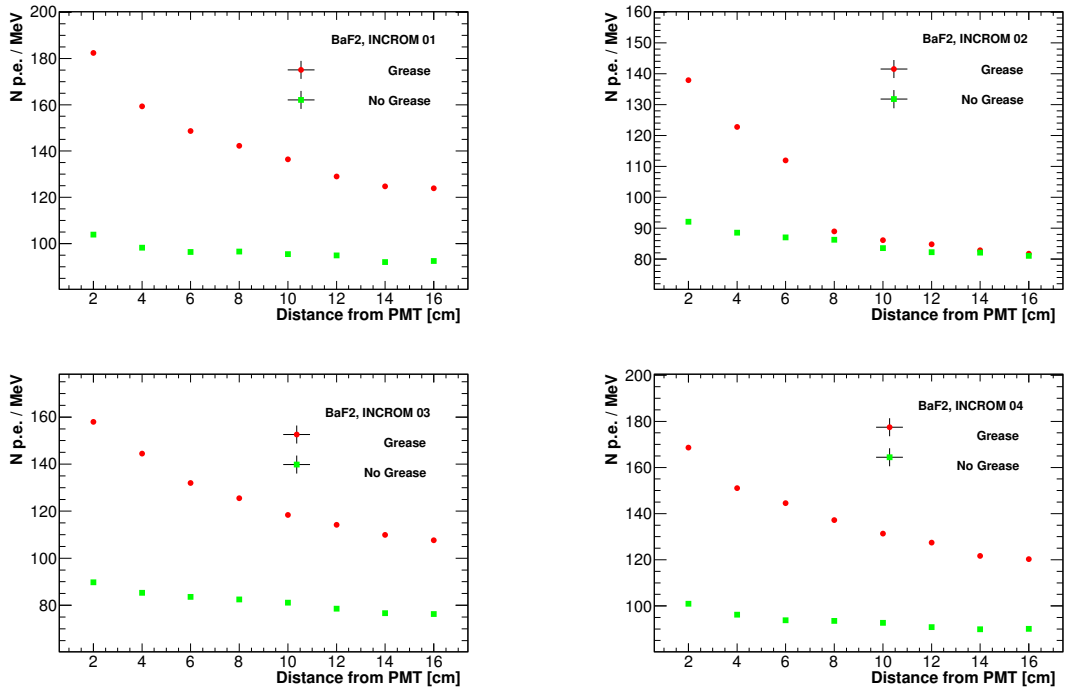

Figure 4.14: *Light yield of BaF_2 INCROM crystals as a function of the distance of the source from PMT. The behavior of INCROM crystal number 02 is probably due to a poor coupling to the PMT.*

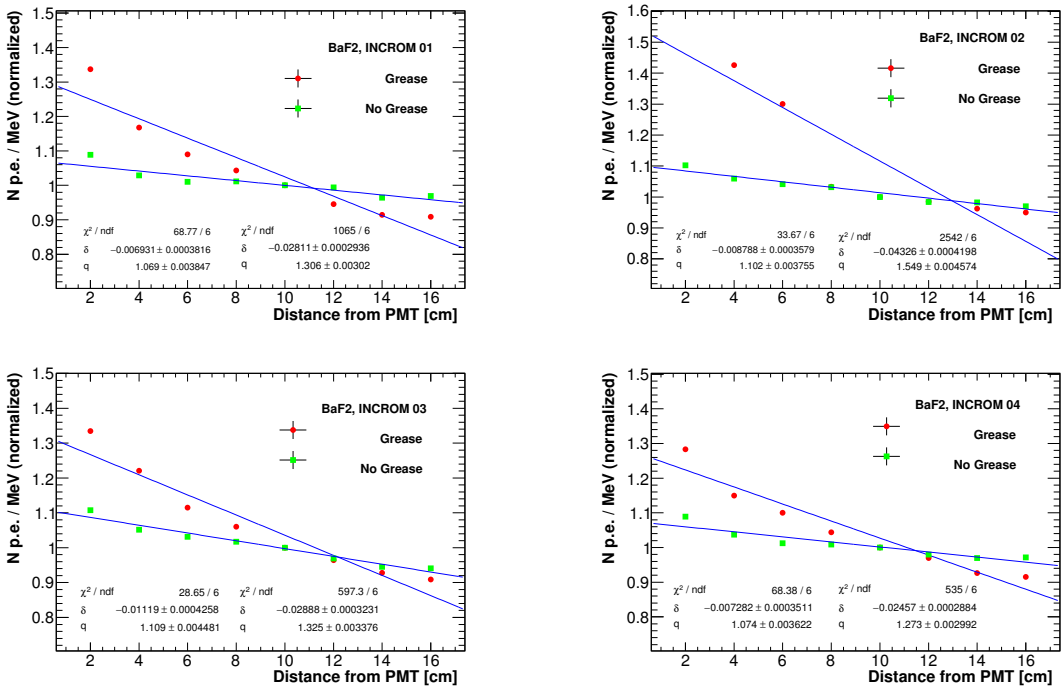

Figure 4.15: *Light yield of BaF_2 INCROM crystals normalized to the central position measurement as a function of the distance of the source from PMT.*

4.2 Irradiation tests with ionization dose and neutrons

The Mu2e calorimeter will operate in a high radiation environment. Simulation studies shows that in the hottest regions each crystal will absorb 30 krad (300 Gy) of ionization dose and will be exposed to a neutron flux of 6×10^{11} n/cm^2 in three years of running [39]. For this reason, we have tested the variation of the light yield and the response uniformity of undoped CsI and BaF_2 crystals irradiated with a dose and a neutron flux exceeding the one expected in the experiment lifetime and we have compared the performance before and after irradiation.

Irradiation tests with a ionization dose have been performed at the ENEA Calliope facility [43], where a ^{60}Co source is used to produce γs with an energy of 1.25 MeV. The irradiation plant is a large volume pool-type facility, where the source is arranged in 48 bars with cylindrical shape housed along two concentric cylinders. The activity of the source during our tests was 0.35×10^{15} Bq, allowing to reach from 10 to 2 Gy/h at about 5 m distance.

Figure 4.16: *CALLIOPE gamma irradiation plant, (ENEA, Casaccia). It is a pool-type irradiation facility equipped with a ^{60}Co γ-source in a large volume shielded cell.*

Figure 4.16 shows the CALLIOPE plant test area placed at the ENEA Casaccia.

The neutron irradiation tests have been performed at the ENEA Frascati Neutron Generator facility (FNG) [44], which uses a deuteron beam, accelerated up to 300 keV, impinging on a tritiated target to produce a nearly isotropic 14 MeV neutron flux via the T(d,n)α fusion reaction. The maximum neutron intensity is 0.5×10^{11} n/s, close to the target, with a uniform production. The desired neutron intensity is reached by either positioning the crystal at the needed distance or changing the deuteron beam intensity. In Figure 4.17 the test area placed at the ENEA Frascati Neutron Generetor facility (FNG) is shown.

In both irradiation tests, the light yield and longitudinal response uniformity have been measured at different steps of the irradiation program. This characterization has been done with the same setup described in the previous section (Sec. 4.1.1).

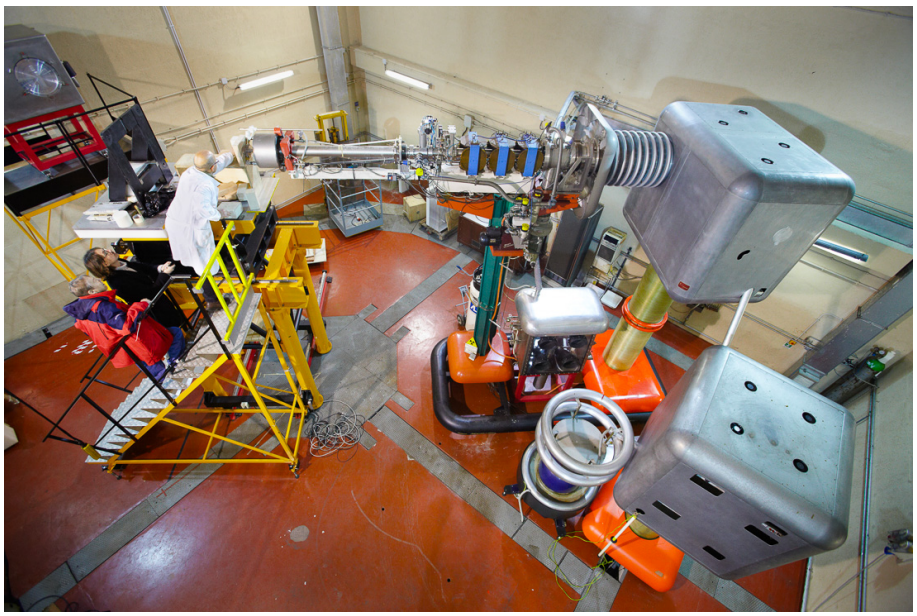

Figure 4.17: *Frascati Neutron Generator facility (FNG, ENEA). It is a 14-MeV neutron generator based on the T(d,n) α reaction and produces up to 10^{11} n/s in steady state or pulse mode. FNG can also produce 2.5-MeV neutron via the D(d,n) 3He fusion reaction.*

4.2.1 γ irradiation test

The old 2014 pure CsI crystal from SICCAS has been irradiated at the CALLIOPE facility, by positioning it perpendicular to the incoming γ, a condition more demanding than the experimental configuration, where the dose derives from particles impinging on the transverse face.

The total dose absorbed by the crystal was $\sim$ 90 krad (900 Gy) in 9 days, with the following irradiation scheme: two days at $\sim$ 0.2 krad/h and seven days at $\sim$ 0.5 krad/h. That total dose corresponds to about three times that expected in the hottest region of the calorimeter (i.e. the innermost ring around the beam axis) in three years running [39].

The measurements on the crystal have been done with the same setup previously described, using a ^{22}Na radioactive source, (sec. 4.1.1) just before the irradiation test, for reference, and at 5.3, 20.6 and 90.8 krad, without any wrapping on crystals and with the PMT coupled in air.

In Figure 4.18, the light yield as a function of the position of the ^{22}Na source along the crystal is shown for different irradiation doses. A large longitudinal response uniformity is present before and after irradiation.

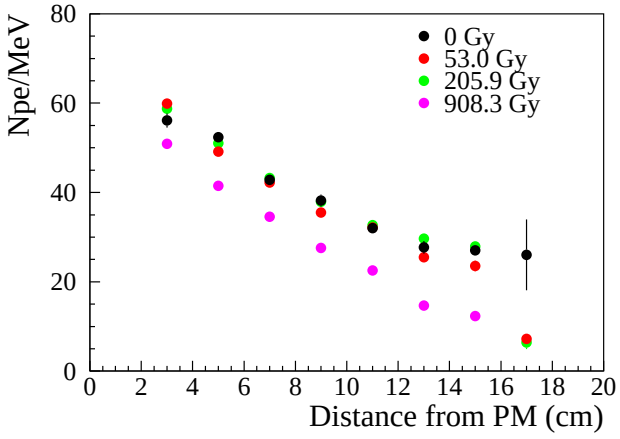

Figure 4.18: *Light yield of the SICCAS CsI crystal irradiated at CALLIOPE facility as a function of the longitudinal position, at different integrated doses (given in Gy, where 1Gy = 0.1 krad). The crystal has been tested without wrapping and coupled to the PMT in air.*

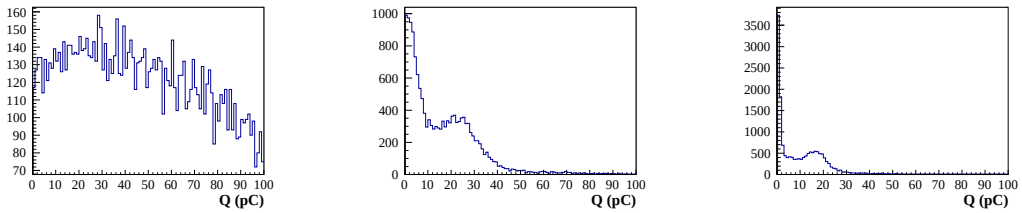

Figure 4.19: *Charge of the undoped CsI SICCAS crystal in the first position, source at 3 cm from the PMT, after 90 krad dose. Left to right: just at the end of the irradiation test, after 30 minutes and three hours. Fluorescence effects are clearly visible. Immediatley after the end of the irradiation, the peak due to the 511 keV photon is not even visible.*

A negligible light yield reduction is observed for doses up to 20 krad, while for the last irradiation step the decrease is $> 20\%$. This change increases also with the source distance from the readout system. The results obtained at the end of the crystal, 17 cm away from the PMT, suffer from the fluorescence which is present after the irradiation exposure and provide a poor fit during the LY extraction.

The fluorescence of the crystal increases with the instantaneous irradiation dose, but it is only a temporary effect and its intensity quickly decreases with time. Fluorescence appears as random small pulse heights and is clearly observable both at the scope and at the digitizer. Its effect is clearly visible in Fig. 4.19, where the charge of the CsI crystal in the same position (3 cm from the PMT) has been measured just as soon as we have concluded the final step of the irradiation test, corresponding to 90 krad, and after having waited additional 30 minutes and 3 hours before repeating the measurement. In the first case, the peak is not even visible, while it reaches 25 pC after 30 minutes, decreasing to 18 pC after 3 hours.

The response recovery of the irradiated crystal has been studied by repeating the measurement six days and one month after the end of the irradiation test. As shown in Figure 4.20 left, no significant recovery is obtained. This is consistent with expectations from literature [45] and other measurements carried out by the Caltech group with other CsI crystals [46]. This confirms the permanent deterioration of undoped CsI crystals after a large dose of γ irradiation.

The behavior of the irradiated CsI has been also compared with the one obtained for another crystal from SICCAS, coming from the same production batch. The

comparison, reported in Fig. 4.20 right, shows consistent results.

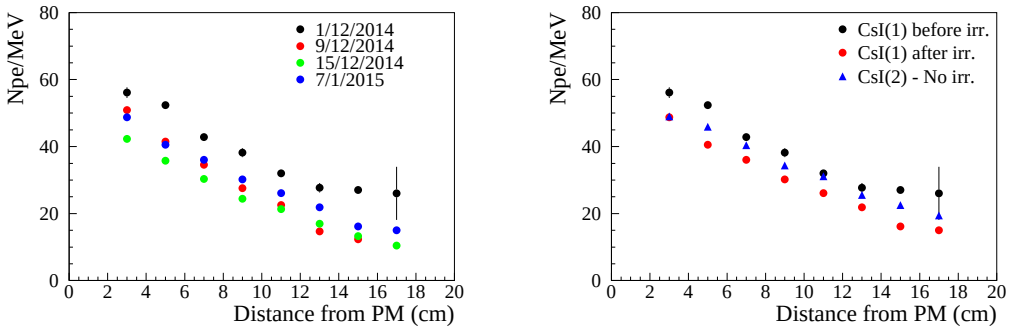

Figure 4.20: *Left: LY of the CsI crystal as a function of the source position along the crystal axis, before the irradiation test (black) and after 90 krad (red). The recovery of the crystal is studied by repeating the measurement after six days (green) and one month (blue). Right: comparison of the LY for the irradiated crystal before (black) and after (red) the irradiation test and a companion crystal from the same production batch (blue).*

After the irradiation test, we have measured the LY and LRU wrapping the two CsI crystals with a Tyvek foil and then adding optical grease for the PMT coupling. Both wrapping and grease increase the light yield, which is ~ 80 $N_{\rm pe}$/MeV (with the source in the crystal center position) when both wrapping and grease are used. LRU results are reported in Figure 4.21. The slope for the longitudinal uniformity remains similar between the irradiated and not irradiated crystal. The wrapping largely improves LRU, which becomes $\pm 20\%$ recovering light loss by internal reflection. With grease, the LRU deteriorates to $\pm 30\%$.

4.2.2 Neutron test at FNG

Four different $(3 \times 3 \times 20)$ cm^3 crystals have been tested with a large neutron fluency at FNG: three undoped CsI from SICCAS (China), ISMA (Ukraine) and OPTO MATERIALS (Italy) companies and one BaF_2 from INCROM (Russia). The irradiation schedule is reported in Table 4.1.

The total flux delivered, 9×10^{11} n/cm^2, corresponds to about 1.5 times the maximum total flux expected for the first calorimeter disk and 3 times the flux

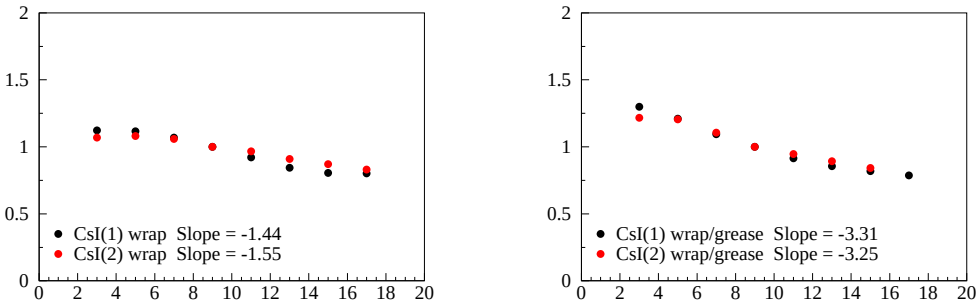

Figure 4.21: *LRU of the irradiated and non-irradiated CsI crystals with Teflon wrapping (left) and adding also optical coupling with grease (right). LRU distributions have been fit with a linear function. Results for the slope parameter are reported in figures.*

Day	Total neutron flux
1	1×10^{11} n/cm^2
2	3×10^{11} n/cm^2
3	5×10^{11} n/cm^2
4	9×10^{11} n/cm^2

Table 4.1: *Integrated neutron fluency at the FNG as a function of the exposition day.*

expected for the second disk in three years of running [39].

Light yield and LRU for Tyvek wrapped CsI crystals and Teflon wrapped BaF_2 crystal have been measured each day just before the irradiation. Crystals were optically coupled with an air gap to the PMT. The measurements have also been repeated 10 and 22 days after the end of the irradiation test.

In Figure 4.22, the light yield of the four tested crystals is reported as a function of the distance of the source from the PMT. The LY increases with the neutron flux due to fluorescence effects and induced activation. Measurements performed several days after the irradiation test show a decrease of the light yield as related to the reduction of these effects. Indeed, comparing the first to the last measurements, a decrease of 10 - 20% is visible for the undoped CsI crystal from Opto Materials

company, while no change is observed for the ISMA one. The SICCAS crystal has a completely different behavior of the response along the crystal axis before and after irradiation, with a strong deterioration of the uniformity slope. For the BaF_2, the measured decrease in LY (integrated in 100 ns to quote only the fast component) is of the order of few percent after 10 days, in agreement with measurements at lower fluency reported in [46]. Figure 4.23 shows the light yield normalized to the value obtained in the central scan position, which is used to evaluate the LRU. All crystals, except the SICCAS CsI, show a good LRU after irradiation, with a total uniformity well below 10% and negligible deterioration. To the contrary, LRU for SICCAS CsI changes from 5% to 15% after neutron irradiation.

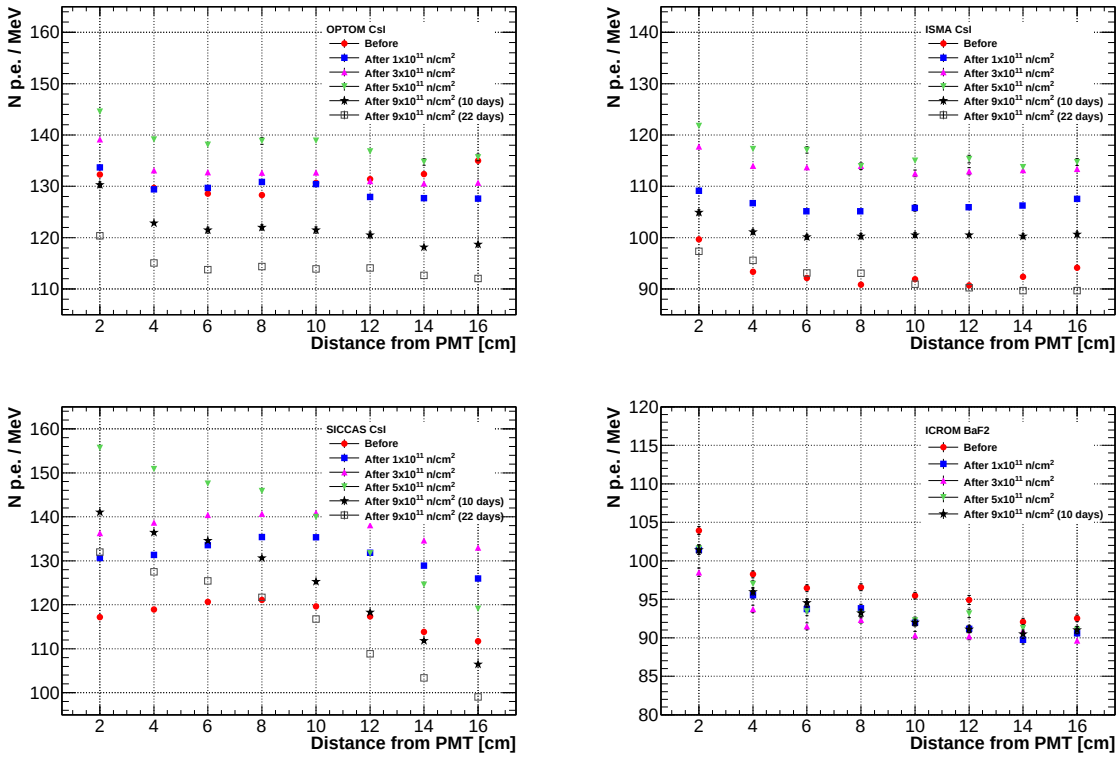

Figure 4.22: *Measurements of the light yield as a function of the distance between the source and the PMT during neutron irradiation for CsI crystals from Opto Materials (top-left), ISMA (top-right), SICCAS (bottom-left) and for BaF_2 from INCROM (bottom-right) companies.*

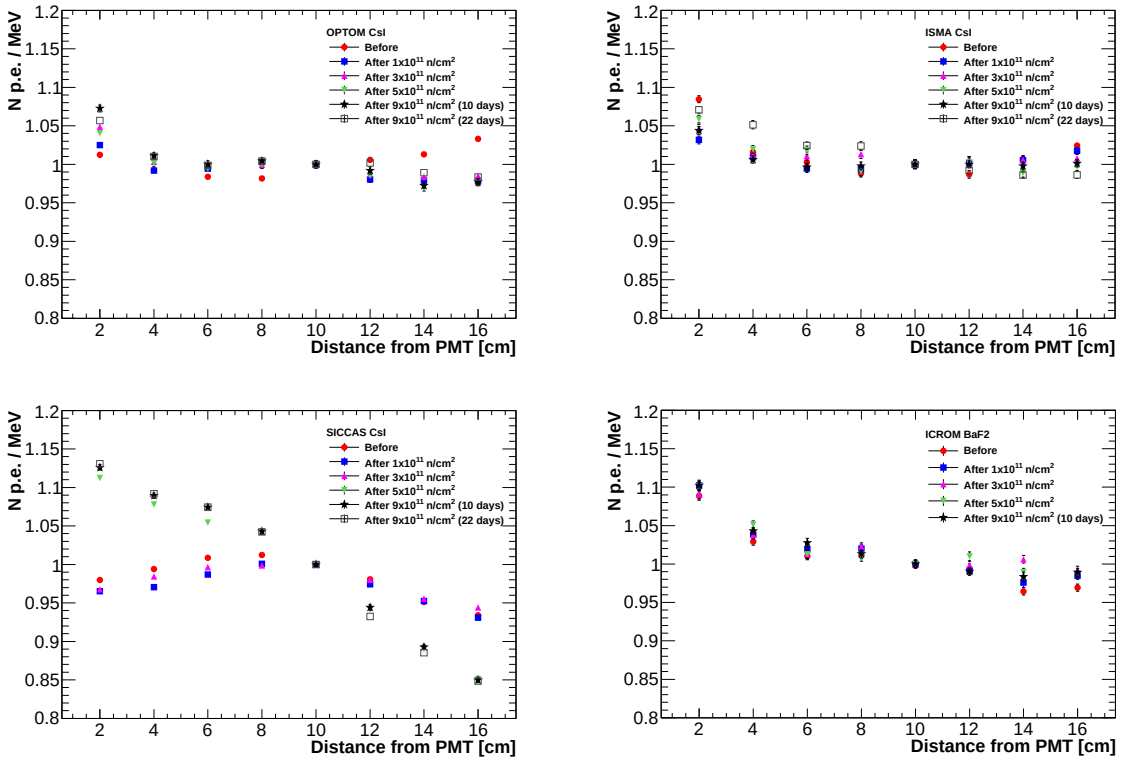

Figure 4.23: *Light Yield normalized to the central scan position value used to evaluate the Longitudinal response uniformity measurements during neutron irradiation test for CsI crystals from Opto Materials (top-left), ISMA (top-right), SICCAS (bottom-left) and for BaF_2 from INCROM (bottom-right) companies.*

Chapter 5

The backup solution: undoped CsI crystals + MPPCs

Due to the delay in the development of the solar blind APD and as an alternative backup choice to the Mu2e calorimeter design, we have tested the timing performance and the energy resolution of undoped CsI crystals readout by MPPC, by optically coupling them both with optical grease and in air. The crystals were wrapped with two Tyvek layers of 100 μm thickness each.

In this chapter, I present the progresses done during the last year for this R&D. I will first show the results obtained with single crystals tested with cosmic rays and then report the measurements done with a 3 $\times$ 3 crystal array exposed to an electron beam with energy between 80 - 140 MeV at the Beam Test Facility of LNF. For 100 MeV electrons, we have measured an energy resolution of $\sim$ 7%, which is fully dominated by energy leakage and a time resolution of $\sim$ 110 ps. The dependence of the resolution on the beam impinging angle has also been studied.

5.1 Single channel performance

As already shown in the previous chapter, Opto Materials crystals have the highest LY and better LRU of the procured undoped CsI crystals. Both crystals have been coupled to the SPL MPPC and have been tested with cosmic rays to evaluate the

timing resolution. The SPL MPPCs are the same used for the assembly and test of the 3×3 matrix prototype.

5.1.1 Experimental setup

In order to optimize the light collection, while simplifying the assembly, crystals were wrapped with 100 μm-thick Tyvek foils, covering both the four faces along the crystal axis and the side opposite to the readout system. Each crystal was then placed between two small plastic scintillators, *fingers*, perpendicular to each other and positioned one below and one above the crystal under test. In this way, the two finger coincidence covers 1 cm^2 area on the long surface of the crystal, as shown in Figure 5.1. For each crystal, the effect of the Rhodosil Paste 7 optical grease coupling has also been studied. The whole system has been assembled inside a light tight black box.

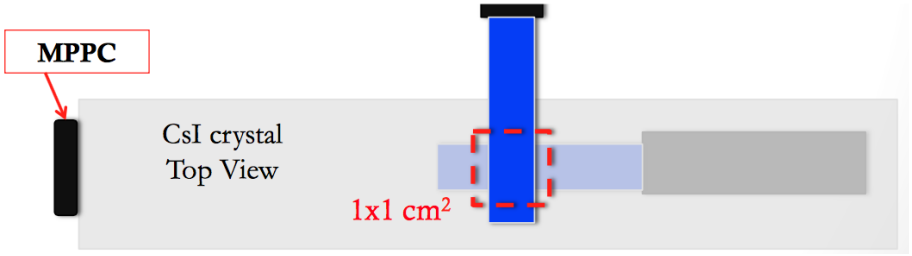

Figure 5.1: *Schematic layout of the experimental setup used to test the timing performance of a single crystal (grey rectangle) readout by an MPPC (black rectangle). Also the two perpendicular finger scintillators, used for triggering, are shown (blue and light blue rectangles).*

The data acquisition system is composed by a trigger board, that makes the coincidence between the two discriminated finger signals, and a CAEN DT5751 digitizer at 1 Giga samples per second, which acquires finger and crystal signals. A copy of each signal, obtained with a fan-in fan-out NIM module, has also been sent to a digital scope. Figure 5.2 shows a typical cosmic ray event triggered by the finger coincidence.

Due to the low coincidence rate, 0.006 Hz, it takes about two days to collect a reasonable statistics of $\sim$ 1000 events. A program analyzes data as soon as the run is completed.

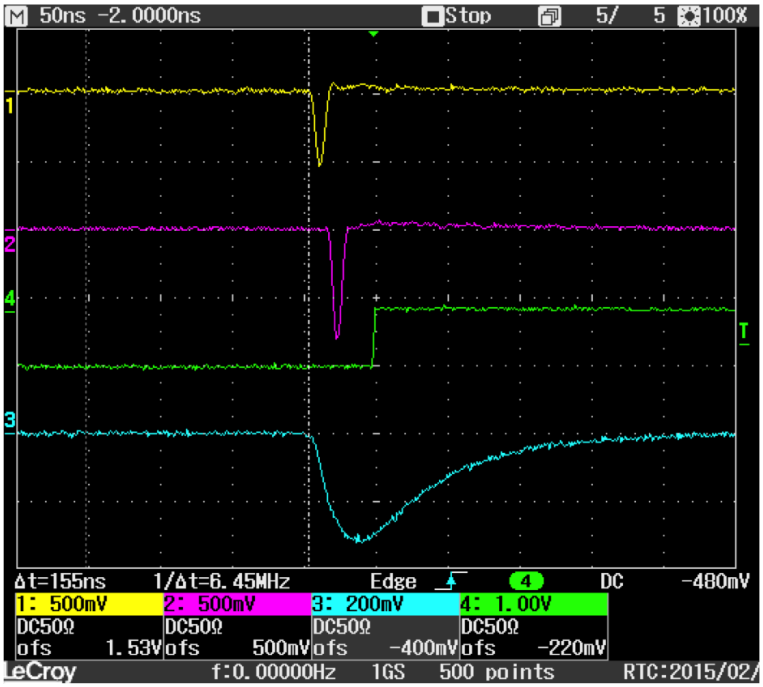

Figure 5.2: *Picture from the scope of an event due to a cosmic ray passed through both fingers. From top to bottom the signal produced by the top finger (yellow), bottom finger (purple), the coincidence of the two used as trigger (green) and crystal (blue) are shown. The bottom finger drives the trigger, so the purple signal is delayed of few ns.*

The goal of this test is to measure the time resolution at the energy released by a minimum ionizing particle (MIP) in the crystal. In order to set the energy scale, we compare the charge spectra of the MIP with that from a radioactive source. Our ^{22}Na source emits 511 keV back-to-back photons from annihilation and its charge spectrum has a corresponding mean value of (11.57 ± 0.17) pC. In Figure 5.3, it is possible to see an example of the charge plot obtained with cosmic rays, where the most probable value, MPV, is (463.3 ± 1.13) pC. Comparing these two values, the energy released by a MIP in a crystal results to be around 20 MeV, in good agreement with MC expectation. The amplifier used for the CR test was a prototype version with a gain of 3.

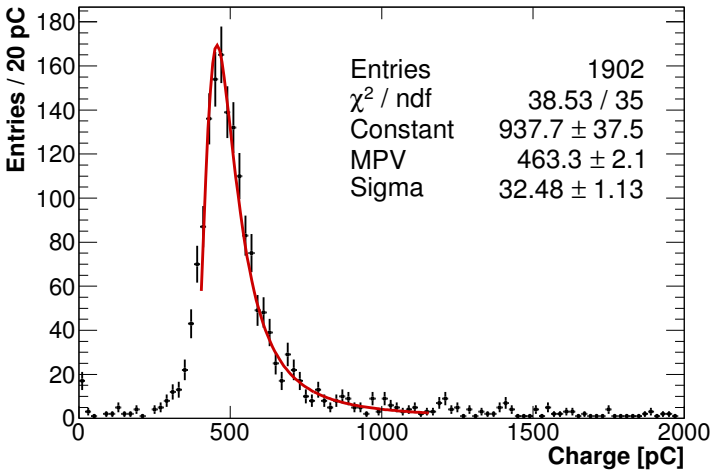

Figure 5.3: *Charge distribution in the Opto Material CsI crystal 01 readout by the SPL MPPC. The most probable value, MPV, has been estimated through a Landau fit.*

5.1.2 Time Measurement

Waveform examples obtained for one finger and for the crystal, are shown in Figure 5.4 left and Figure 5.4 right respectively. To extract the time, I first evaluated the maximum value of pulse height for the finger and crystal signals and I then made a fit with a 4^{th} order polynomial function between the times at two fixed thresholds: *i*) the position of the time sample corresponding to a pulse height of 10 mV above the signal baseline and *ii*) the one at maximum pulse height less 1 ns (t_{max} - 1). The fit is shown in Figure 5.4.

Both for fingers and crystals the measured time is taken at a constant fraction CF, set at 25%, of the maximum signal amplitude. Similarly, the crystal time is evaluated as the value of the fit function position at 25% CF. In order to eliminate the jitter due to the trigger, I subtracted half sum of the finger time:

$$t = t_c - \frac{t_1 + t_2}{2} \ , \tag{5.1}$$

where t_1 and t_2 are the time of the bottom and top fingers respectively and t_c is the crystal time. The distribution of the finger times half difference, $(t_1 - t_2)/2$, after slewing correcting for the time, is reported in Figure 5.5. The time jitter of the trigger of the trigger, $(t_1 + t_2)/2$, is evaluated as the σ provided by the gaussian fit that is $\sim$ 170 ps.

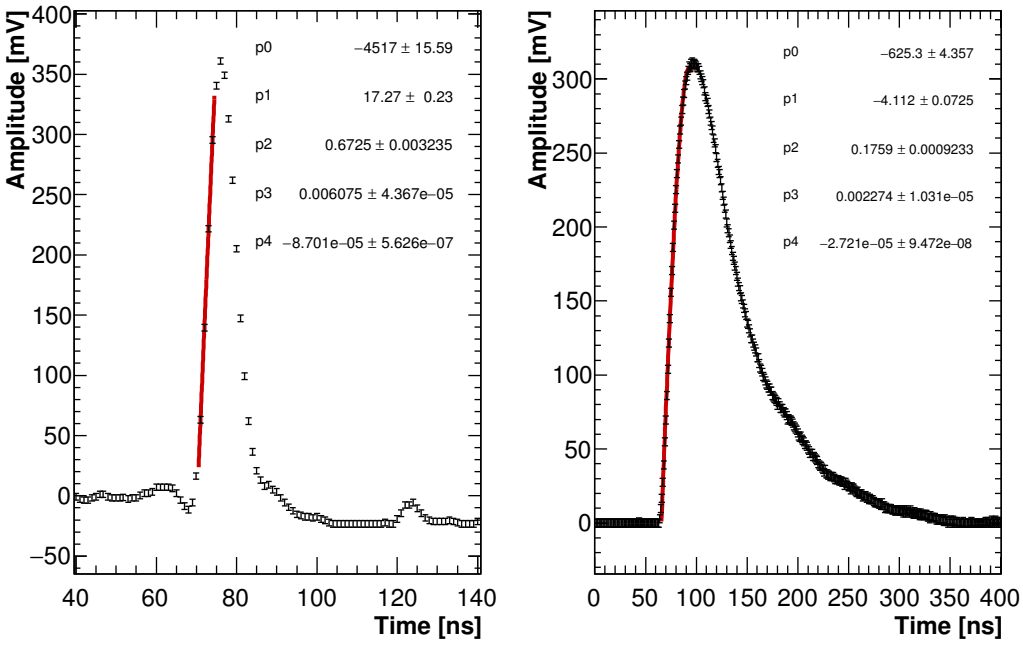

Figure 5.4: *From left to right, signals of the top finger and of the Opto Materials 01 crystal acquired by the CAEN DT5751 digitizer at 1 Gsps rate. Also the 4th order polynomial fit is shown.*

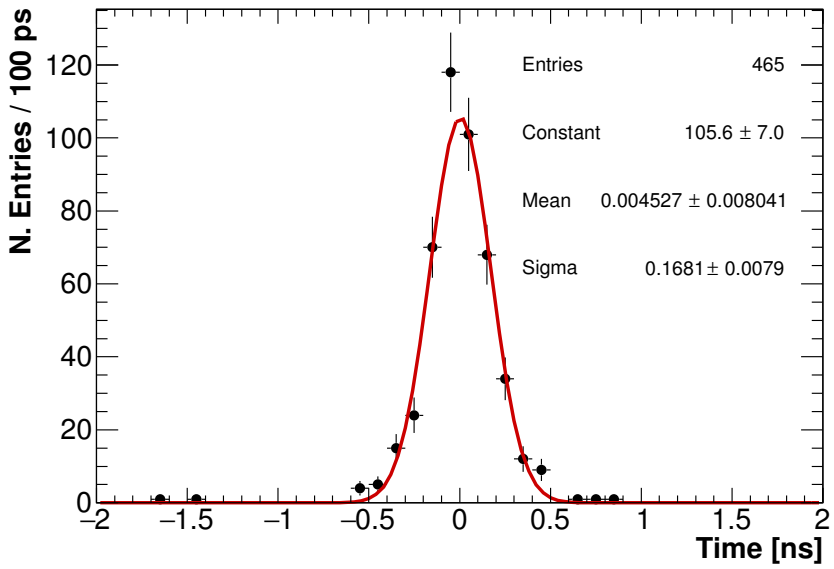

Figure 5.5: *Half difference of finger times distribution, $(t_1 - t_2)/2$. The red line is the gaussian fit.*

The detector timing properties are determined primarily by time slewing (or time walk) resulting from the signal rise time, shape and amplitude. The dependence of the time, t, from the charge, Q, is shown in Figure 5.6. This behavior is described by the function:

$$t = \frac{p0}{\sqrt{Q}} + p1\,, \tag{5.2}$$

where $p0$ and $p1$ are parameters evaluated by a fit to the dependence in FIg. 5.6 minimizing the χ^2.

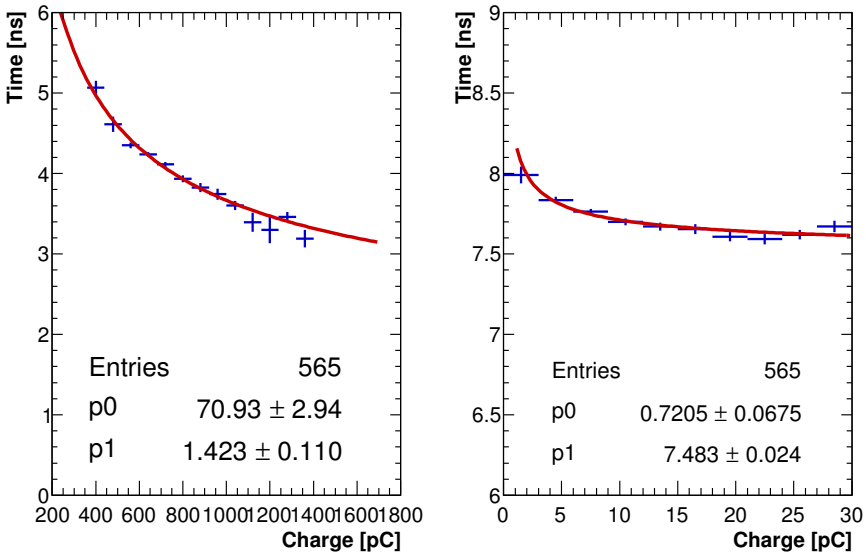

Figure 5.6: *Left: time of crystal evaluated as* $t = t_{crystal} - \frac{t_1+t_2}{2}$ *as a function of the signal charge. Where* t_1 *and* t_2 *are the bottom and top finger times respectively. Left: half difference of finger times as a function of the signals charge. The fit reported (eq. 5.2) is used to evaluate the slewing correction.*

After the time slewing correction, the time distributions of the Opto Material 01 crystal tested, wrapped with Tyvek and Teflon and coupled with and without optical grease to the SPL MPPC, are reported in Figure 5.7. The time resolution, σ_c is the "Sigma" value of the gaussian fit, reported in the same figure.

The best performance is obtained with optical grease coupling: (328 ± 12) ps with Teflon and (333 ± 12) ps with Tyvek wrapping. Coupling in air deteriorates the resolution: (409 ± 16) ps with Teflon and (455 ± 13) ps with Tyvek wrapping.

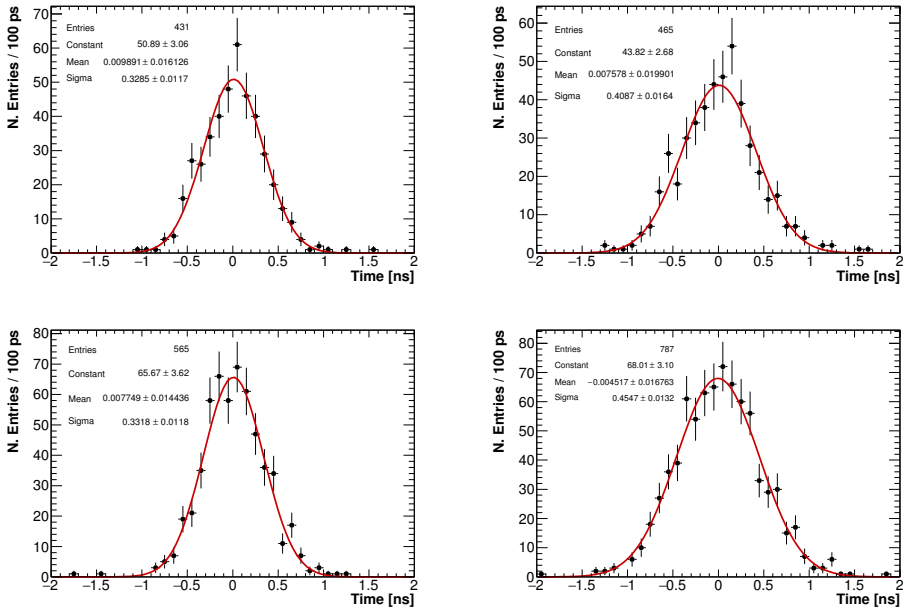

Figure 5.7: *Time distributions obtained with the constant fraction method after the slewing correction of the Opto Material 01 crystal. This crystal has been tested wrapped with Teflon (top) or Tyvek (bottom) and coupled to the MPPC both with (left) and without (right) optical grease.*

From Figure 5.5, the trigger jitter obtained is $\sigma_f \sim (168 \pm 6)$ ps. The time resolution after jitter subtraction is evaluated as:

$$\sigma = \sqrt{(\sigma_c^2 - \sigma_f^2)} \tag{5.3}$$

In Table 5.1, all the time resolutions obtained testing crystal + SPL MPPC exploiting cosmic rays are summarized. These values are estimated after subtraction of the trigger jitter contribution.

	Tyvek	Tyvek and grease	Teflon	Teflon and grease
Opto Materials 01	~ 410	~ 270	~ 375	~ 260
Opto Materials 02	-	~ 280	-	-
ISMA 05	-	~ 265	-	-

Table 5.1: *Time resolution @ 22 MeV given in ps. The value reported are jitter subtracted. The symbol "-" means that this case has not been measured.*

Since the tests at the Frascati Neutron Generator facility (FNG, ENEA) showed

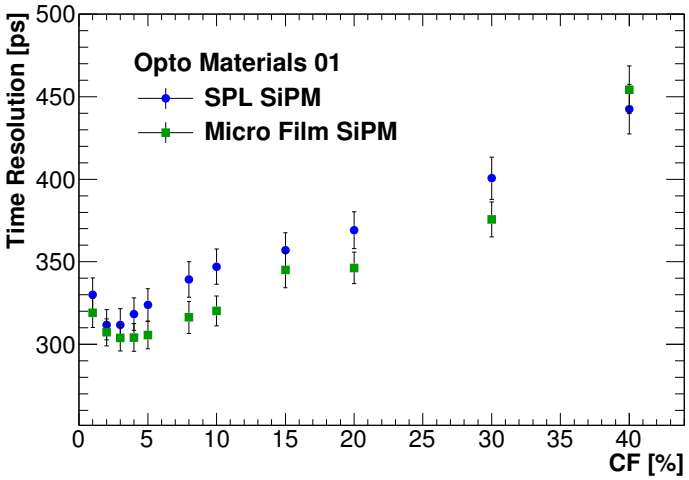

Figure 5.8: *Time resolution as a function of the constant fraction threshold value of the Opto Material 01 with grease coupling. For both the SiPMs, the best resolution is obtained with CF = 3%.*

a darkening effect on the silicon layer of the SPL-MPPC [50], another kind of MPPC with a different cover layer has also been tested. These are the so called Micro Film MPPC. As shown in Sec. 5.2.3, an improvement of the time resolution is obtained for the electron beam by optimizing the CF value. In this final test, I evaluated the time in a similar manner, by using two variable thresholds for the fit range (the fit function remains a 4th order polynomial) at respectively 0.1% and 85% of the signal

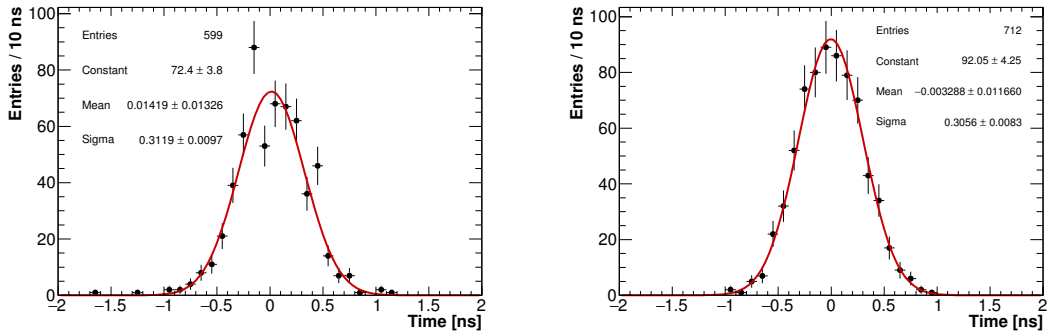

Figure 5.9: *Time distributions after slewing correction of the Opto Materials 01 crystals wrapped with Tyvek and readout by a SPL MPPC (left) and a Micro Film SiPM (right), coupled with optical grease. Trigger jitter has not been subtracted. The time resolutions obtained are (324 ± 10) ps and (306 ± 8) ps respectively.*

maximum amplitude. These threshold values are obtained performing a scan and minimizing the time resolution.

Therefore, as shown in Figure 5.8, a scan on the time resolution as a function of the CF threshold has been carried out. The CF value used for all tests has been chosen as the value which minimizes the time resolution of the crystal, that is CF = 3%. For this purpose, only the Opto Material 01 coupled with grease to both SPL and Micro FIlm photosensors has been tested, the optimized CF value is similar in both cases.

The timing performance of the Opto Material 01 crystal wrapped with Tyvek and coupled to this device using optical grease is reported in Figure 5.9. For the same configuration the SPL MPPC (the Micro Film SiPM) shows an improvement of $\sim 2\%$ ($\sim 8.5\%$) of the time resolution with respect to the previous method.

5.2 Test Beam

At the end of the single crystal tests, I assembled a small matrix of pure CsI crystals. Energy and time response and resolution has been measured using 80 - 130 MeV electron beam at Frascati Beam Test Facility (BTF).

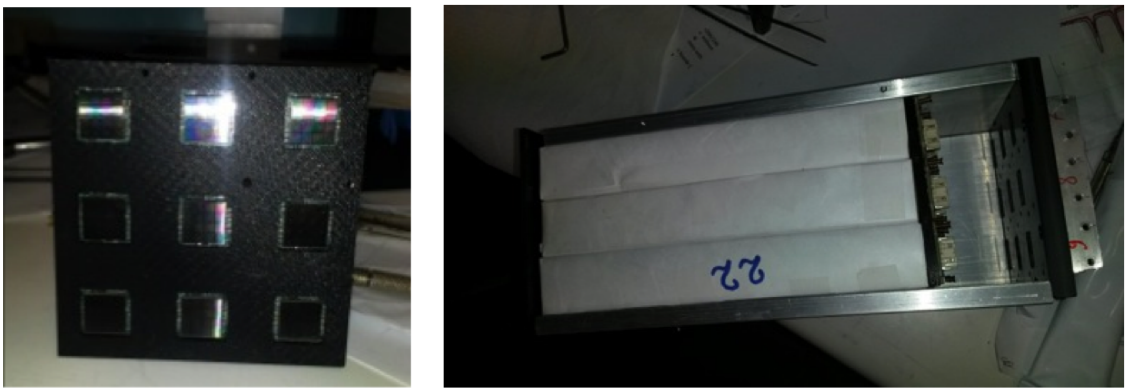

Figure 5.10: *Test beam: (left) MPPC Holder, (right) matrix assembled.*

5.2.1 Matrix prototype

The calorimeter prototype consists of nine $3 \times 3 \times 20$ cm^3 undoped CsI crystals wrapped with 100 μm thick Tyvek arranged into a $\sim$ 1 cm thick aluminum matrix. The nine used crystals have been previously tested (Ch. 4) with the ^{22}Na source to evaluate LY and LRU when coupled to a PMT and with cosmic rays, coupled to an SPL MPPC (Ch. 5.1.2), to evaluate their time resolution. For this matrix I have used two crystals produced by Opto Materials [48], while the remaining 7 came from ISMA (Ukraine) [49].

In the matrix, the back side of each crystal has been coupled to a large area 9×9 cm^2 MPPC_TSV_SLP photosensor by means of Rhodorsil 7 silicon paste. As already stated, these new MPPCs are formed by an array of sixteen 3×3 mm^2 cells with 50 μm pixels, for a total of 57600 pixels. The TSV technology, used in these MPPCs provides reduced cross-talk and dark rate and very fast signals. The operating voltage, V_{op}, is set to 55 V, about 3 V above the breakdown voltage, corresponding to an average gain of 1.3×10^6 and a particle detection efficiency (PDE) of $\sim$ 35-40% around 300 nm. The response uniformity of the 16 cells is excellent, as well as the gain uniformity among different MPPCs: variations of V_{op} required to equalize gains across all channels were below 20 mV.

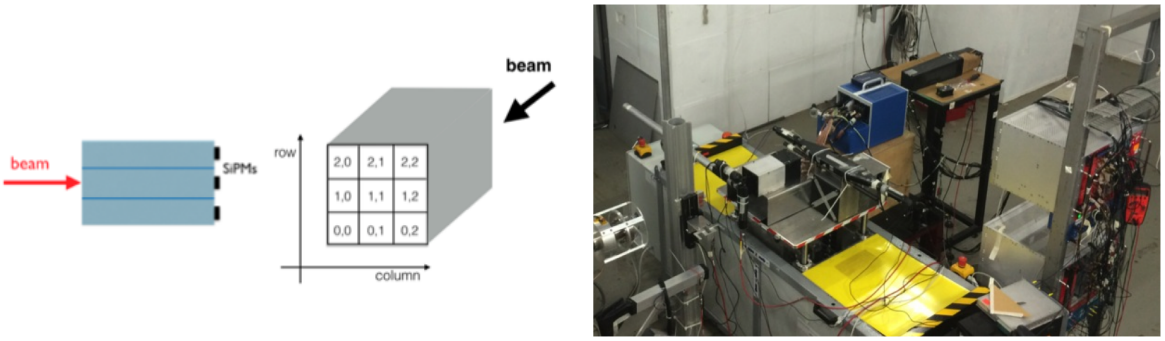

Figure 5.11: *Left: sketch of the test beam configurations. The beam at 0° degree incidence angle with respect to the prototype surface. Center: crystal numbering scheme. Right: BTF experimental hall.*

A custom FEE board has been designed to analogically sum all anode signals while providing an additional amplification of 8. The amplifier bandwidth is $\sim$ 200 MHz and is adequate for the timing measurements. In Figure 5.10, pictures of

one MPPC, one preamplifier, the MPPC holder and the assembled calorimeter are shown.

Two $5 \times 1 \times 1$ cm^3 plastic finger scintillation counters, crossed at 90° were positioned in front of the calorimeter. The timing coincidence between the signals from those counters defined the beam trigger. In addition, one $10 \times 30 \times 4$ cm^3 scintillation counter read out at both ends was positioned above the matrix to provide a cosmic ray trigger. Signals from the MPPCs and the scintillation counters were readout and digitized by 12 bit, 250 MHz WF digitizer boards from CAEN. The logical OR of the beam and cosmic triggers was used during the data taking.

As shown in Figure 5.11 (left), two beam incidence angles with respect to the normal of the prototype front face have been studied: 0°, that is orthogonal incidence, and 50°, that corresponds to the typical incidence angle for the conversion electrons in Mu2e (Fig. 5.11, left).

Each crystal in the matrix is identified by a pair of numbers, (i,j), indicating its row and column number. The reference system is explained in Figure 5.11 (right).

5.2.2 Beam Test Facility, LNF

The pure CsI matrix test beam has been performed at the DAΦNE Beam Test Facility (BTF) at the National Laboratory of Frascati (INFN). It is a beam transfer line designed for the optimized, stochastical production of single electrons/positrons for detector calibration purposes (Fig.5.12).

This facility provides electron and positron beams with tunable energy, from 25 MeV to 750 MeV, and variable intensity, down to a single particle mode, which is particularly suitable for particle detector testing purposes, such as energy calibration and efficiency measurements.

Beam characteristics (spot size, divergence, momentum resolution) are strongly dependedent on multiplicity (number of particles/spill) and energy requested. Energy range, pulse duration, beam intensity and duty cycle can be limited by DAΦNE collider operation. The BTF is a part of the DAΦNE accelerator, consisting of a double ring electron-positron collider, a high current linear accelerator (LINAC),

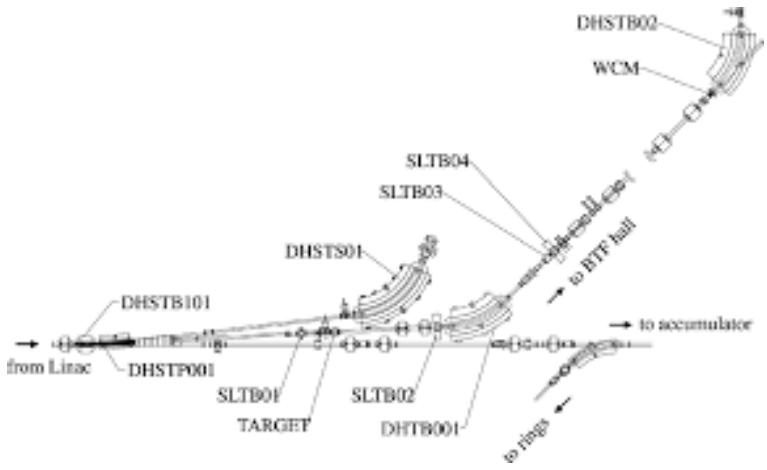

Figure 5.12: *Beam Test Facility at the National Laboratory of Frascati (INFN).*

an intermediate damping ring and a system of 180 m transfer lines connecting the whole system. The LINAC has a triple output (Fig. 5.12): a straight line towards the accumulator (and from there to main ring), the spectrometer line at 6°, dedicated to the LINAC beam energy measurement and finally an exit at 3° for the Beam Test Facility (BTF) channel, which is a completely equipped test facility (variable thickness target, quadrupoles dipoles slits).

A small fast cycling DC magnet (DHSTB101) with a bending angle of 3° has been installed upstream the pulsed magnet (DHSTP001) used for the beam energy measurement. The magnet has been realized by modifying a spare quadrupole with the upper and lower coils connected in series.

The two BTF dipoles (DHSTB001-002) are always on, thus avoiding the long time necessary for their standardization. During beam injection in the collider, DHSTB101 is off, and the beam follows the standard timing sequence and injection scheme: one LINAC bunch per second out the available 50 is bent by 6° by the pulsed magnet DHSTP001 to the hodoscope for energy measurement and the remaining bunches follow the standard path to the accumulator and main rings.

In the BTF operation, DHSPT001 is on and the beam is driven into the new transfer line at 3° . The pulsed magnet DHSTP001 kicks one LINAC bunch per second by the additional 3° necessary to reach hodoscope system. The required switching time between BTF and injection configuration comes now only from ramping the two magnets DHSTB101 and DHSTP001 to the different value, and has been

estimated to be less than 10 seconds [51].

For the purpose of our calorimeter test, an electron beam in the energy range from 80 GeV up to 130 MeV has been used.

5.2.3 Charge and time reconstruction

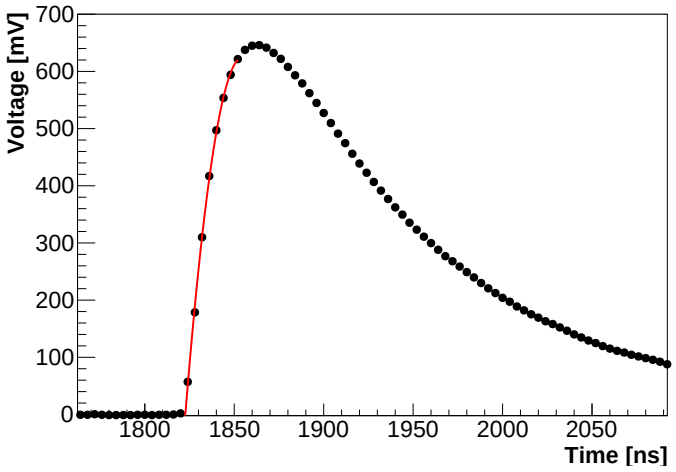

Figure 5.13: *Example of a channel (1,1) waveform for a 100 MeV e^- event acquired by the WFD.*

The charge, Q_i, and time, T_i values, for each event and a given calorimeter channel, i, are reconstructed starting from the digitized signal waveforms with the technique described in this section. In Figure 5.13, an example of a channel (1,1) waveform for a 100 MeV e^- event acquired by the WFD is shown.

As in the previous test on single crystal, the charge (in pC) is estimated by numerical integration of the waveform. Two time windows of same width of 400 ns are used as integration gates. One to estimate the baseline Q_{ped}, at early time and one just around the signal peak Q_{signal}. The reconstructed charge is then defined as $Q_i = Q_{signal} - Q_{ped}$. To estimate the time, we instead perform a fit to the digitized signal waveform and then evaluate it by using a CF technique. Many degrees of freedom can be explored to optimize the result: the functional form to be used in the fit, the fit range and the value of the threshold used for the CF. If the electronics response function, ETF, had a δ behavior, the scintillating signal shape would be

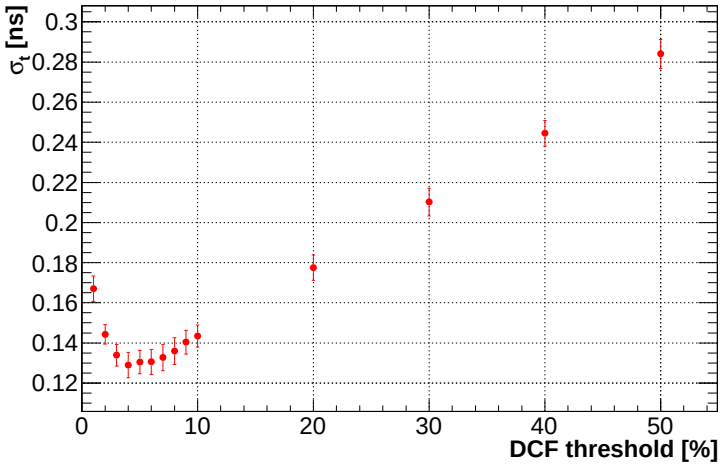

Figure 5.14: *Left: time resolution using 80 MeV electron beam as a function of the CF threshold.*

well described by the difference of two exponential functions as:

$$V(t) = \frac{e^{-t/\tau_r} - e^{-t/\tau_s}}{\tau_r + \tau_s}, \tag{5.4}$$

where τ_r is the mean time of the leading edge and τ_s is the decay time of the falling edge. In our case, the ETF of the MPPC and amplifier system is comparable to the scintillation time and a complicated convolution is needed to fit the full signal shape. An example of a waveforms produced by the CsI+MPPC+amplifier readout is shown in Figure 5.13, presenting a leading edge of about 25 ns and a total width of about 300 ns. As shown in the same figure, the fit range is restricted only to the leading edge of the pulse. The first method (standard) developed uses a Polynomial function of 4^{th} order in the range limits between the time stamps corresponding to a pulse height of 5 mV and 85% of the maximum. The time, T, is then extracted as the crossing of the fit function at 40% of the maximum height. This method has been calibrated with Cosmic Ray data sample by comparing with a simultaneous readout based on a 50 ps TDC and a fixed threshold discrimination at 20 mV.

To optimize the method, a run with an 80 MeV electron beam impinging orthogonally to the center of the matrix front face has been used. On this run, several functions have been tested: single and double exponential, exponential (single and double) convoluted with an unbiased Gaussian, and so on. For all these cases, a scan on both the fit range and the CF threshold has been operated. Finally a Lognormal

[52] function has been chosen, since it returned the best time resolution without evident systematic effects. For the fit range, the best solution is to use as lower (upper) limit the first time stamp at which the pulse is below 0.1% (85%) of the maximum pulse height. Moreover, the CF threshold has been optimized by performing a scan on its value and minimizing the time resolution. Figure 5.14 shows that the minimum of the resolution is found for a 5% threshold. Moreover, the resolution value is stable within 10% around the minimum valley in the threshold range [2%, 10%]. Figure 5.15 shows a typical fit to a signal with a large pulse height.

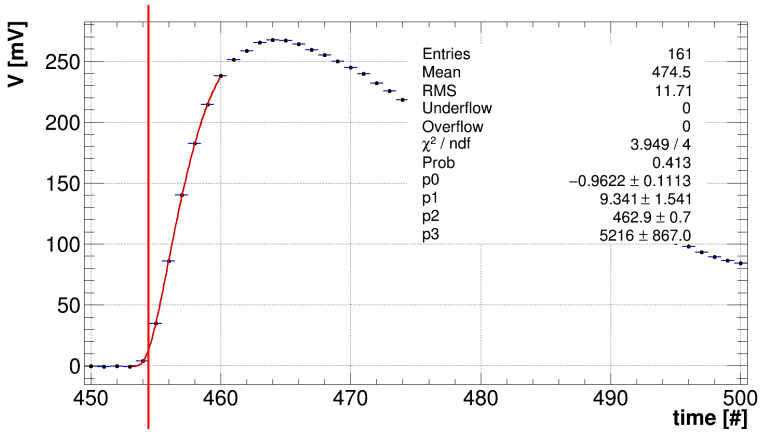

Figure 5.15: *Example of SiPMs waveform fit for a large and a small pulse.*

Since the pulses from the *finger* scintillation counters were much narrow than the ones from the crystals, a different fit range has been set. These signals present a steep leading edge of about 15 ns (3-4 time stamps) and a total width below 100 ns. Since the Lognormal is defined by 4 parameters, the fit range should be extended in the region after the waveform peak: the lower edge of the fit range has been set at the first time stamp below 5 mV and the upper one 16 ns after the peak. Figure 5.16 shows an example of the fit to a typical *finger* signal.

5.2.4 Beam and cosmic events selection

The data analysis has been performed on two samples: (i) beam electrons selected by the beam trigger and (ii) cosmic muons selected by the cosmic trigger.

For the beam events, a preliminary selection requires the sample to satisfy the

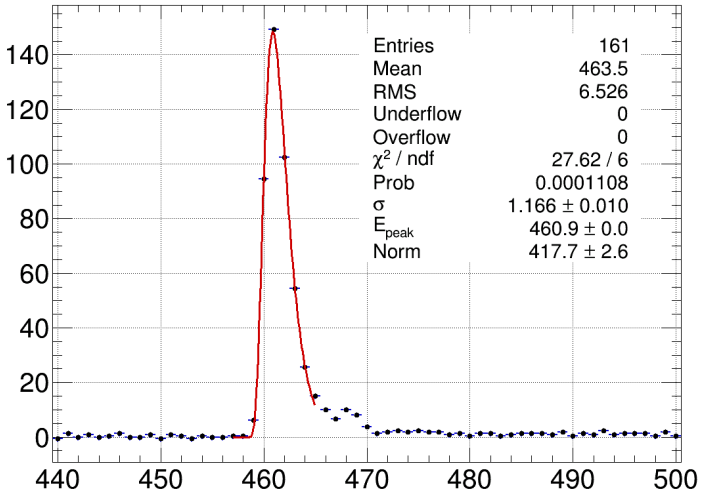

Figure 5.16: *Fit of a scintillation counter waveform using a Lognormal function.*

single particle requirement by applying cuts on the pulse height of the *finger* counters. As already stated, at the BTF, low energy electrons are produced by interaction of the primary Linac beam on a tungsten target and are then selected in momentum and multiplicity by a dedicated system based on a dipole and a set of slides. The average multiplicity depends on the user needs and, in our case, have been tuned by the accelerator experts. We have typically run with an average multiplicity of ~ 1 so that we observe also 0, 1, 2 or 3 electrons in our sample. The beam dimension, at the final window exit, exhibits a round shape, well described by a gaussian distribution with a σ of $\sim$2-3 mm in X and Y coordinate. The *finger* counters were able to intercept most of the beam. In In Figure 5.17, the scatter plot of the charge distribution for the two *finger* counters, Q_1 and Q_2 is shown. The *single particle* selection corresponds to applying the following cuts on the two pulse-heights: $Q_2 \in [30, 50]$ pC and $Q_1 \in [50, 80]$ pC.

The cosmic event selection starts by looking at the events that satisfy the cosmic ray trigger A clean selection of minimum ionizing particles, MIP, in a given column requires all the three crystals in the central column to have signals above 5 MeV and the energy sum of the other six crystals to have less than 5 MeV of deposited energy. Figure 5.18 shows the energy distribution for the selected central column crystals after this selection.

A dedicated Monte Carlo simulation, MC, of the setup has been done by means

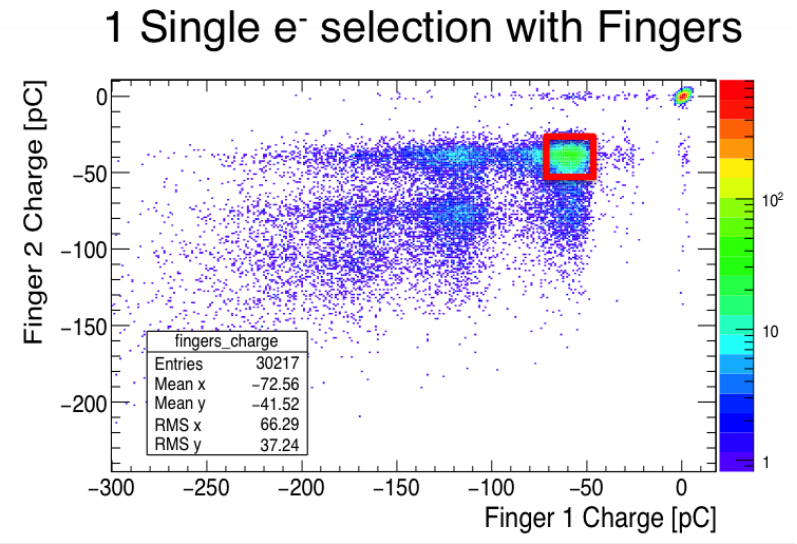

Figure 5.17: *Scatter plot of the reconstructed charges in the two scintillation counters used for triggering the beam.*

of GEANT4. Most of the geometrical details have been inserted in the simulation both regarding the used materials and the beam dimension. The transportation of optical photons has not yet been simulated. Electronic noise and average response in photoelectron yields have been instead inserted by means of gaussian or poissonian smearing. The simulation has been applied also to cosmic events. In Figure 5.18, the energy distribution of the crystals in the central column is shown both for data and MC. A good agreement between data and MC distributions is observed.

5.2.5 Channel equalization and calibration

A position scan of the calorimeter prototype has been performed with the 80 MeV electron beam sent at the center of each crystal. These data have been used both to calibrate the energy response and to determine the cable delays, T_0's and the time walk corrections for each channel. Before starting the calibration runs, the prototype was aligned using a laser system, such that the center of its front face (the side opposite to the read out) was well aligned with the beam direction.

In Figure. 5.19 the charge distribution of each crystal is shown, for the run when the beam was centered in its own position, thanks to a movable table. These

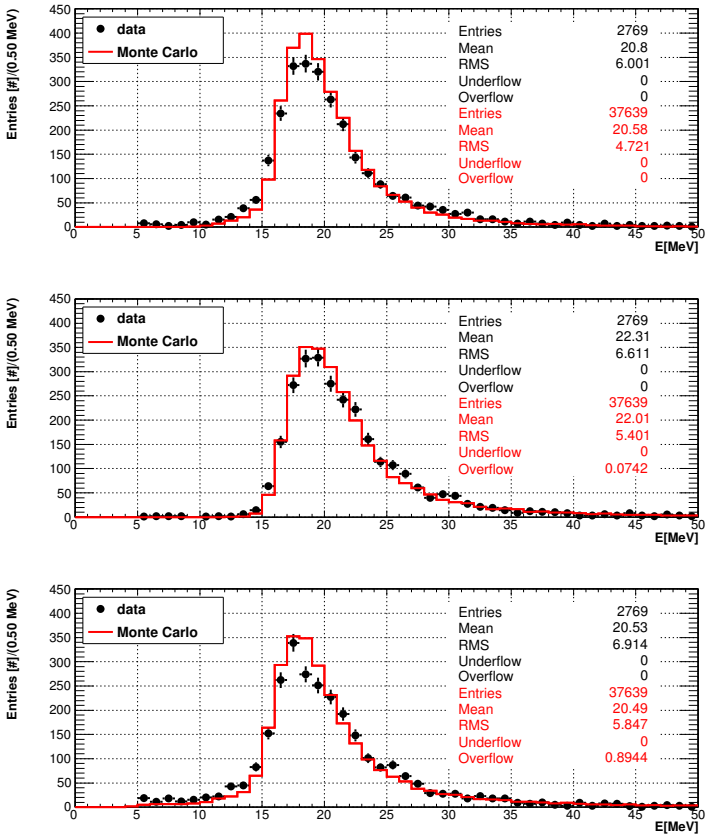

Figure 5.18: *Distributions of the crystal energy for the prototype central column after MIP selection. MC distributions are superimposed.*

distributions were fitted with a Lognormal function for evaluating the peak positions, $C(i,j)$. These values have then been used to compute the equalization factors of all the channels with respect to the central one: $A(i,j) = C(i,j)/C(1,1)$. The equalization factors have an average of 0.97 with an RMS value of 0.03. The high quality of the hardware equalization reached has been obtained by the combination of a good quality selection performed on the CsI crystals and by the well reproducible bias setting and response of the received MPPCs. The total charge of the calorimeter is then well represented by the following equation:

$$Q_{TOT} = \sum [Q(i,j)/A(i,j)]. \tag{5.5}$$

where $Q(i,j)$ represent the charge collected by the cell (i,j).

For the time calibration, time walk corrections for all channels have been determined with a similar selection of the calibration runs. Each Linac burst has a

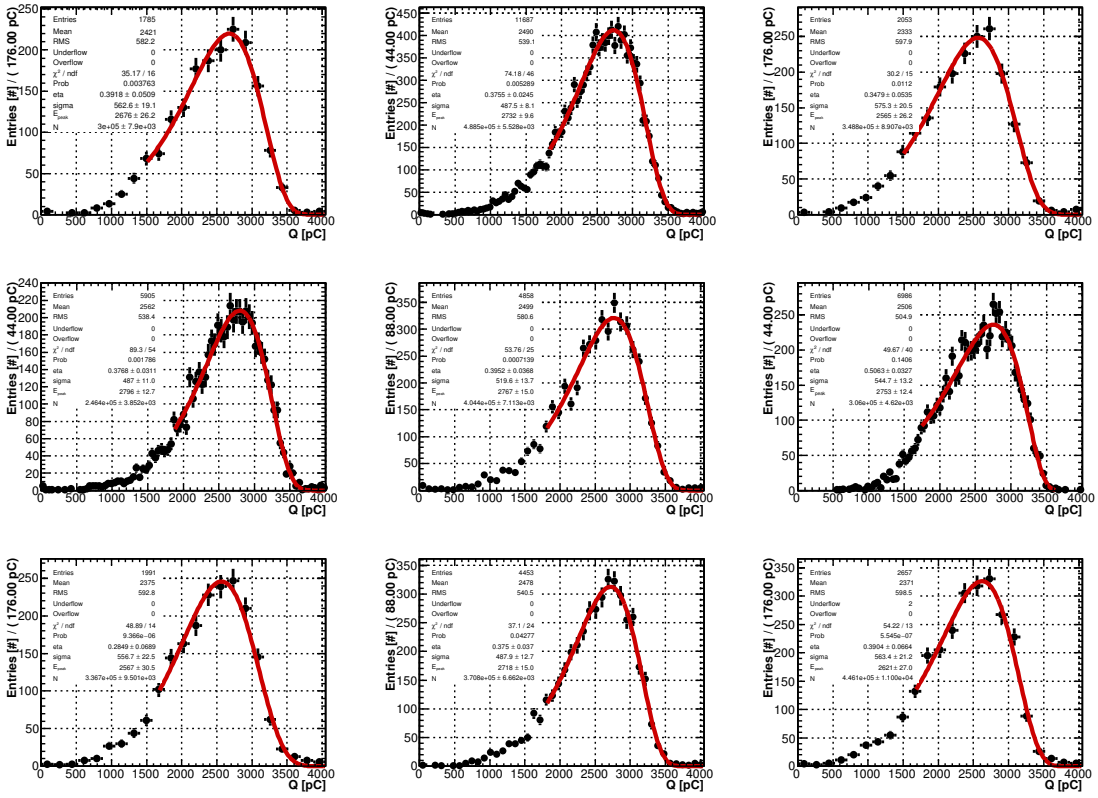

Figure 5.19: *Charge distribution from the calibration runs for all the calorimeter channels, using the 80 MeV beam.*

∼10 ns duration and it is divided into 180-200 ps long bunches. The trigger provided by the Linac start has $\mathcal{O}(10$ ns) time resolution making it necessary to use a different source of timing trigger. We rely on the mean time of the two "finger" counters, $T_s = (T_1+T_2)/2$ to provide a precise start. The timing of each calorimeter channel is then calculated as $T(i,j)_{corr} = T(i,j) - T_s$. In Figure 5.20, the profile distributions of $T(i,j)_{corr}$ as a function of the charge $Q(i,j)$ are presented for the calibration runs and for the improved timing reconstruction. A residual pulse height dependence on timing is observed as due to a dependence of the rise time from the pulse height. The distributions are fit with the "slewing" functional form: $T_0 + A/\sqrt{Q(i,j)}$. Besides from a small variation of the cable delays at a level of 100-200 ps, the corrections remains contained below 1 ns. In the following, the time distributions are evaluated for the slewing correct timing variable: $\mathbf{T(i,j)} = T(i,j)_{corr} - T_0 - A/\sqrt{Q(i,j)}$.

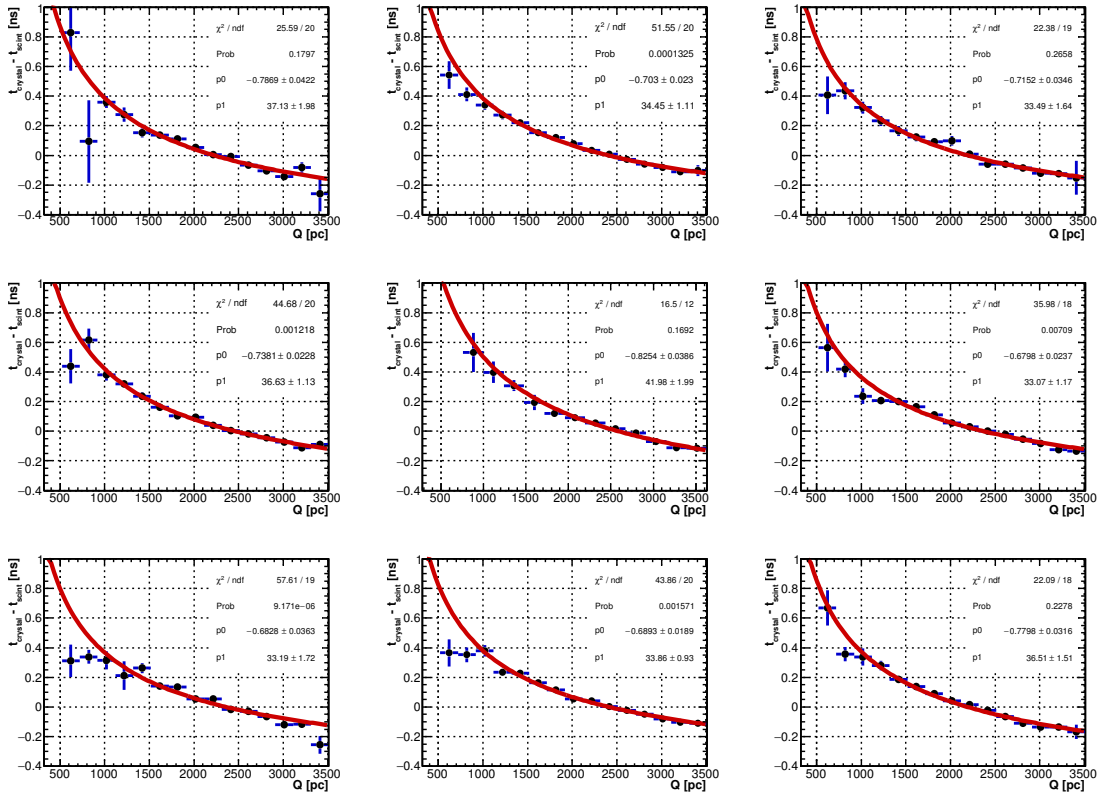

Figure 5.20: *Time walk correction out of the position scans. Histograms arrangement follows the corresponding crystal position.*

5.2.6 Energy response and energy resolution

After completing the equalization of channels, the calorimeter energy scale (in pC/MeV) has been set using both a scan in beam energy and the response to MIPs. For electrons, this has been done for a set of runs with the beam impinging orthogonally to the calorimeter prototype front face at the following energies: 80, 90, 100, 110 and 120 MeV. Moreover the low energy point provided by the MIP, corresponding to around 20 MeV, has been included.

For the electrons, a further quality selection has been applied to reduce the events with multiplicity higher than 1 surviving the "single particle" selection done with the finger counters. This cut eliminates the events with Q_{tot} too large with respect to the signal peak. However, in several runs there was a class of events with saturated signals surviving also this cut, as the example shown in Figure 5.21 (left).

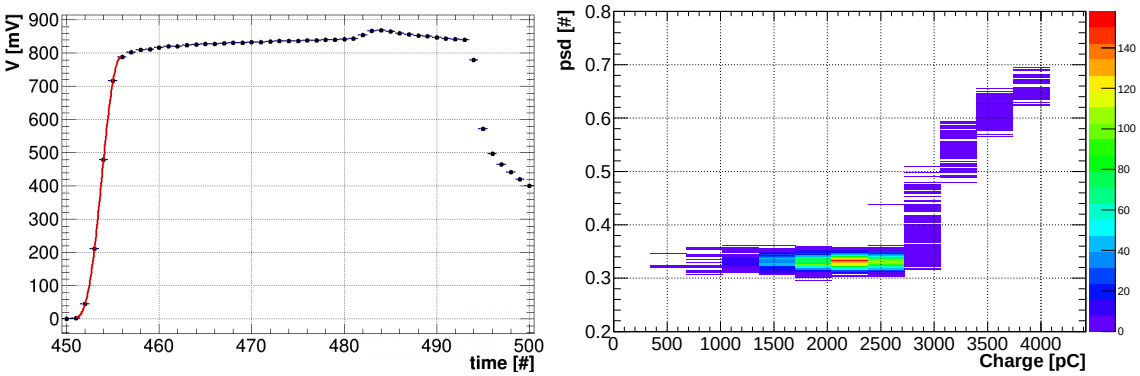

Figure 5.21: *Left:saturated signals read out from the central crystal of the matrix. Red lines show the fit result used for the time reconstruction. Right: Pulse shape discriminator variable versus the reconstructed charge.*

To identify these cases, a discriminator variable, pulse shape discrimination, **psd**, has been built as

$$\mathbf{psd} = \frac{\int_a^b V(t)}{Q_{tot}},$$

where a is the waveform time stamp at 1% of the maximum waveform height and b is the point at 90% of maximum waveform height on the trailing edge. Figure 5.21 (right) shows the typical distribution of the **psd** variable as a function of Q_{tot}. In the analysis, only the events with **psd** below 0.355 have been retained.

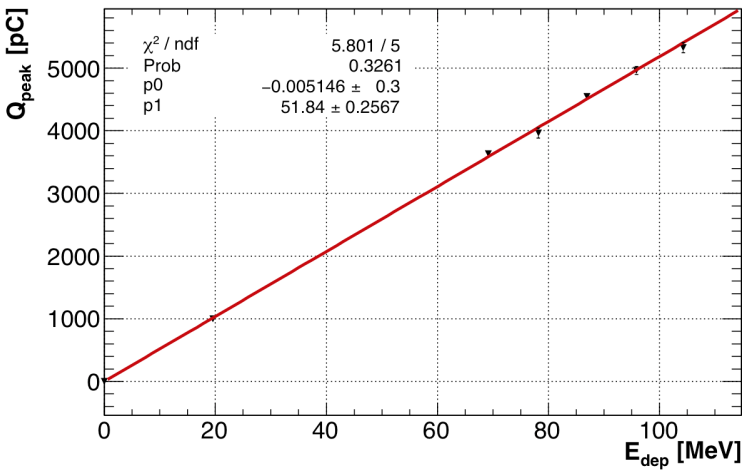

Figure 5.22: *Peak value, Q_{peak}, of the reconstructed total charge of the prototype in the calibration runs as a function of E_{dep}. The red line represents a linear fit.*

After this selection, we have performed a Lognormal fit to the Q_{tot} variable for each run and reported the peak values, Q_{peak}, as a function of the average deposited energy, E_{dep}, as estimated by the simulation. This is shown in Figure 5.22.

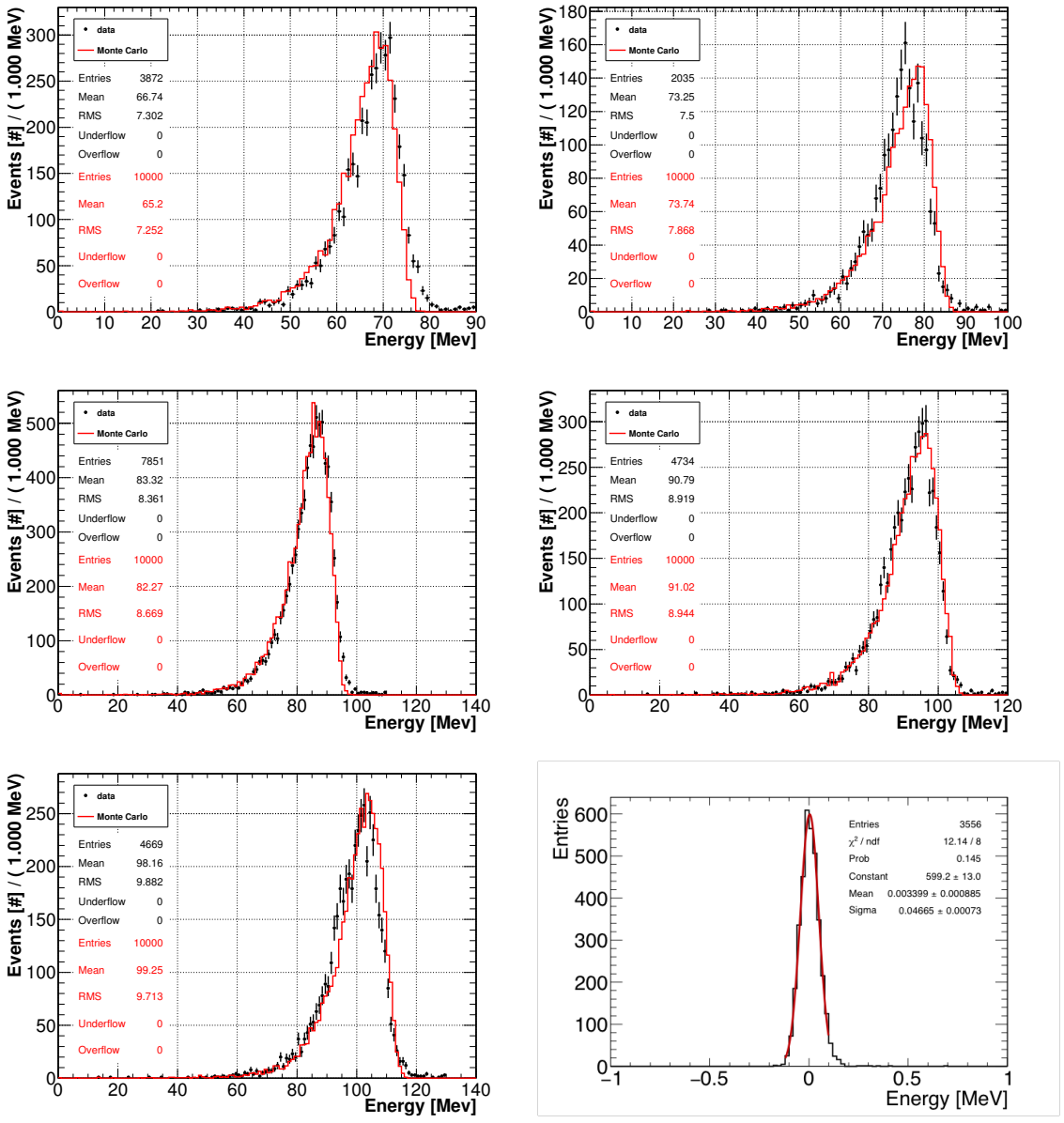

Figure 5.23: *Energy distribution from data overlaid with the Monte Carlo for the following runs: 80 (top-left), 90 (top-right), 100 (middle-left), 110 (middle-right) and 120 (bottom) MeV. In the last plot, the single channel noise distribution is also reported (bottom right.)*

The Q_{peak} values are fit to a line: the constant term is compatible with 0, the slope, $k_{cal} \sim 52$ pC/MeV is used as energy-scale. Using the total gain provided by the product of MPPC and amplifier amplifications, this k_{cal} value corresponds to an average light yield of ~ 32 pe/MeV. The total calorimeter energy, E_{tot}, is then derived as $E_{tot} = Q_{tot}/k_{cal}$.

The distribution in Figure 5.23 show E_{tot} for the different runs, MC distributions are superimposed. A good data-Monte Carlo agreement is observed. The bottom plot on the right shows the noise distribution for a channel as estimated by the events without any electrons in the matrix. The noise per channel corresponds to ~ 50 keV.

From the same E_{tot} distributions, I have evaluated the energy resolution by plotting the σ of the Lognormal fit as a function of E_{dep} as reported in Figure 5.24. The resolution estimated by the Monte Carlo is also shown superimposed in the same plot. Data and Monte Carlo show a good agreement within the uncertainties. The energy resolution measured ranges from 7.4% to 6.5% in the energy deposition range (70, 102) MeV and is dominated by energy leakage. The contribution of the noise is practically negligible (< 150 keV) as well as the stochastic term due to the photoelectron statistics that is evaluated to be between 1.4 to 2% from the estimated light yield and excess noise considerations.

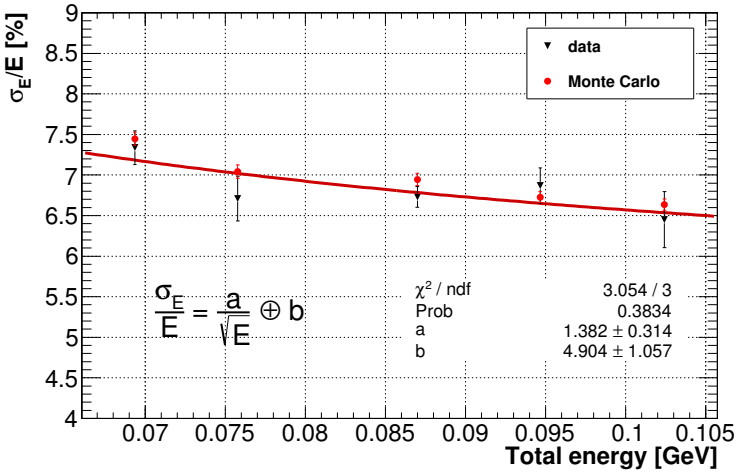

Figure 5.24: *Energy resolution from data (black) compared with Monte Carlo (red).*

5.2.7 Measurement of time resolution

The time resolution, σ_t, has been measured in different ways using: (i) only the crystal with the highest energy deposition; (ii) the energy-weighted mean time of all crystals in the matrix:

$$T_{\text{mean}} = \Sigma(T(i,j) \cdot E(i,j))/E_{tot}, \qquad E_{tot} = \Sigma E(i,j),$$

The shape of the recorded signal waveforms has been found to be dependent on the integrated charge. Figure 5.25 shows the dependence of the length of the waveform leading edge, $t_{peak} - t_{crystal}$, on the energy deposited in the crystal. To reduce this dependence, signals used for timing measurements were required to have a deposited energy above 10 MeV.

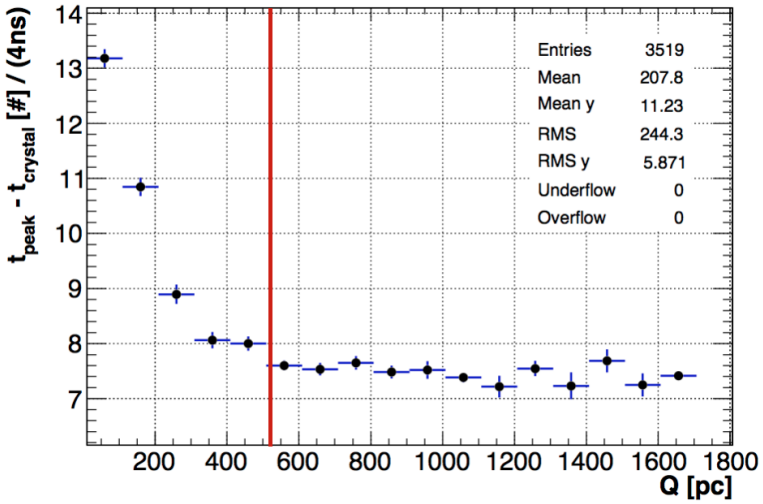

Figure 5.25: *Pulse rising time as a function of the signal reconstructed charge. The red line indicates the 10 MeV equivalent threshold.*

5.2.7.1 Time resolution at normal incidence

The time resolution has been measured for the of 80, 90, 100, 110 and 120 MeV beam energies, with the beam focused in the center of the calorimeter prototype and the beam direction orthogonal with respect to the calorimeter face. The charge distribution obtained is fit with a gaussian function, the σ of the fit is used to

evaluate the resolution. The time resolution, as a function of the energy deposited in the crystal, is shown in Figure 5.26 after having subtracted the T_s jitter contribution. The time resolution varies from 130 ps, at 45 MeV, to 110 ps, at 69 MeV of deposited energy in the central crystal (corresponding to 80 and 120 MeV beam momentum respectively).

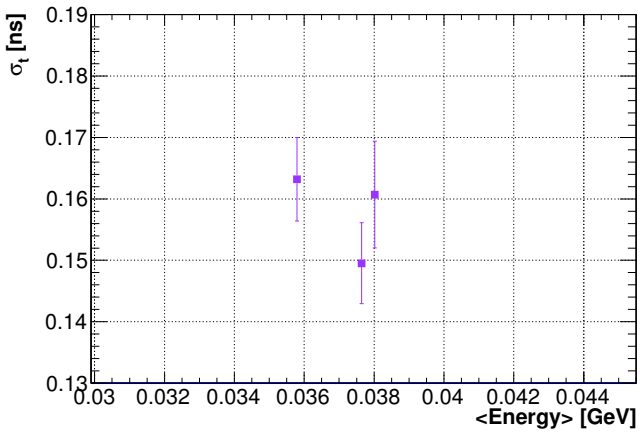

Figure 5.26: *Time resolution of the most energetic crystal, after subtraction of the T_s jitter, as a function of the mean energy deposited in the crystal.*

Similarly, Figure 5.27 shows the obtained resolution of the time distribution, after subtracting the jitter contribution, function of the mean deposited energy, when the energy weighted time, T_{mean}, is used for the crystals above 10 MeV as a function of the mean deposited energy. The time resolution varies from 120 ps, at 53 MeV, to 105 ps, at 82 MeV of energy deposition (corresponding to 80 and 120 MeV beam momentum respectively, after the application of the 10 MeV threshold on signals selection).

5.2.7.2 Cosmic rays

Measurement of the time resolution with cosmic muons is important as the muon rejection and electron-muon separation will be an important part of the Mu2e data analysis.

Cosmic rays have been used for time resolution measurement at fairly low energy. Indeed, selecting the events where the cosmic ray energy deposition is contained

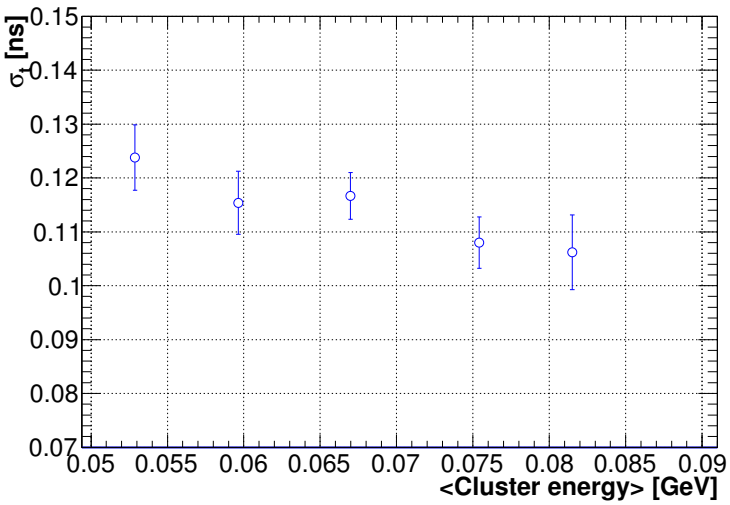

Figure 5.27: *Time resolution of the energy weighted mean time, after subtraction of the T_s jitter, as a function of the mean energy deposited in the matrix.*

inside a single column, the "neighboring crystals" technique can be used for quoting the time resolution corresponding to a MIP energy deposition in approximately the3 cm depth of crystal. This procedure however includes also an additional fluctuation due to the jitter in the path length of the muons crossing multiple crystals at different angles. The MIP single column selection has been used for the central column. The time resolution, with the neighboring crystals technique, has been applied to two pairs of crystals: central-top and central-bottom. The same time walk corrections found in the calibration runs have been applied. Figure 5.28 shows the time residual for the two pairs. Taking into account the factor $\sqrt{2}$, the resulting time resolution is of about 240 ps/crystal that corresponds to an average energy deposition of $\sim$ 20 MeV. The average energy deposition for a muon faking an electron in the Mu2e detector will be of $\sim$ 40 MeV so that another $\sqrt{2}$ improvement is expected in the final experiment.

5.2.7.3 Summary of timing results

Two different reconstruction methods have been used for the determination of timing, a conservative one with a CF threshold set to 40% of the maximum pulse height and an improved one with the threshold set at 5%. The latter one improves the tim-

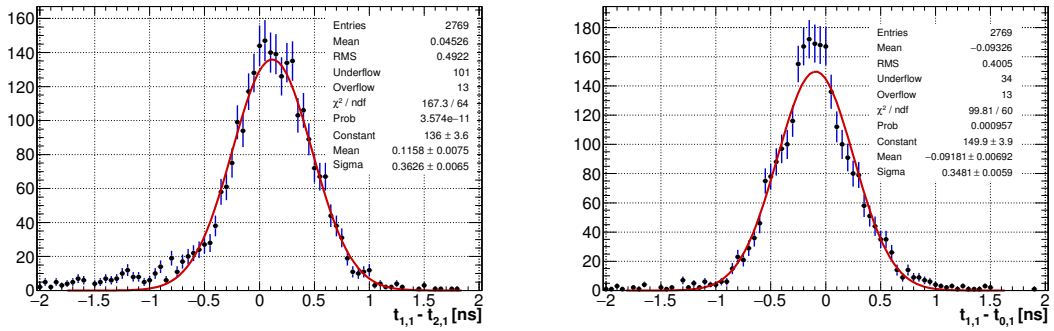

Figure 5.28: Cosmic time residual plots. Left: between crystals (1,1) and (2,1). Right: between crystals (1,1) and (0,1).

ing of almost a factor of two for large signals while provides marginal improvement for energy deposition comparable to that deposited by a minimum ionizing particle.

For the improved method, three different samples have been used to determine the timing resolution in different geometrical configurations. To understand relative merits of each technique, the obtained timing is reported as a function of the deposited energy in Figure 5.29. The first observation is that the time resolution measured using "contiguous crystals" (red marker) agrees well with the corresponding measurement performed using the external trigger (open triangle). A second observation is that the timing for a MIP is comparable to the one related to similar energy deposition. Moreover, a scan with the calorimeter prototype rotated by 50° has been performed. In this case the timing resolution has been measured using the difference between two neighboring crystals with similar energy deposition [53]. The results obtained using the energy weighted technique in the tilted configuration are slightly worse with respect to those obtained in the orthogonal configuration in the same energy bins. This is attributed to additional time jitter between the signals from different crystals due to shower fluctuations.

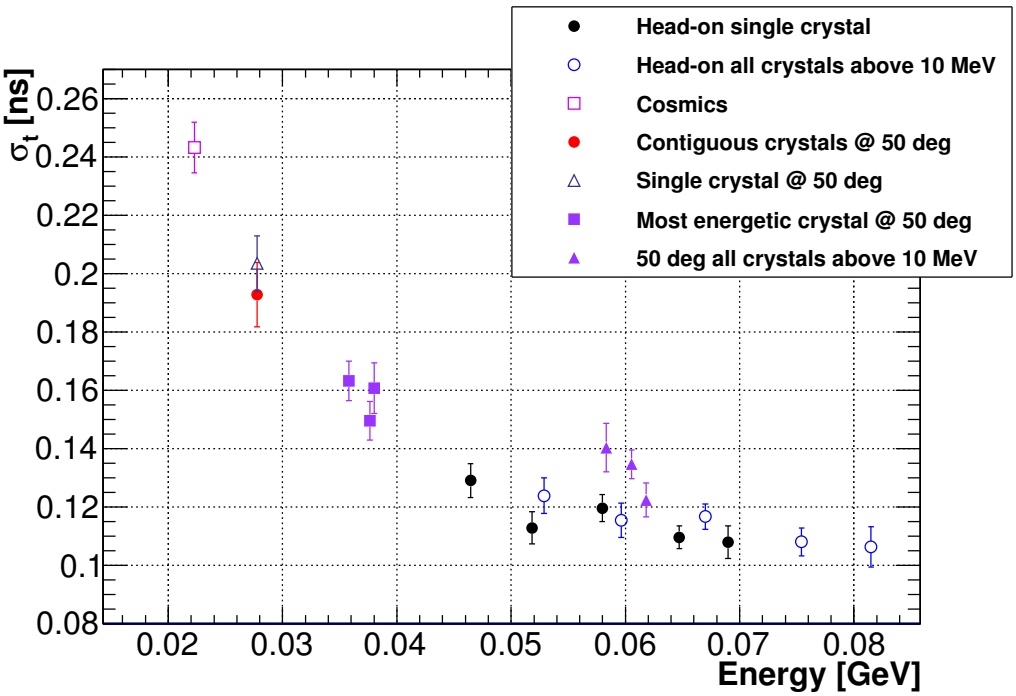

Figure 5.29: *Time resolution summary plot. The legend explain the techniques used in the analysis of each reported point.*

Conclusions

In this thesis we have shown the goal of the Mu2e experiment and its physics motivation: the research of the charge lepton flavor violating process $\mu + N(A, Z) \rightarrow e + N(A, Z)$ with a single event sensitivity of 2.7×10^{-17} in three years of running. This search complements direct searches for New Physics since this process can occur in virtual loops where higher mass particles can contribute.

In order to achieve such sensitivity, the Mu2e experimental setup is based on a peculiar Superconducting Magnetic System, which has been briefly described. This apparatus, combined with an intense, pulsed muon beam will help to improve the present limit on $\mu - e$ conversion of four orders of magnitude. Its results, combined with the ones from MEG-II will help to discriminate between several New Physics scenarios. Subsequently, we have demonstrated, through a software simulation, that a calorimeter with high granularity is required to perform a powerful μ/e particle identification and provide a tracking independent reduction filter (software trigger) for the experiment and keep functionality in an environment with a delivered dose of 12 krad/year in the hottest area. Moreover, the calorimeter should work in 1 T axial magnetic field and a 10^{-4} Torr vacuum. We therefore aim for a calorimeter with large acceptance for monoenergetic electrons of 104.7 MeV and reasonable energy O(5%) and time O(500 ps) resolution in this energy region.

The baseline calorimeter design is composed of two disks of BaF_2 scintillating crystals readout by a new generation APD. Indeed, since the BaF_2 has a fast component (220 nm) and a large slow component (310 nm), the photosensors should have two properties: 1) a high quantum efficiency in the UV region, down to 200 nm and 2) solar blind for the components above 220 nm. Since the APDs are still in the development phase, we have pushed forward an intense R&D stage to check if the

combination of a cheaper crystals, pure CsI, emitting at higher frequency (310 nm), coupled with large area MPPC can satisfy the requirements.

In the fourth chapter we have shown our measurements on single crystals. Light yield and longitudinal response uniformity for ($3\times3\times20$) cm^3 undoped CsI and BaF_2 crystals from different manufacturers have been measured using a ^{22}Na radioactive source. The 2015 pure CsI crystals, wrapped in 150 μm tick Tyvek, have a LY around 100 $N_{p.e.}$/MeV, which increases with optical grease of about 60%. These crystals also show a good longitudinal response uniformity, smaller than $\delta \sim 0.8\%$/cm, when coupled in air, proving a significant improvement with respect to the previous SICCAS 2014 samples. Optical coupling with grease deteriorates uniformity up to $\delta \sim 1.2\%$/cm. Results on BaF_2 wrapped with 75 μm tick Teflon show a similar LY for the fast component and a LRU at the level of $\delta \sim 0.8\%$/cm, which significantly deteriorates to $\delta \sim 2.5\%$/cm using optical grease.

The determination of the LY and LRU changes, for undoped CsI and BaF_2 crystals after irradiation with a large ionization dose and neutron fluency, provides an important benchmark for the Mu2e calorimeter, where a high irradiation environment is foreseen. About 30 krad of ionization dose is expected for crystals of the innermost ring in three years of running. A ionization dose up to 20 krad does not modify the light yield ($\sim$ 35 $N_{p.e.}$/MeV at crystal center) and LRU (20%) for unwrapped SICCAS CsI crystals, coupled in air to an UV-extended PMT. After a total dose of 90 krad, a 20% (50%) reduction in LY (LRU) has been observed. Teflon wrapping improve LRU to 20%. Coupling with optical grease allows to reach a light yield of $\sim$ 80 $N_{p.e.}$/MeV at the crystal center. Some fluorescence effects are visible after an intense irradiation dose, which becomes negligible after few hours.

CsI and BaF_2 crystals have also been irradiated with a 14 MeV neutron flux up to 9×10^{11} n/cm^2, corresponding to about 1.5 (3) times the total flux expected for the first (second) calorimeter disk in three years of running. At the end of the irradiation test, a negligible acceptable deterioration of the light yield has been observed. Except for the undoped CsI from SICCAS, the longitudinal response uniformity is maintained well below 10% for Tyvek wrapped crystals with PMT coupling in air, without deterioration due to the neutron irradiation. For the SICCAS crystal, a deterioration from 5% to 15% has instead been observed.

Once we have completed single channel measurements, a 3×3 calorimeter prototype of CsI crystals readout by UV-extended TSV SPL MPPCs have been assembled and tested at the Beam Test Facility in Frascati with an electron beam in the energy range from 80 to 120 MeV. A light yield of ~ 30 $N_{p.e.}$/MeV has been measured. The large amplification of the MPPCs allows for large pulse heights and fast rise time that imply a precise time resolution. An energy resolution of $\sim 7\%$ and a time resolution of 110 ps have been achieved for 100 MeV electrons impinging perpendicularly to the calorimeter surface. The simulation well reproduces the observed energy distribution.

These results show that the CsI+MPPC configuration well satisfies the Mu2e calorimeter requirements while granting flexibility for the possible running options. Indeed, another gain factor of two in light yield is expected by using a double MPPC readout, so that the options of running with crystal-photosensor optical coupling in air as well as operating at voltages below V_{op} is possible.

If the R&D os solar blind APD will not be ready by the technological choice deadline, the backup option of CsI crystal coupled to MPPC photosensor will be used as a viable solution for the Mu2e calorimeter.

Bibliography

[1] G. Altarelli, "The Standard Model of Particle Physics", arXiv:hep-ph/0510281 - 2005.

[2] ATLAS collaboration home page, `http://atlas.ch`.

[3] CMS collaboration, "Observation of a new boson at a mass of 125 GeV with the CMS experiment at the LHC", Phys. Lett. B, Vol 716, Issue 1, Pag. 30-61 (arXiv:1207.7235) - 2012.

[4] G. Aad et al. [ATLAS Collaboration], "Observation of a new particle in the search for the Standard Model Higgs boson with the ATLAS detector at the LHC", Phys. Lett. B, Vol. 716, 1, Pag. 1-29 (arXiv:1207.7214) - 2012.

[5] Super-Kamiokande Collaboration, Y. Fukuda et al, "Evidence for oscillation of atmospheric neutrinos", Phys. Rev. Lett. 81, 1562 (arXiv:hep-ex/9807003) - 1998.

[6] J.N. Bahcall, M.C. Gonzalez-Garcia and C. Peña-Garay, "Global analysis of solar neutrino oscillations including SNO CC measurement", Journal of High Energy Physics, Volume 2001, JHEP08 - 2001.

[7] R. N. Mohapatra, "Seesaw Mechanism and Its Implications", arXiv:hep-ph/0412379 - 2004.

[8] Jeffrey A. Harvey and Michael S. Turner, "Cosmological baryon and lepton number in the presence of electroweak fermion-number violation", Phys. Rev. D 42, 3344 - 1990.

[9] Pawel Guzowski, "A combined limit for neutrinoless double-beta decay", arXiv:1504.08285 - 2015.

[10] A. de Gouvea and P. Vogel, "Lepton Flavor and Number Conservation, and Physics Beyond the Standard Model", Progress in Particle and Nuclear Physics, Vol 71, pag. 75-92 (arXiv:1303.4097) - 2013.

[11] Yoshitaka Kuno and Yasuhiro Okada, "Muon decay and physics beyond the standard model", Rev. Mod. Phys. 73, 151 - 2001.

[12] A. Czarnecki, X. G. Tormo and W. J. Marciano, "Muon decay in orbit: spectrum of high-energy electrons", Phys. Rev. D84 013006 - 2011.

[13] Fermilab, Proton Improvement Plan-II (PIP-II), `https://pip2.fnal.gov` - 2015.

[14] J. Adam et al., "New constraint on the existence of the $\mu \to e\gamma$ decay", Phys. Rev. Lett., 110:201801 - 2013.

[15] A.M. Baldini et al., "MEG Upgrade Proposal", Paul Scherrer Institute Research Committee - 2013.

[16] MEG collaboration, J.Adam et al., "New Constraint on the Existence of the $\mu \to e\gamma$ Decay", Phys. Rev. Lett., 110:201801 - 2013.

[17] C.H.te.Cheng, B.Echenard and D.G.Hitlin, "The next generation of $\mu \to e\gamma$ and $\mu \to 3e$ CLFV search experiments", Snowmass - 2013.

[18] L. Calibbi et al., "Status of supersymmetric type-I seesaw in SO(10) inspired models" JHEP, 1211:040 - 2012.

[19] W. Bertl et al., "A search for $\mu \to e$ conversion in muonic gold", EPJ C, 47(2):337:346 - 2006.

[20] R. Harnik, J. Kopp, and J. Zupan, "Flavor Violating Higgs Decays", JHEP, 1303:026 - 2013.

[21] M. Blanke et al., "FCNC Processes in the Littlest Higgs Model with T-Parity: a 2009 Look", Acta Phys. Polon., B41:657:683 - 2010.

[22] J. M. Arnold, B. Fornal, and M. B. Wise, "Phenomenology of scalar leptoquarks", Phys. Rev., D88:035009 - 2013.

[23] P.S. Bhupal Dev, C.H. Lee and R. N. Mohapatra, "Natural TeV-Scale Left-Right Seesaw for Neutrinos and Experimental Tests", Phys. Rev., D88(093010) - 2013.

[24] A. Czarnecki, M. Dowling et al., "Michel decay spectrum for a muon bound to a nucleus", Phys. Rev. D 90, 093002 (arXiv:1406.3575) - 2014.

[25] N. Berger for the Mu3e collaboration, "The Mu3e experiment", Nuclear Physics B Proceedings Supplement 00 16 - 2013.

[26] SINDRUM II Collaboration (Bertl, Wilhelm H. et al.), "A Search for muon to electron conversion in muonic gold", Eur. Phys. J. C47 337-346 - 2006.

[27] A. Czarnecki, X. Garcia i Tormo and W. J. Marciano, "Muon decay in orbit spectra for $\mu - e$ conversion experiments", Hyperfine Interact, 210 19 - 2012.

[28] L. Bartoszek et al., "Mu2e Technical Design Report", Fermi National Accelerator Laboratory - 2014.

[29] IPAC, "Proc. 2nd International Particle Accelerator Conference", IPAC 2011, San Sebastian, Spain - 2011.

[30] S. Ahmad et al., "Searches for muon-electron and muon-positron conversion in titanium", Phys. Rev. Lett., 59(970) - 1987.

[31] R. Ehrlich, "Update on the cosmic background simulation", Mu2e-doc-4184 - 2014.

[32] F. Cervelli et al., "Study of the DIO rate for a calorimeter based trigger", Mu2e-doc-3456-v1 - 2013.

[33] P. Murat, "Particle Identification with the Mu2e Detector and Rejection of the Cosmics-Induced Background", Mu2e-doc-2992 - 2013.

[34] D. Brown, "Tracker Selection Cut-set C" Mu2e-doc-3996-v3 - 2014.

[35] R.-Y. Zhu, "Radiation damage in scintillating crystals", Nucl. Inst. And Meth. A413 297-311 - 1998.

[36] S. Nikzad et al., "Delta-doped electron-multiplied CCD with absolute quantum efficiency over 50% in the near to far ultraviolet range for single photon counting applications", Appl. Opt., 51:365:369 - 2012.

[37] Gordon Gilmore, "Practical Gamma-ray Spectroscopy", Wiley editor - 2008.

[38] C.M.Hawkesetal., "Decay time and Light Yield measurements for plastic scintillating fibers", Nucl. Instrum. Meth. A292, 1990, 329-336.

[39] G. Pezzullo and B. Echenard, "Study of the radiation dose and neutron flux on the calorimeter'", Mu2e-doc-2853.

[40] Hamamatsu, "TSV MPPC array", production flyer 2015.05 KSX-I50080-E-S13361-3050xx-04.

[41] Advanced RISC Machines, `http://foldoc.org/Advanced%20RISC%20Machines` - 1997.

[42] I. Sarra, R. Donghia et al., LNF Mu2e calorimeter group, "The backup option - CsI+MPPC: Tests, measurements and plans", Mu2e Document 5701-v6 - 2015.

[43] S. Baccaro, A. Cecilia and A. Pasquali, "γ irradiation facility at ENEA-Casaccia Centre, Roma", ENEA Report RT/2005/28/FIS - 2005.

[44] M. Martone. M. Angelone and M. Pillon, "The 14 MeV Frascati neutron Generator", Journal of Nuclear Materials 212-215 (1994) 1662-1664.

[45] Z.Y. Wei and R.Y. Zhu, "A study on undoped CsI crystals", Nucl. Inst. and Meth. A326 (1993) 508.

[46] R.Y. Zhu, "Crystals: optical, scintillation properties and radiation hardness", Mu2e-doc-5699 - 2015.

[47] J.O.Gichaba, "Measurements of TYVEK Reflective Properties for the Pierre Auger Project", The University of Mississipi, 1998.

[48] Filar optoMaterials s.r.l., `http://www.filaroptomaterials.com` - 2015.

[49] Institute for Scintillation Materials, `http://www.isma.kharkov.ua/eng/` - 2015.

[50] M.Cordelli, R.Donghia et al., "Irradiation tests with ionization dose and neutrons for undoped CsI and BaF_2 crystals", Mu2e-doc-5800 - 2015.

[51] B.Buonomo, G.Mazzitelli and P.Valente, "Performance and Upgrade of the DAFNE Beam Test Facility (BTF)", Nuclear Physics B - Proceedings Supplements, 150:362-365 - 2006

[52] A. Lucà, I. Sarra, "GEANT4 Simulation of the Response of a LSO Crystal Electromagnetic Calorimeter to 105 MeV/c Electrons", Mu2e-doc 2625-v1

[53] O. Atanova et al., "Experimental test of an undoped CsI+MPPC calorimeter prototype with electron beam in the enrgy range 80 to 140 MeV", Mu2e-doc-5816-v1

Acknowledgements

There are a lot of people I would like to thank for supporting me over the past years. Their help, guidance and friendship have been undoubtedly precious for me.

First and foremost, I would like to express my gratitude to my supervisor, Chief Misc for his help, patience and guidance on my master thesis; his ideas and feedback have been absolutely invaluable.

I would certainly like to thank my advisor Ivano, for the fundamental support and engagement he gave me through the learning process of the last months, considering me not only as a student but also as a "little sister". I would also like to thank my co-workers at the National Laboratory of Frascati: Roberto, Marco, Simona and Fabio.

My sincere thanks also goes to Professor Domizia Orestano, who spent time and effort correcting my thesis, while helping and supporting me at Roma Tre University.

I would especially like to thank my fellow Roma Tre colleagues and friends, who kept me entertained with enjoyable moments both within university and outside it, in particular Carlotta, Salvo, Anto, Rubi and Fuego. I am sure without them and without their support , I would not be at this stage.

Finally, I would like to thank all those people outside both Roma Tre and the physics faculty: they kept me in touch with reality, spending together awesome moments that I will never forget. First, I thank my "synchro" team, especially Lori, Mile, Caro, Emi and my coach Eli, for all the laughs and the efforts we shared in the swimming pool, and for special friendship we have beyond it. Thanks also to whom I have known for many years, and who is still standing me: Ele, Gio, Marco and Bruno.

Last but not least, I would like express my gratitude to my amazing family for their constant support. Thanks to my brother and sister and their great families, which are my first "funs" and they are always ready to support me morally. Most of all, I would like to thank my parents: no words can explain my gratitude for what they have done and they still do for me.